FINITE ELEMENT ANALYSIS OF SLIP SYSTEMS IN SINGLE CRYSTAL SUPERALLOY NOTCHED SPECIMENS

By

SHADAB A. SIDDIQUI

A THESIS PRESENTED TO THE GRADUATE SCHOOL
OF THE UNIVERSITY OF FLORIDA IN PARTIAL FULFILLMENT
OF THE REQUIREMENTS FOR THE DEGREE OF
MASTER OF SCIENCE

UNIVERSITY OF FLORIDA

2003

Dedicated to my **parents**, because of whom I am here, and to my fiancée **Rukshana** who guided my steps in the most difficult moments and gave me her support for completing this task.

ACKNOWLEDGMENTS

I would like to thank Dr. Nagaraj Arakere, my research advisor, for giving me the opportunity to work in his group and for his valuable assistance and advice during the different stages in the development and successful completion of this research. I would also like to thank my supervisory committee members for their contributions to the completion of this project.

I would also like to thank Srikant, Rukshana, Jeff and my lab mates for their help and support. Finally, I thank God for helping me complete this task.

TABLE OF CONTENTS

LIST OF TABLES

LIST OF FIGURES

Abstract of Thesis Presented to the Graduate School
of the University of Florida in partial fulfillment of the
Requirements for the Degree of Master of Science

FINITE ELEMENT ANALYSIS OF SLIP SYSTEMS IN SINGLE CRYSTAL
SUPERALLOY NOTCHED SPECIMENS
By

Shadab A. Siddiqui

May 2003

Chairman: Nagaraj Arakere.
Major Department: Mechanical And Aerospace Engineering

Fatigue failure of turbine engine components is a pervasive problem. Among the most demanding structural applications for high temperature materials are those of aircraft engines and power generating industrial gas turbines. In particular, the turbine blades and vanes used in these applications are probably the most demanding, due to the combination of high operating temperature, corrosive environment, high monotonic and cyclic stresses, long expected component lifetimes and the enormous consequences of structural failure. However, the need to maximize efficiency results in the need to minimize component weight and forces design margins to be as small as possible.

To develop a mechanistically based life prediction system, an understanding of the evolution of slip systems in regions of stress concentration, under the action of 3-D fatigue stresses, is necessary. A study of slip systems in 3-D anisotropic (single crystal) stress fields is presented as a function of crystal orientation. Three-dimensional anisotropic stress fields are examined by analyzing the stress field in a single crystal

double-edged notched rectangular specimen with varying crystal orientation. Slip fields activated near the notch during tensile loading are observed experimentally (Material Science And Engineering Department, University of Florida). Detection of the specific slip systems is possible through the study of the visible traces left on the surface of the specimens. Three-dimensional FEA of the specimen is used to predict the slip systems. Analysis results are verified by comparing them with experimentally generated slip fields. The load and the crystallographic orientations govern the activation of specific slip systems.

Slip systems are examined for two different crystal orientations at the surface and on the mid planes. For both orientations, the resulting slip sectors are different. Maximum resolved shear stresses for both the orientations are found to be on their mid planes. The past research, which used 2-D isotropic plane stress or plane strain model, predicts sectors with straight boundaries. The present 3-D anisotropic FEA analysis with accurate representation of specimen geometry and load predicts curved slip sectors boundaries with complex shapes. Overall, the slip systems predicted by 3-D FEM show very good agreement with experimentally measured slip systems on the surface.

CHAPTER 1
SINGLE CRYSTAL SUPPERALLOY

Superalloys

Superalloys are a group of nickel-, iron-nickel-, and cobalt- base alloys that are used at temperature above about 540°C. Initially superalloys were developed for use in aircraft piston engine turbo superchargers. Their development over the last 60 years is because of their usage in advancing gas turbine engine technology. Superalloys exhibit a combination of high strength at high temperatures, excellent creep and stress rupture resistance, toughness and metallurgical stability; useful thermal expansion characteristics and strong resistance to thermal fatigue and corrosion. The high temperature strength of all superalloys depends on the principle of a stable, face centered cubic (FCC) matrix, combined with either precipitation strengthening and/or solid solution hardening. In general, superalloys have an austenitic (γ phase) matrix and contain a wide variety of secondary phase. The most common secondary phases are γ' and metal carbides. Nickel base superalloys are the most widely used alloy for the hottest parts. The high phase stability of the FCC nickel matrix and the capability to be strengthened by a variety of direct and indirect means are the principal characteristics of nickel superalloys. The introduction of directional- solidification and single crystal casting technology are the additional aspect of nickel- base superalloys (Davis, 1997). These alloys exhibit better high temperature properties than polycrystalline wrought or cast alloys (Figure 1-1).

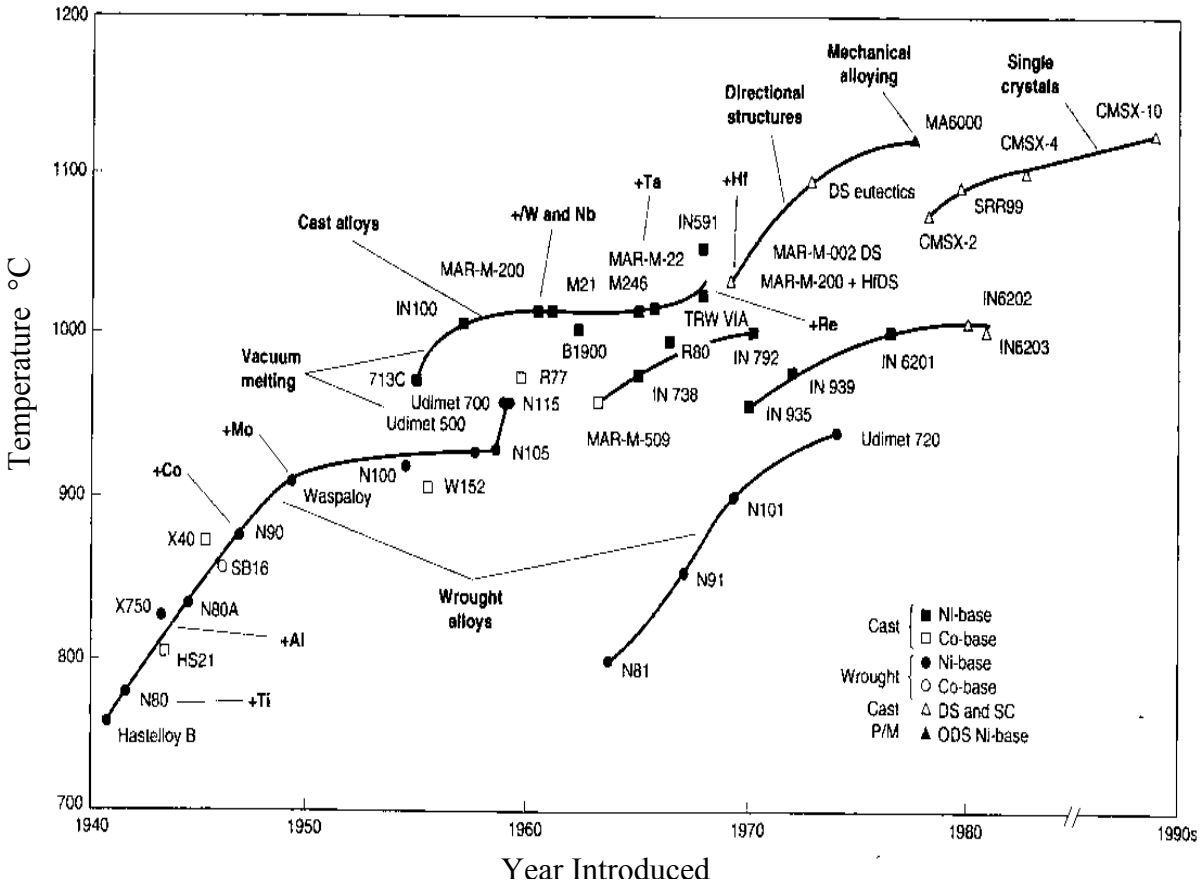

Figure 1-1 Temperature capability of superalloys with approximate year of introduction. (Davis, 1997)

Microstructure of Superalloys

The major phases that are present in superalloys are, gamma matrix (γ), gamma prime (γ'), gamma double prime (γ''), grain boundary, carbides and borides. γ matrix, in which the continuous matrix is an FCC nickel base nonmagnetic phase, usually contains a high-percentage of solid solution elements. γ is present as the matrix, in all nickel– base alloys. γ' is present when aluminum and titanium are added in adequate amounts required to precipitates within the austenitic gamma matrix. The nature of the γ' precipitate is of primary importance in obtaining optimum high temperature properties (Davis, 1997).

Single-Crystal-Nickel Base Superalloys

Nickel base single crystal superalloys are precipitation strengthened cast monograin superalloys based on the NI-Cr-Al system. They have attracted considerable attention for use in rocket and gas turbine engines because of their high temperature properties. In high temperature application grain boundaries are typically the weak link, which provide passages for diffusion and oxidation, which results in failures at this location. Grain boundary strengtheners are added to the alloy chemistry to increase capability, which results in lowering the melting point of the alloy. Because of this entire single – crystal components are produced from one large grain. Removal of grain boundaries and grain boundary strengthening elements raise the incipient melting temperature of the alloy by 150°F and results in improved high temperature fatigue and creep capabilities (Stouffer and Dame, 1996). This increase in melt temperature permits higher heat treatment temperature that in turn yields improved creep capability. These single crystal superalloys are orthotropic and have highly directional material properties. The <001> direction is the most common primary growth direction for nickel- base superalloys (Davis, 1997).

Nickel–Base Superalloys Evolution: A General Literature Review

Nickel –Base superalloys have evolved over a period of 82 years. The first landmark in their evolution was laid with the development of Nimonic 80A (Ni-Cr alloy) a polycrystal / wrought superalloy (Dreshfield, 1986). To an extent, variations in chemical compositions through increasing element additions and introducing refractory metals improve the elevated temperature mechanical properties and surface stability of nickel base superalloys. During the 1940's an innovative process called the investment casting process was adopted from dental prosthesis technology. This technology enabled

the production of high precision components with complicated shapes. However, due to impurities problems, there were not many improvements in the mechanical properties and creep resistance, in the initial components processed by investment casting. Falih N. Darmara solved this problem in the 1950's with the invention of a new melting process called vacuum induction melting(VIM). This process, considered by many to be one of the most important advances in the evolution of superalloys, allowed for the development of alloys with increased quantities of reactive elements. Reactive elements such as aluminum and titanium, participate in the precipitation of coherent intermetallic precipitate gamma-prime phase Ni_3 (Al,Ti) (Fermin,1999).

Between the 1960's and 1970's, a further development in superalloy processing was introduced in order to increase the efficiency of the turbine performance by increasing the operating temperature and rotational speeds and reducing clearance between static and rotational components. This development was through the introduction of the directional solidification process developed by Frank Versnyder and others at Pratt and Whitney. This process produced significant improvements in the rupture life and thermal fatigue resistance of Ni-base superalloys. After about 10 years of research and investigation, the single crystal solidification process was developed, which was the result of minor variation in the directional solidification process. This minor variation in the directional solidification process yielded a significant increase in the thermal capability of nickel-base superalloys due to increased mechanical properties and thermal stability (Fermin, 1999). Figure 1-2 illustrates a comparison between polycrystalline, single crystal and columnar-crystal superalloys.

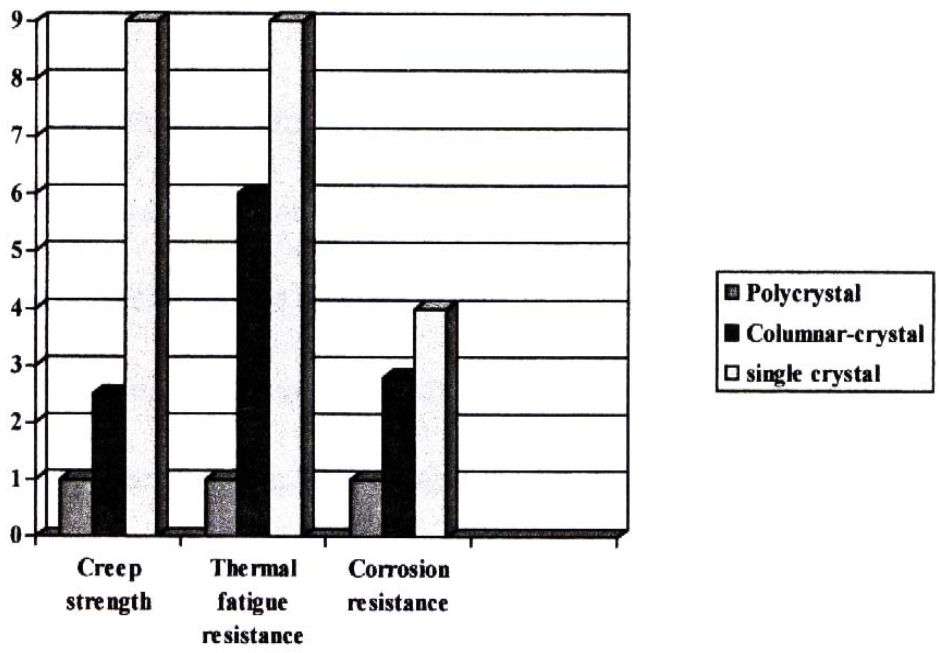

Figure 1-2 Comparative mechanical properties and surface stability of polycryatalline, directionally solidified and single crystal superalloys (Fermin, 1999)

Micro-Structural Properties of Ni-based Single Crystals.

The description of the macrostructure of Ni-based single crystals primarily consists of primary and secondary dendrites. Primary dendrites are parallel, continuous and span the casting without interruption in the direction of solidification. The secondary dendrite arms on the other hand are perpendicular to the direction of solidification and define the interdendritic spacing .The <001>family of direction is the one along which the solidification for both primary and secondary dendrite arms proceed.

The principal hardening mechanism in single crystal nickel-base superalloys is precipitation of gamma-prime, γ' (Deluca and Annis, 1995). The gamma prime precipitate is a face centered cubic (FCC) structure, composed of the intermetallic compound Ni_3Al .The γ' precipitate is suspended within the γ matrix, which is also of

FCC structure and comprised of nickel with cobalt, chromium, tungsten and tantalum in solution (Figure 1-3).

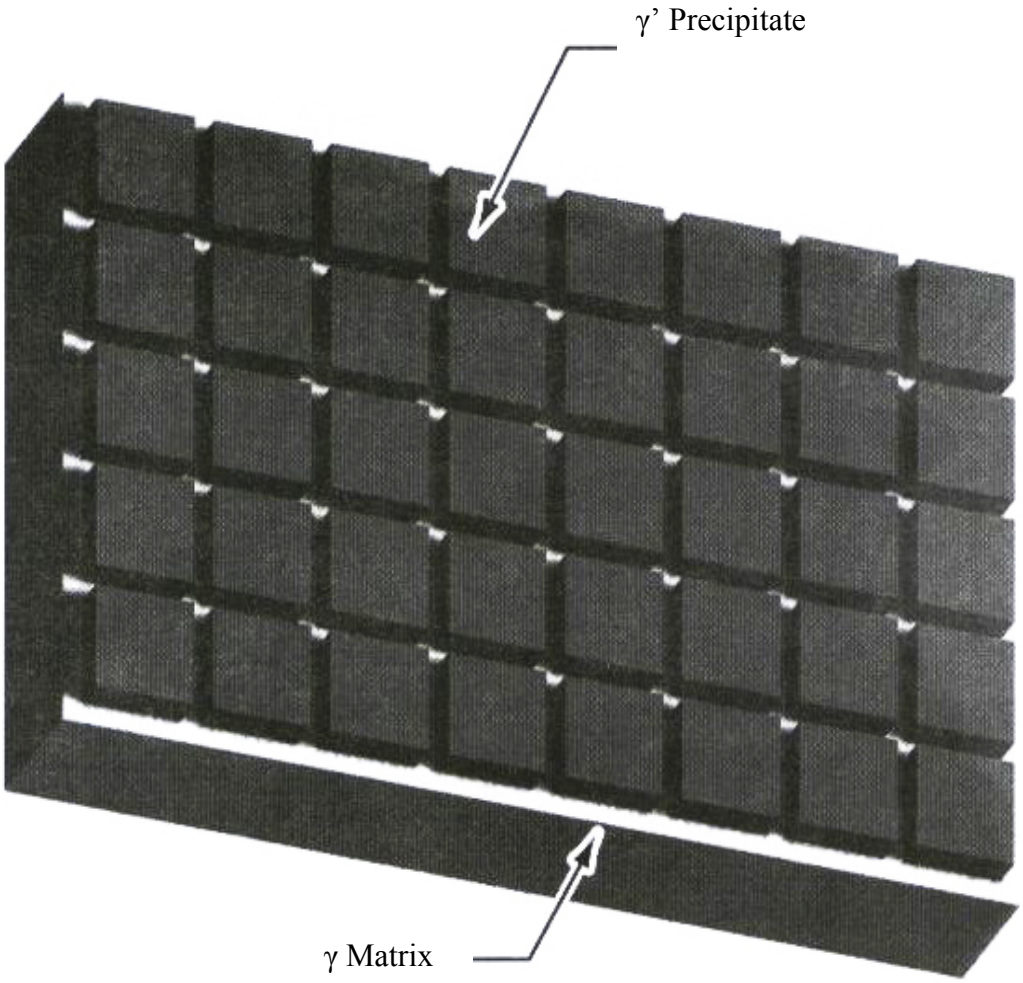

Figure 1-3 Microstructure showing γ matrix and γ' precipitate (Moroso, 1999).

Manufacturing of Single Crystal

Single crystals are manufactured by using techniques similar to those of directionally solidified castings with one important difference; that is by selecting a single grain with desired orientation. The first method for growing the single crystal uses a helical mold. In this method, a helical section of mold is placed between a chill plate and the part casting. A single grain is selected by the helix or spiral grain selector, which acts as a filter. This is because superalloys solidify by dendritic growth and each dendrite

can grow only in three mutually orthogonal<001>directions. Due to the combination of an orthogonal nature of dendritic growth and continually changing direction of the helix, a single crystal is emitted from the top of the helix. The second method is called seeding, which is capable of controlling both primary and secondary orientation. The seed crystal should be made of an alloy, which has equivalent or a higher melting temperature than molten alloy. The seed is placed on a chill plate where the temperature at the top of the seed is tightly controlled. This is done so that the seed crystal does not melt completely thereby allowing the molten alloy in the mold cavity to solidify with the same orientation as the seed (Davis, 1997). Both the methods are shown in Figure 1-4.

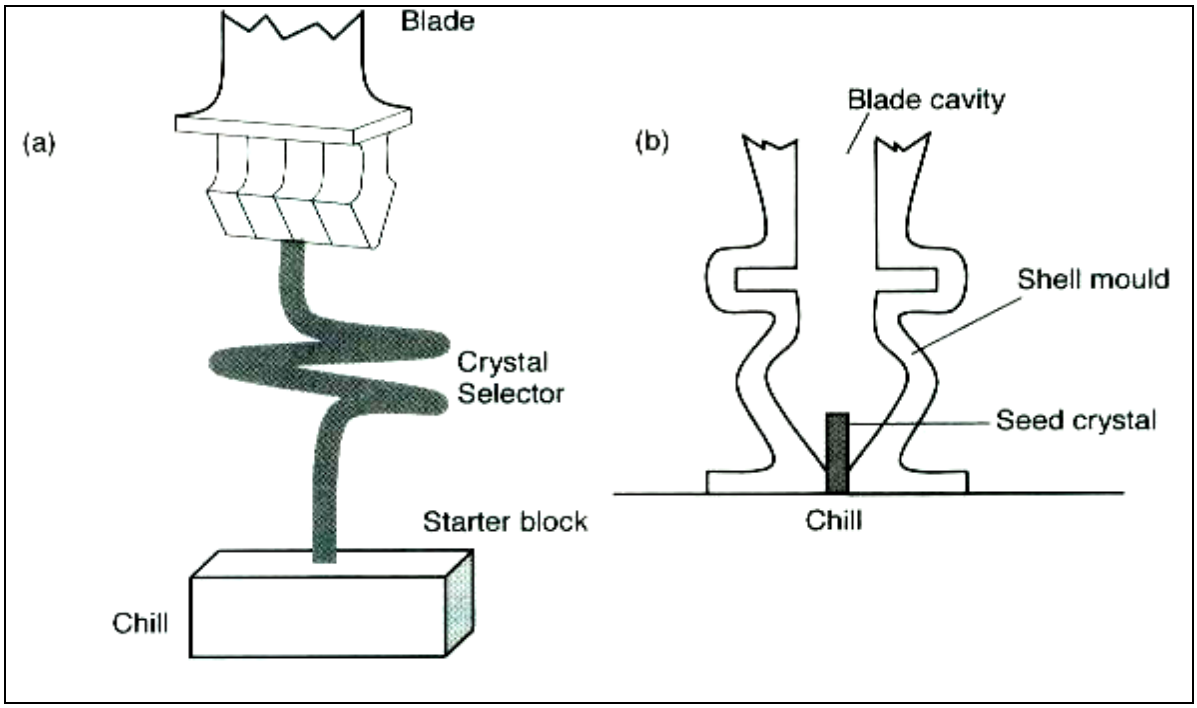

Figure 1-4 Single crystal blade production with: a) Crystal selector and b) Seed crystal. (Meetham, Voorde, 2000).

Deformation Mechanisms

Slip, climb and twinning are three main factors responsible for inelastic deformation in metals. The main reason for deformation of crystalline metals is the

propagation of dislocations through the metal's lattice when temperatures are less than 0.5 of the absolute melting temperature. At higher temperatures, deformation occurs by dislocation climb (which is a diffusion controlled process). Twinning, a rotation of atoms in the lattice structure, is not as important as strains are very small as compared to slip and climb. Plastic flow may result in an ideal crystal when one plane of atoms slides over another by the simultaneous breaking of all the metallic bonds between the atoms. However the actual yield stress is much lower than the theoretical shear stress, due to the presence of dislocation in the lattice structure. Dislocation is defined as a disruption in the crystal lattice structure of material (Stouffer And Dame, 1996).

Slip deformation is a stress-controlled process. The geometry of the crystal structure, magnitude of the shearing stress produced by external loads, and the orientation of the active slip planes with respect to the shearing stresses decides the extant of slip in single crystals. Slip begins when the shearing stress on the slip plane in the slip direction reaches a threshold value called the critical resolved shear stress (Dieter, 1986). The value of critical resolved shear stress depends chiefly on the material composition and temperature. It is also the function of applied load and direction, crystal structure and specimen geometry. During the application of a load to an FCC single crystal specimen, the first planes to get activated are the planes of high atomic densities and called the primary octahedral slip systems. A slip line or step is observed in experiments involving polished single crystals specimens (Figure1-5). Table 1-1 shows the 30 possible slip systems in an FCC crystal.

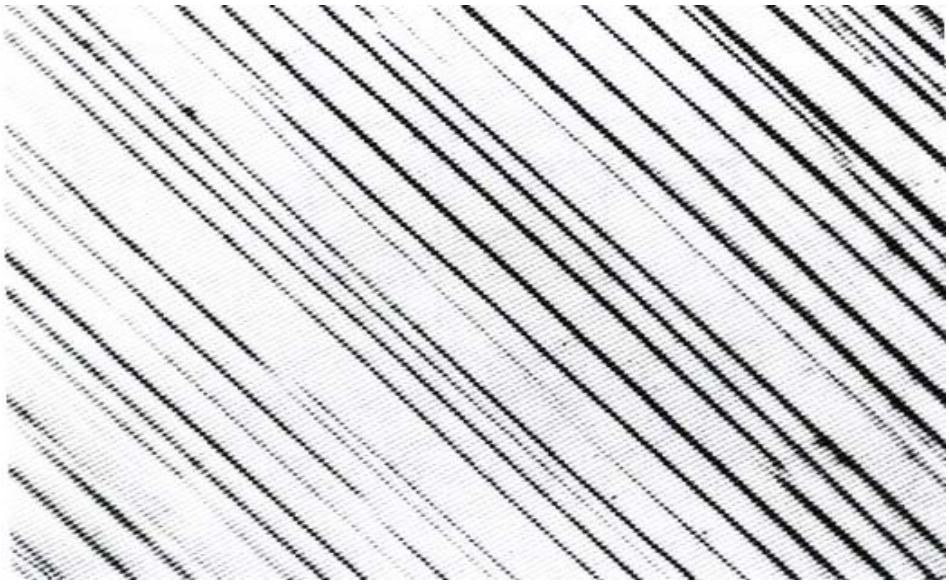

Figure 1-5 Straight up slip lines in copper (Dieter, 1986)

Slip will occur when the resolved shear stress (RSS) exceeds the yield strength of the material. However, in single crystal alloys the yield strength depends on the material orientation relative to the applied uniaxial load. Single crystal materials also have tension-compression asymmetry of the yield stress that is a function of orientation. A Sample loaded in the [001] direction, shows higher yield strength in tension than compression. In the [011] case, it is just the opposite.For the [111] orientation, the tension – compression asymmetry and orientation effects become negligible. When temperature increases above 700°C to 750°C, there is a sharp drop in the yield stress, and tension – compression asymmetry and orientation effects disappear. Test specimens near the [011] orientation generally show the lowest tensile strength and greatest ductility while specimens near the [111] orientation generally have the high tensile strength (Stouffer And Dame, 1996)

Table 1-1 Slip planes and slip directions in an FCC crystal.(Stouffer and Dame, 1996)

Slip Number	Slip Plane	Slip Direction
	Octahedral Slip a/2{111}<110>	Primary Slip Directions
1	(111)	[10-1]
2	(111)	[0-11]
3	(111)	[1-10]
4	(-11-1)	[10-1]
5	(-11-1)	[110]
6	(-11-1)	[011]
7	(1-1-1)	[110]
8	(1-1-1)	[0-11]
9	(1-1-1)	[101]
10	(-1-11)	[011]
11	(-1-11)	[101]
12	(-1-11)	[1-10]
	Octahedral Slip a/2{111}<112>	Secondary Slip Directions
13	(111)	[-12-1]
14	(111)	[2-1-1]
15	(111)	[-1-12]
16	(-11-1)	[121]
17	(-11-1)	[1-1-2]
18	(-11-1)	[-2-11]
19	(1-1-1)	[-11-2]
20	(1-1-1)	[211]
21	(1-1-1)	[-1-21]
22	(-1-11)	[-21-1]
23	(-1-11)	[1-2-1]
24	(-1-11)	[112]
	Cubic Slip a/2{100}<110>	Cube Slip Directions
25	(100)	[011]
26	(100)	[01-1]
27	(010)	[101]
28	(010)	[10-1]
29	(001)	[110]
30	(001)	[-110]

Motivation for the Thesis

In modern military gas turbine engines, various causes of component failure are low cycle fatigue, corrosion, overstress, manufacturing processes, mechanical damage and the types of materials used. However the single largest cause of component failure is attributed to high cycle fatigue (HCF) (Cowles, 1996) (Figure 1-6).

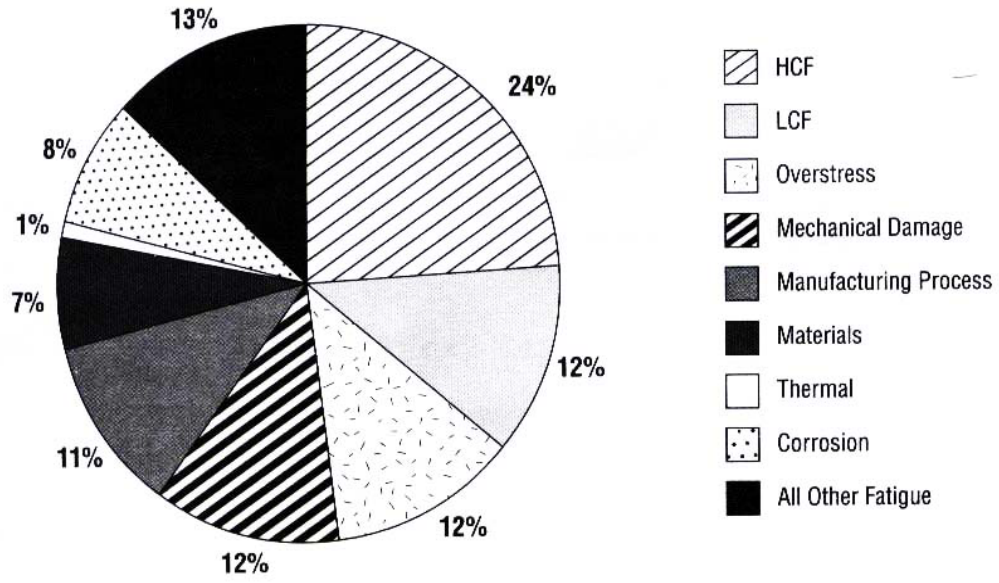

Figure 1-6 Representative jet engine component distress mode statistics.(Cowles, 1996).

The problem of high cycle fatigue is a pervasive one, affecting all turbine engine parts made from a wide range of materials (Figure 1-7). The components most likely to fail by HCF are turbine and compressor blades.

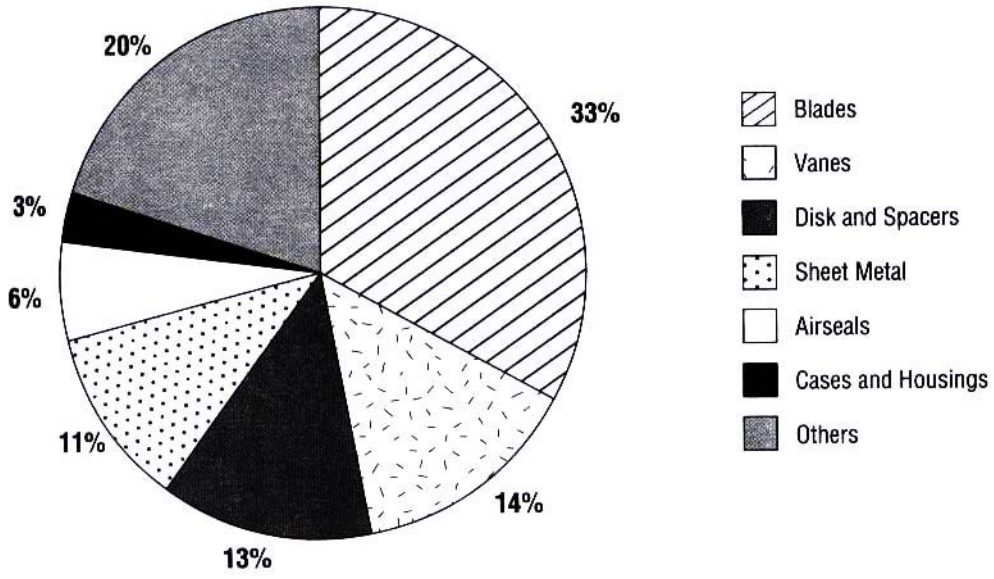

Figure 1-7 Representative distributions of HCF problems by components.(Cowles, 1996).

Need for the Study

Potential cause of HCF in gas turbines is presence of vibratory stresses. Turbine blades are particularly susceptible to damage by vibratory high cycle fatigue due to the large range in frequency responses excited by rotation. Such vibratory stresses are further superimposed by cyclic and steady stresses induced by thermal and mechanical loads. Due to these loads, cracks fatigue can nucleate in regions of high stress concentrations, and eventually propagate and cause blade failure.

To develop a mechanistically based life prediction systems, an understanding of evolution of slip systems in regions of stress concentration, under the action of 3-D fatigue stresses, is necessary. The planes, on which crystallographic fatigue cracks initiate in 3-D stress fields and their crack propagation rates, are essential for life prediction.

At a first step towards realizing this goal, the understanding of evolution of slip systems in a single crystal specimen, under the action of 3D static stress is important. A double-edged notched rectangular tension test single crystal is used to simulate 3D stress fields. Slip fields activated near the notch during tensile loading are observed experimentally (Material Science And Engineering Department, University of Florida). Three-dimensional FEA of the specimen is used to predict the slip systems. Analysis results are verified by comparing with experimentally generated slip fields.

CHAPTER 2
PLASTIC DEFORMATION AROUND A NOTCH TIP

This chapter contains a general review of the literature published in the area of stresses and sectors around a notch tip. The information will provide the necessary a background to understand the slip mechanism and plastic deformation near a notch tip. Investigation of the plastic deformation at a crack tip in a single crystal is important to the development of the understanding of single crystal failure. Plastic fields, with sectors of deformation and crystallographically dependent radial boundaries are produced by the plastic deformation around a crack tip in a single crystal material. In 1987, Rice had predicted plastic deformation around a crack tip in metallic single crystals. These results were confirmed experimentally (Shield and Kim, 1994; Shield, 1996) and investigated numerically (Rice et al., 1990; Mohan et al., 1992). Currently, no analytical or numerical work exists which provides insight into the slip system behavior of ductile anisotropic single crystals in the presence of a crack or notch or which can completely predict the behavior observed in experiments.

Slip Mechanism

In a single crystal specimen, the extent of slip depends on the magnitude of the shearing stress produced by external loads, the crystal structure geometry and the orientation of the active slip planes with respect to the shearing stresses. Therefore the stress - strain behavior of a material, which is a function of the number of activated slip systems, varies with orientation (Figure 2-1).

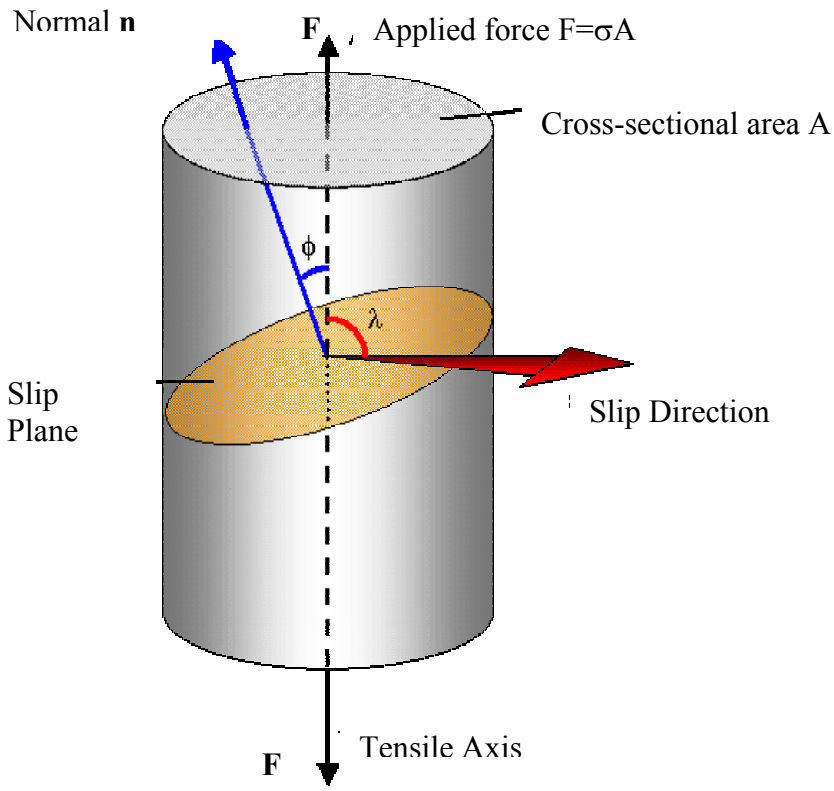

Figure 2-1 Calculation of resolved shear stress parallel to slip direction, from tensile force F.(Dieter,1986).

When a load is applied slip systems get activated based on Schmid factor, m.

Where $m = \cos\lambda \times \cos\phi$ (2-1)

Where ϕ is the angle between the tensile axis and the normal to the slip plane and λ is the angle between the slip direction and the tensile axis. From eq.2-1 its clear that the Schmid factor is also a function of the load orientation and slip plane orientation.

It has been observed experimentally that a single crystal will slip when the resolved shear stress on the slip plane reaches the critical resolved shear stress for that material.

$$\tau_{RSS} = m \times \sigma \qquad (2\text{-}2)$$

Where σ is the load applied and τ_{RSS} is the resolved shear stress. This behavior is known as Schmid's law. However, agreement to Schmid's law has been proven only with isotropic materials, and its correlation to single crystals is not yet known. Therefore, another method must be used to predict RSS values and slip activation for these anisotropic materials.

Work of Prominent Researchers in the Field

Rice (1987)

Rice analyzed crack tip stress and deformation fields for ideally plastic tensile loaded crystals, by examining the mechanics of both FCC and BCC notched specimens. Rice presented the analysis for plane strain tensile cracks. He also used critical resolved shear stress criteria to predict sectors. He paid attention to two specific crack orientations in FCC and BCC crystals, although the analysis techniques are applicable to other orientations too. One orientation defined the notch plane as (010), the notch growth direction as (101) and the notch tip direction as (10-1). The second orientation defined the notch plane as (101); the notch growth direction as (010) and the notch tip direction as (10-1).

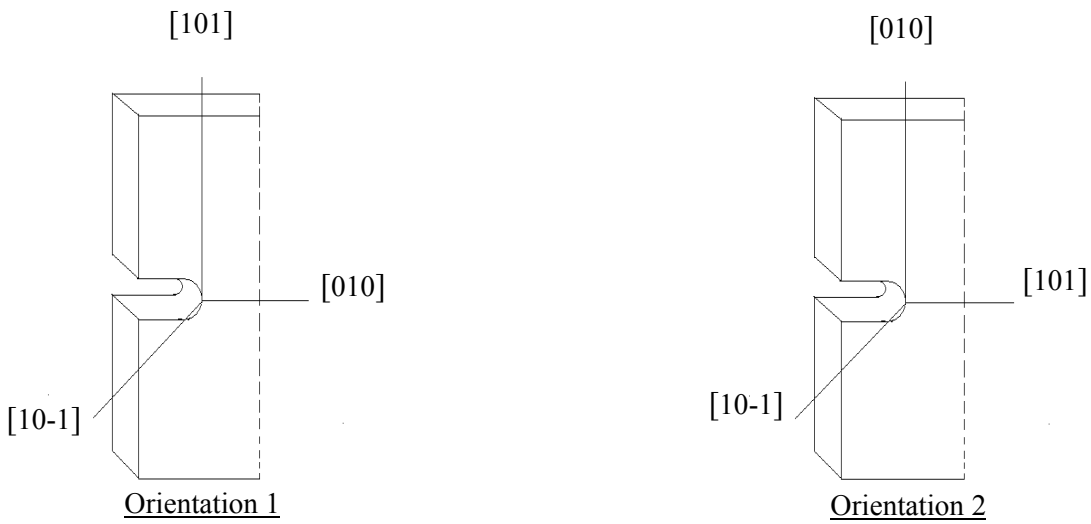

Figure 2-2 Orientations of specimens used by rice. (1987)

Rice analyzed both orientations and derived analytical solutions to predict the active slip systems and to determine sectors around the notch. Rice considered only the positive half of the plane for both of the cases since the solution is symmetric about the notch growth axis. He found a continuous solution with respect to the radius and angular displacement.

The main drawbacks in rice solutions are 1) He did not include anisotropy in his model, so his solution cannot validate the experimental results, 2) His solutions cannot determine detailed strain field data based on the state of stress near the tip, 3) His solutions show no difference between either orientation's sector boundaries or between FCC and BCC crystal structure. Both orientations predict boundaries at 55º, 99º and 125º.

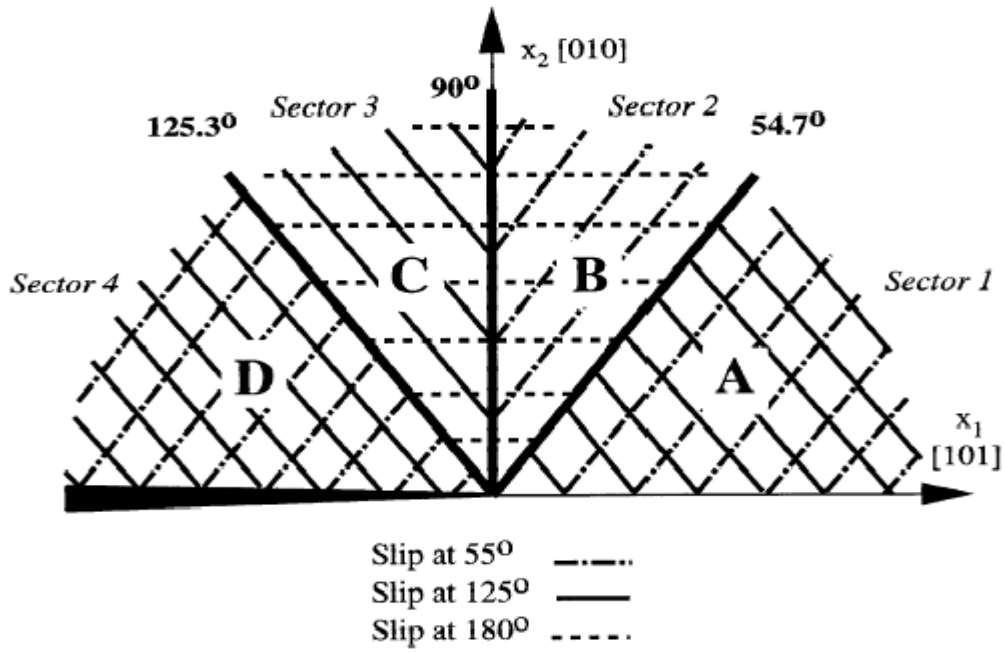

Figure 2-3 Rice's perfectly plastic analytical solution for orientation 2. (Crone and Shield, 2001).

The families of slip plane traces in the FCC and BCC case are identically oriented relative to one another, except that the slip plane traces for the BCC families are rotated by 90º relative to the traces for the FCC families. For example if N=X and S=Y describe a particular FCC family, then N=Y and S= X describe a corresponding BCC family, where N is the unit normal to a slip plane and S is a unit vector. Thus orientation had no effect on the sector boundaries. Rice also neglects strain hardening, because of which there is no effect of plastic deformation on yield locus.

Shield and Kim (1993)

Shield and Kim followed the work of Rice to correlate their experimental solution with Rice's analytical solution. Results are presented for determining the plastic deformation fields near a crack tip (200μm wide notch) in an iron – 3% silicon single

crystal (Specimen FE-11). The notch in Shield and Kim's specimen was in a (011) plane with prospective crack growth in a [100] direction.

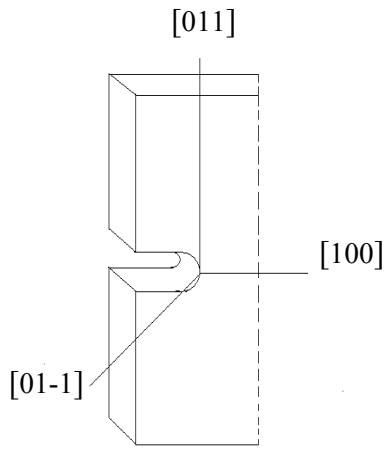

Figure 2-4 Orientation of specimens used by shield (1993).

Since the solution is symmetric about the [100] axis, only the upper half- plane was considered. The specimen was loaded in four-point bending with measurements were made at zero loads after extensive plastic deformation has occurred (Figure 2-5).

Rice presented an asymptotic analysis of the plane strain stress field at a crack tip in a perfectly plastic crystal. Subsequently, Saeedvafa and Rice (1998) extended this analysis to include Taylor power –law hardening and presented an asymptotic solution of the plane strain crack tip stress field which we will refer to as an HRR type solution.

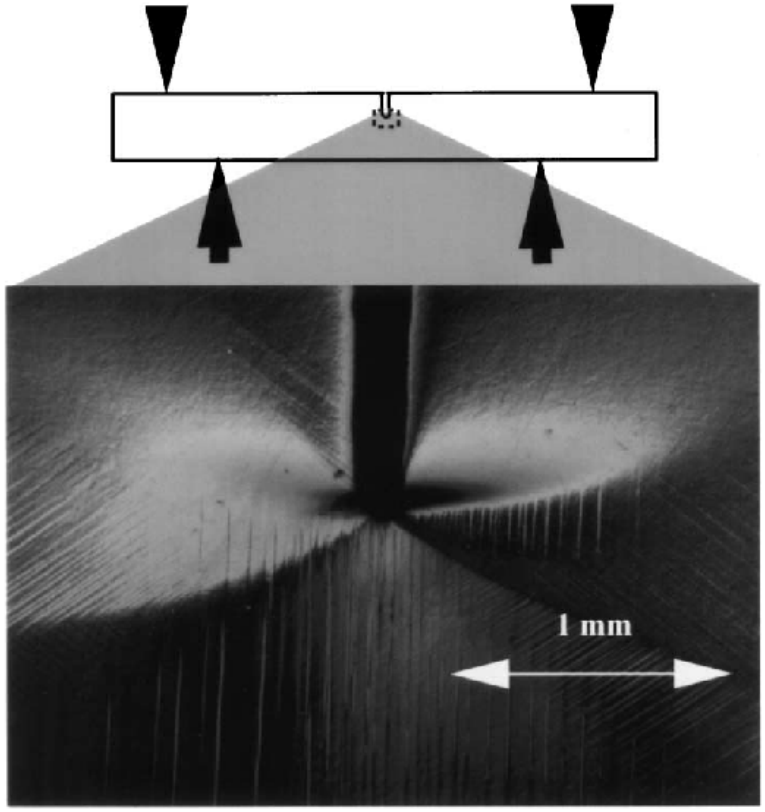

Figure 2-5 Specimen loaded in four-point bending by crone and shield. (Crone and Shield, 2001).

Shield et al. predicts slip sectors, similar to Rice, based on plastic strain field data. They assumed that the total strain was equal to plastic strain and neglected the elastic strain. The specimen they considered had dimension of 7.45 mm $\times$6.00mm $\times$26.05 mm. The bar was extended to a length of 51.95 mm by welding 12.95 mm long polycrystalline bars of the same cross-section to each end. They introduced a single- edge notch at the center of the crystal to a depth of 2.05mm and a width of 200μm. To verify that the surface strains reflect the behavior of the material in the interior of the specimen, the specimen was sectioned and etched. Shield and Kim present strains as a function of angle, since the strains do not vary much with radial distances from the notch tip. The

angle was measured from the crack propagation direction and was taken as positive in the counterclockwise direction.

From the experiment a pattern of four (eight symmetric) sectors were found. This pattern is shown in Figure (2-6).

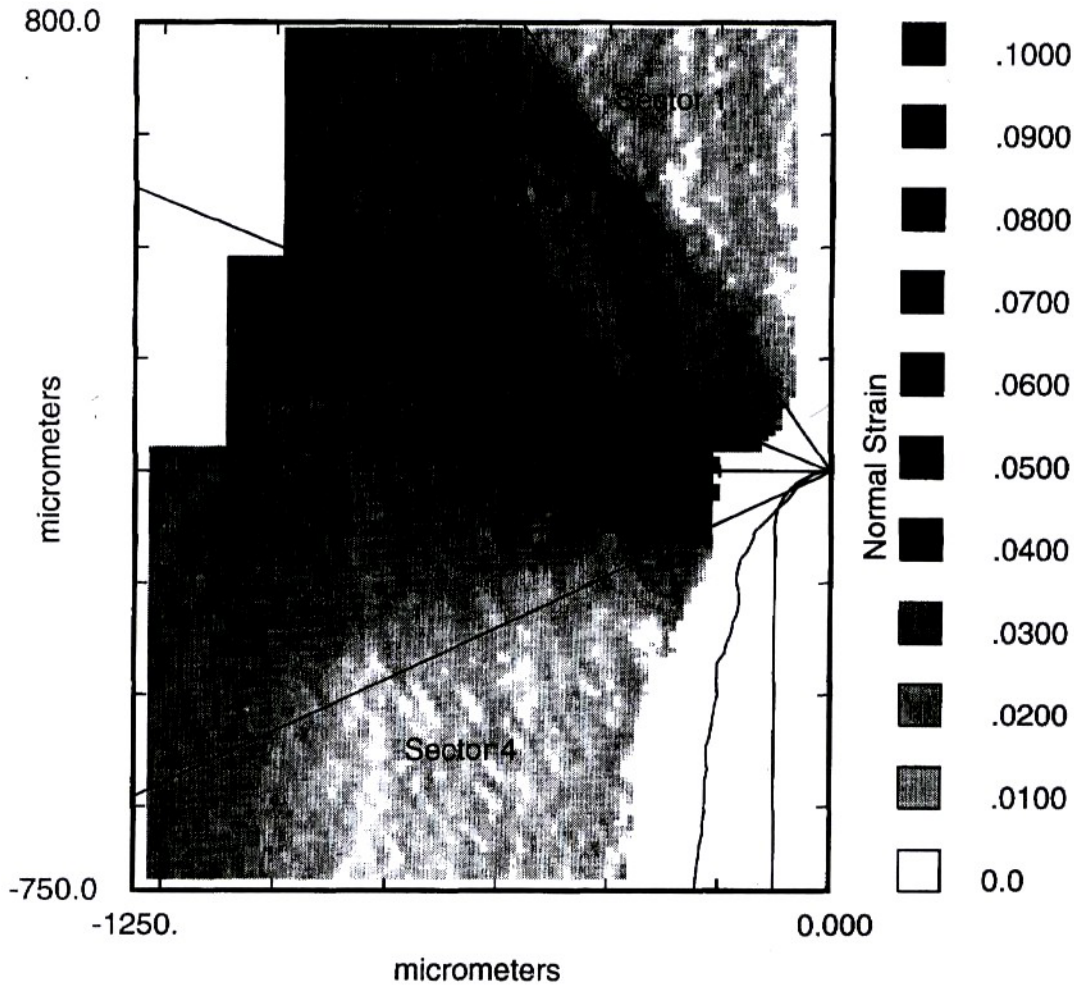

Figure 2-6 The E_{22} strain components near a notch in an iron – silicon single crystal. (Shield, 1995).

The figure displays the E_{22} strain component. Sectors 1 and 2 have constant strains, although section 2 had some small variations. The third sector has the largest strain values and they vary with radius in an approximately 1/r manner. The fourth sector has roughly constant strain, though the strain levels are too low to make an absolute

statement. An excellent agreement between the interior dislocation pattern and surface strains was found. Thus the surface measurements accurately reflect the deformations that are occurring in the interior of the specimen and a comparison with the plane strain result of Rice is justified.

Shield (1995)

Following his work on iron-silicon single crystal Shield extended his work to copper single crystals. He chose the study of {110} as a crack plane with the prospective crack growth direction in the [100] direction. This is the same orientation as the iron-silicon specimen (FE-11). Because, iron- silicon has a BCC structure and copper has a FCC structure, the slip systems in the two materials are different. However, since the orientations are the same, it will be possible for a direct comparison to be made on the basis of orientation. Also, the effect of the different slip systems on the strain fields can be assessed.

Shield compared this work with his previous work and concluded that the discrete sectors observed in FE-11 are also present in this specimen. The sector boundary angles are similar to, but not exactly the same as those observed in FE-11, which has same orientation but different slip systems (Table2-1).

Table 2-1 Orientation II sector boundary angle comparisons.

	FE-11 (bcc)	C1-B1 (fcc)	Rice (1987)
	Sector boundary angles (degrees)		
1-2 boundary	35	43	55
2-3 boundary	65	62	90
3-4 boundary	110	100	125

(Modified from Crone and Shield, 2001)

The greatest difference in sector boundary angles occurs in the 1-2 sector boundary. The angle of maximum strains (in sector 3) is almost identical in both

specimens, suggesting that this angle may be more related to the notch tip geometry than the crystal structure. Shield also observed that load had no effect on sector boundary angles. However, as the load increased, the amount of plasticity near the notch tips also increases. Shield also observed that results obtained for low loads show similarities to Rice's model but Shield's experimental results do not correlate to Rice's model at high plastic strain (Table 2-1). The boundary angles between the two samples were similar but not constant. This disagreement can be due to the material structure alone or due to flaws that may be present in the material structure, regardless of a constant specimen orientation and test condition. This can also be due to the geometry of the notch, which is very difficult to duplicate accurately.

Shield observed slip lines which are caused by plastic deformation at large strains. He then compared results with strain sectors determined by a Moiré interferometer. He found that the sector boundary angles determined by Moiré's interferometer matched well with the strain field images. The contradictory results of Shield's experiment and Rice's results provoke the need to replace the existing model, which can provide more accurate solutions.

Crone and Shield (2001)

Crone and Shield extend the work of Shield (1995) by experimentally studying notch tip deformation in two different orientations. Moiré microscopy was used to measure the strain field on the surface of the bending samples. Two crystallographic orientations were considered in this research. Orientation 1 is defined as the orientations containing a crack or notch on the (101) plane and its tip along the [10-1] direction. This orientation was investigated experimentally by Shield (1995) and Shield and Kim (1994).

Orientation 2 is defined as the orientation containing a crack or notch on the (010) plane with a tip along the [-101] direction. Experimental results for these orientations were found. The plane of observation was the same for these two orientations with the crack or notch being rotated by 90°. Both orientations were analytically investigated by Rice (1987).

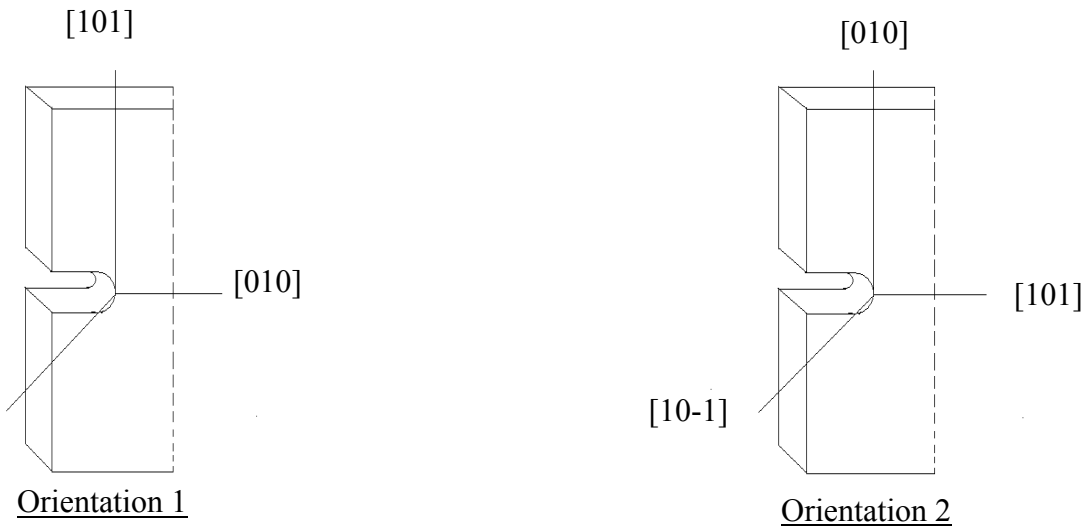

Figure 2-7 Orientations of specimens used by crone and shield. (2001)

Crone and Shield compared their experimental results with Rice's analytical solution as well as with a numerical solution by Mohan et al. (1992) and Cuitino and Ortiz (1996) (Table 2-2). Rice's analytical solution was applied to both orientations 1 and 2 where the plane of observation was the same with the notch being rotated by 90°. The numerical solutions are based on plane strain assumptions even though Cuitino and Ortiz concluded that the problem under consideration is not a plane strain because of

differences between the interior and surface fields. Even with the plane strain assumptions Rice's analytical solutions do not match with Crone and Shield's experimental results.

Table 2-2 Comparisons of experimental sector boundary angle with numerical and analytical solutions of orientation II.

Sector boundary	Experimental	Analytical	Numerical	
In degrees	Crone and Shield (2001)	Rice (1987)	Mohan, et al. (1992)	Cuitino and Ortiz (1996)
1-2	50-54	54.7	40	45
2-3	65-68	90	70	60
3-4	83-89	125.3	112	100
4-5	105-110		130	135
5-6	150			

(Modified from Crone and Shield, 2001)

Orientations 1 and 2 are related by a 90° rotation about the x_3 axis. This means that orientation 1 represents orientations 2 rotated by 90° about the notch tip direction, such that the notch growth direction and notch plane directions are switched. The experimentally determined sector boundary angles for both orientations are compared in Table 2-3.

Table 2-3 Experimental sector boundary angles for copper samples.

Sector boundary	Orientation I	Orientation II
Boundary angles in degrees	(101) Plane	(010) Plane
1-2	35-40	50-54
2-3	54-59	65-68
3-4	111-116	83-89
4-5	138	105-110
5-6		150

(Modified from Crone and Shield, 2001).

Contrary to the equivalent sectors predicted by Rice, there are several clear differences between orientations 1 and 2 predicted by Crone and Shield.

Here, the experimental results are fairly unclear due to the "annulus of validity" where Crone and Shield take their measurements. The annulus chosen following Shield and Kim (1994) corresponds to the area from 350-750μm from the notch tip. This annulus was chosen to avoid inclusion of material close to the notch. Behaviour of material close to the notch is dominated by the notch geometry while behaviour of material in the far field may be affected by specimen boundaries.The annulus was also chosen to place the sectors well out of the range of any plastic deformation and can be used where only elastic deformation is taking place.

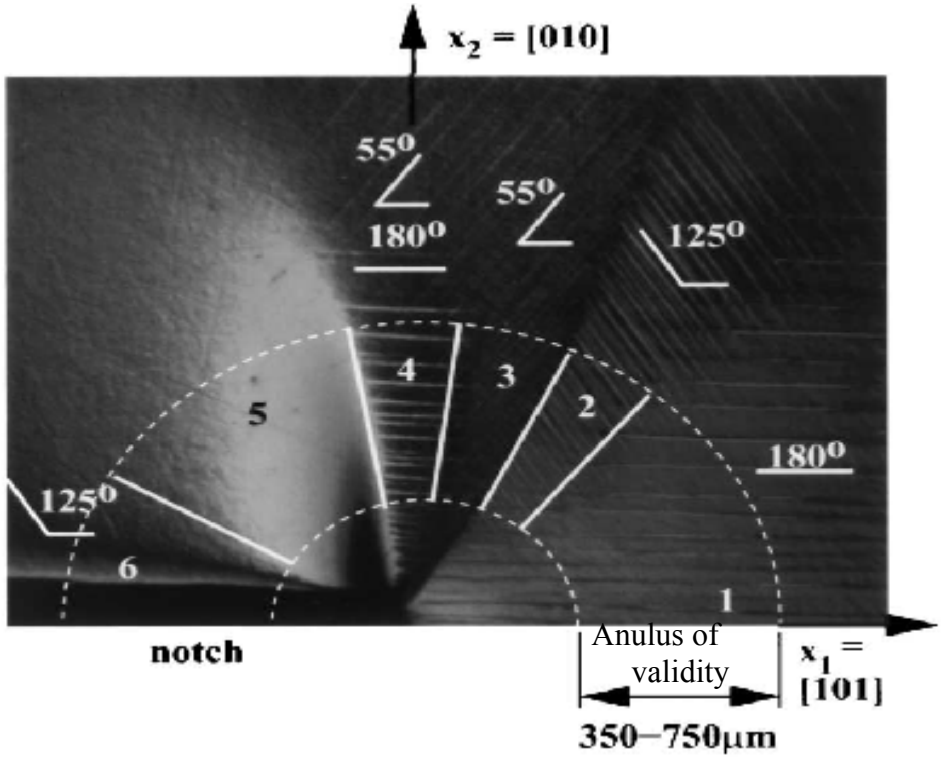

Figure 2-8 Experimental slip sectors from crone and shield. (Modified from Crone and Shield, 2001).

Here, the research presented has further confirmed that the structure of the deformation field near a notch in a metallic single crystal is linked to crystallographic orientation. Although Rice (1987) captures the main features of the deformation

experimentally observed near a notch in FCC copper and copper-beryllium single crystal, a more complex 3 Dimensional anisotropic analytical solution is required to account for the sector boundary angles and the elastic sectors noted in these experiments. Research is currently underway to develop an analytical solution that more closely correlates with the experimental findings.

CHAPTER 3
3D STRESS ANALYSIS OF SINGLE CRYSTAL NOTCHED SPECIMENS USING FEM

Introduction

In the field of linear elastic fracture mechanics, various test methods have been developed in order to study the elastic response of isotropic-notched specimens under the action of tensile load. The following are the test methods developed for the above study: Analytical Approach, Numerical Approach and Experimental Approach. The methods developed for isotropic specimens pose many difficulties when applied to three dimensional anisotropic specimen models. For example, In case of the isotropic analytical models, the current solution relies on many simplifications/approximations that lead to inaccurate results when compared with the experimental results. However these limitations in the elastic models are overcome by the use of the three-dimensional FEA approach, which enables solutions that correlate well with actual experimental results. Moreover, unlike the analytical solutions, both the numerical and experimental model specimen have the capability of using notched specimens which act as very simplified cracks to model fracture behavior. The study of the elastic response of anisotropic specimens is also useful to find the multi-axial loading strength of the specimen.

Close Form Solution for a Uniaxially Loaded, Smooth, Single Crystal Specimen.

Anisotropic materials play an important role in many phases of modern technology. They are used widely in areas like material sciences, solid-state physics, missile and aircraft manufacturing and many others. Thus this sophisticated technology

requires the study of the properties of anisotropic materials, particularly the elastic properties of these materials in various directions. Unlike in the past, where the materials were consider to be homogenous and isotropic in order to simplify calculations, it is unfeasible today to make such oversimplified assumptions as these will lead to inadequate and incorrect results.

The test specimen chosen for the study is a notched single crystal super alloy. The objective of the study is to find the state of stress in the material co-ordinate system of the specimen and consequently calculate the resolved shear stresses in the 12 primary slip systems of critical locations. In an isotropic material a single elastic constant governs the transformation from stress to strain and properties of materials do not vary with directions. But this is not the case with anisotropic material, in this the elastic constant of a crystal vary markedly with orientations. The stress strain relationship for an anisotropic solid with cubic symmetry has three independent constant (elastic modulus, shear modulus and Poisson ratio) in the material co-ordinate system, as well as stress tensor matrix instead of single elasticity constant that varies with orientation (Lekhnitskii, 1963).

Coordinate Transformation for Orthotropic Material

The definition of the elasticity matrix requires the determination of the precise orientation of the actual specimen. This may be done either in terms of the material miller indices or angular measurements. A co-ordinate transformation is essential in the case of physical material test specimen, due to the difficulty encountered while cutting the sample such that the x, y and z test axes be perfectly aligned along the material axes:

[100], [010] and [001] respectively. Such a co-ordinate transformation will translate the known specimen stresses in terms of the material co-ordinate systems.

Outlined below are the transformation procedure derived from Lekhnitskii and Stouffer and Dame. There are two approaches to the transformation from the specimen to the material co-ordinate system. First approach is the direct measurement of the angles between the original and the transformed co-ordinate systems to find the directions cosines. This approach is suitable if the angles are easily found. Second approach is to find the miller in dieses of the transformed axes, which are rotated through a series of steps to arrive at the final transformed destination. This method is based on rigid body rotations and is more suitable for complex orientations, where the angles between the two co-ordinate systems are difficult to find. Although neither method is preferred over the other, the first method (angle measurement) turns out to be more convenient in the case of experimental specimens.

Coordinate Axes Transformation

Knowing the orientation of the sample, one can perform the co-ordinate transformation and the transformation matrices can then be used to determine the stresses and strains resolved on any given plane and slip system. Here the material co-ordinate system is denoted by x_1, y_1, and z_1 and the specimen co-ordinate system is denoted by x’”, y”’, and z”’. The original coordinate system is the material coordinate system and the transformed coordinate system is defined as the specimen coordinate system, and is at some angular displacement from the original axes.

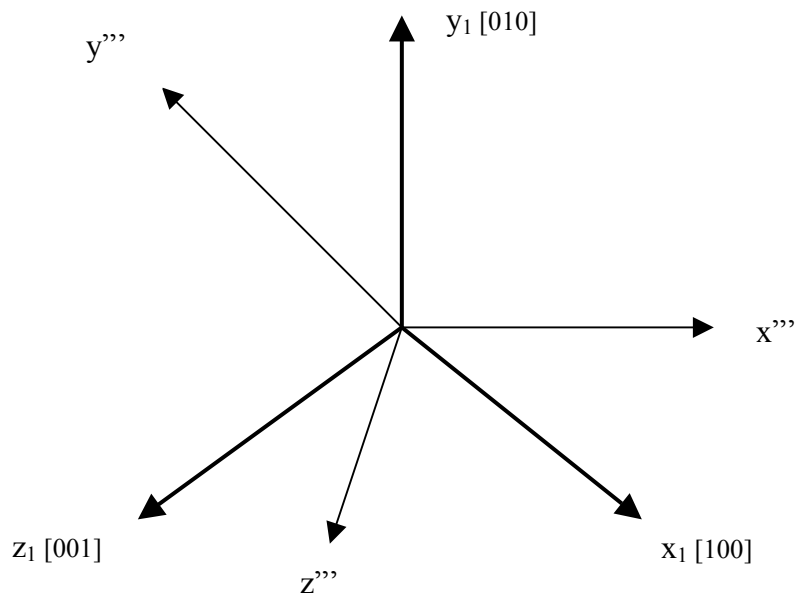

Figure 3-1 Material (x_1, y_1, z_1) and specimen (x''', y''', z''') coordinate system.

By breaking the total transformation into several rigid rotations, transformations from material co-ordinate system to the specimen coordinate system is done. The first transformation, to the x', y' and z' axes, is performed by rotating by ψ_1 about the z_1-axis (Transformation from x_1 toward y_1 is defined as positive).

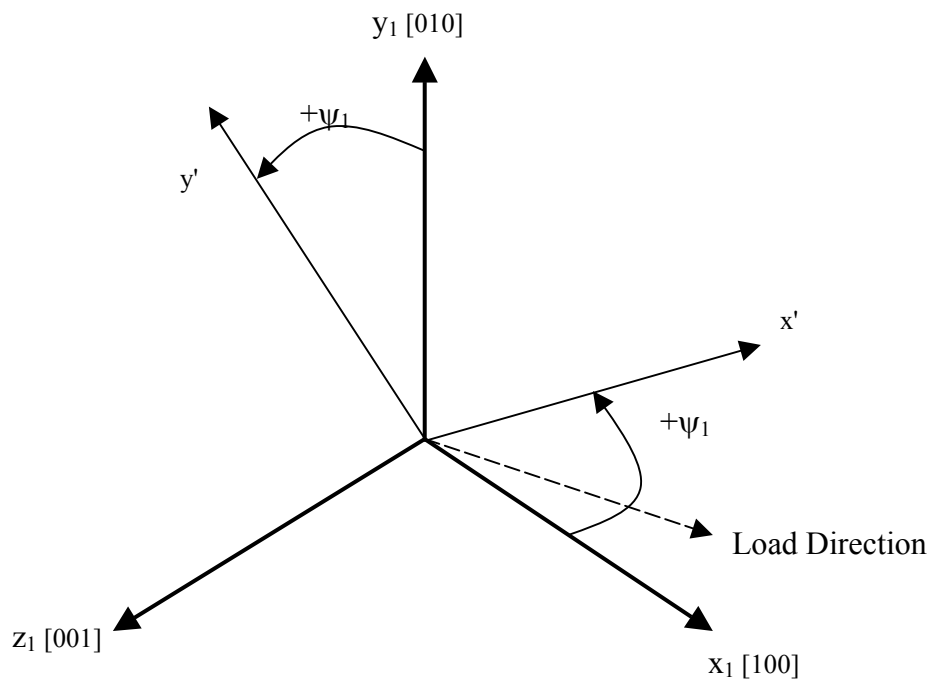

Figure 3-2. First rotation of the material co-ordinate system by angle $+\psi_1$ about the z_1 axis.

Here the x', y' and z' represents the transformed coordinates, in terms of the original coordinates after first rotation by angle $+\psi_1$.

$$x' = x_1 \cdot \cos(\psi_1) + y_1 \cdot \sin(\psi_1) \tag{3-1}$$

$$y' = -x_1 \cdot \sin(\psi_1) + y_1 \cdot \cos(\psi_1) \tag{3-2}$$

$$z' = z_1 \tag{3-3}$$

Writing the transformation in matrix form is:

$$\begin{pmatrix} x' \\ y' \\ z' \end{pmatrix} = \begin{pmatrix} \cos(\psi_1) & \sin(\psi_1) & 0 \\ -\sin(\psi_1) & \cos(\psi_1) & 0 \\ 0 & 0 & 1 \end{pmatrix} \cdot \begin{pmatrix} x_1 \\ y_1 \\ z_1 \end{pmatrix} \tag{3-4}$$

The second transformation, to the x", y" and z" axes, is done by rotating by ψ_2 about the y' axis (Transformation from z' toward x' is defined as positive).

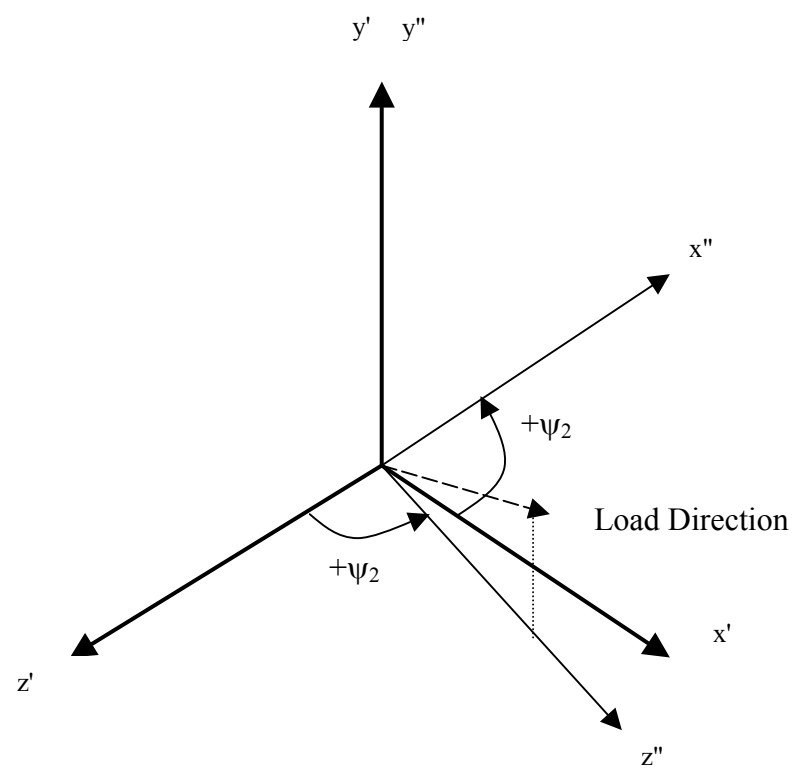

Figure 3-3. Second rotation by angle $+\psi_2$ about the y' axis.

Now the second transformation in matrix form is:

$$\begin{pmatrix} x'' \\ y'' \\ z'' \end{pmatrix} = \begin{pmatrix} \cos(\psi_2) & 0 & -\sin(\psi_2) \\ 0 & 1 & 0 \\ \sin(\psi_2) & 0 & \cos(\psi_2) \end{pmatrix} \cdot \begin{pmatrix} x' \\ y' \\ z' \end{pmatrix} \tag{3-5}$$

The final transformation to the specimen coordinate system (x’’’, y’’’ and z’’’ axes) is done by rotating the y” and z” axes by angle ψ_3 about the x”-axis (Transformation from y” toward z” is defined as positive).

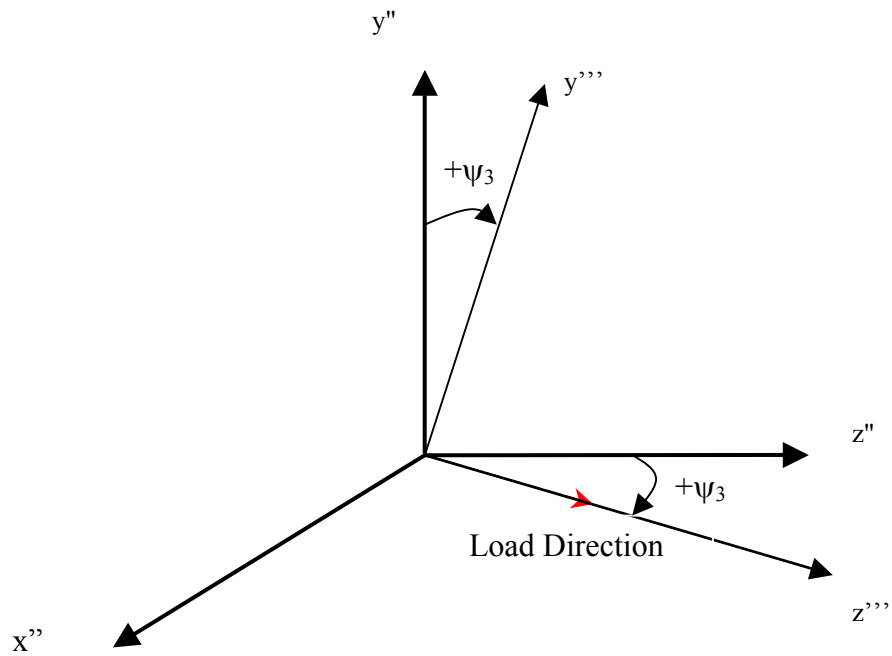

Figure 3-4. Third rotation by angle $+\psi_3$ about the x” axis.

The third transformation in matrix form can be written as:

$$\begin{pmatrix} x''' \\ y''' \\ z''' \end{pmatrix} = \begin{pmatrix} 1 & 0 & 0 \\ 0 & \cos(\psi_3) & \sin(\psi_3) \\ 0 & -\sin(\psi_3) & \cos(\psi_3) \end{pmatrix} \cdot \begin{pmatrix} x'' \\ y'' \\ z'' \end{pmatrix} \tag{3-6}$$

By multiplying the three transformations (Individual step matrices) the total transformation can be calculated. (The first transformation becomes the last one multiplied):

$$\begin{pmatrix} x''' \\ y''' \\ z''' \end{pmatrix} = \begin{pmatrix} \alpha_1 & \beta_1 & \gamma_1 \\ \alpha_2 & \beta_2 & \gamma_2 \\ \alpha_3 & \beta_3 & \gamma_3 \end{pmatrix} \cdot \begin{pmatrix} x_1 \\ y_1 \\ z_1 \end{pmatrix} \tag{3-7}$$

Where

$$\begin{pmatrix} \alpha_1 & \beta_1 & \gamma_1 \\ \alpha_2 & \beta_2 & \gamma_2 \\ \alpha_3 & \beta_3 & \gamma_3 \end{pmatrix} = \begin{pmatrix} 1 & 0 & 0 \\ 0 & \cos(\psi_3) & \sin(\psi_3) \\ 0 & -\sin(\psi_3) & \cos(\psi_3) \end{pmatrix} \cdot \begin{pmatrix} \cos(\psi_2) & 0 & -\sin(\psi_2) \\ 0 & 1 & 0 \\ \sin(\psi_2) & 0 & \cos(\psi_2) \end{pmatrix} \cdot \begin{pmatrix} \cos(\psi_1) & \sin(\psi_1) & 0 \\ -\sin(\psi_1) & \cos(\psi_1) & 0 \\ 0 & 0 & 1 \end{pmatrix} \quad (3\text{-}8)$$

The following results represent the direction cosines between the material and the specimen coordinate system axes.

Table 3-1. Direction cosines

	x_1	y_1	z_1
x'''	α_1	β_1	γ_1
y'''	α_2	β_2	γ_2
z'''	α_3	β_3	γ_3

Several checks based on perpendicularity can be performed to make sure that a proper orthogonal coordinate transformation has been done (Appendix).

<u>Example Problem</u>

Consider a specimen loaded in the [314] direction (Figure 3-6)

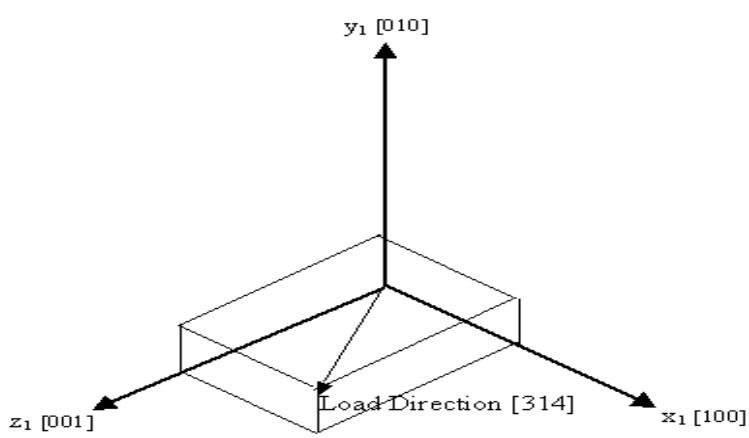

Figure 3-5. Figure showing the load direction.

The coordinate transformation is reduced to two rigid body rotations ψ_2 and ψ_3 since $\psi_1 = 0$.In second step load vector is reflected onto the x_1-z_1 plane. The reflection shows a triangle whose sides are the u and w Miller indices: u= 3, w = 4.

The first angular translation, ψ_2, is:

$$\psi_2 := \operatorname{atan}\left(\frac{u}{w}\right) \qquad (3\text{-}9)$$

$\psi_2 = 36.87^\circ$

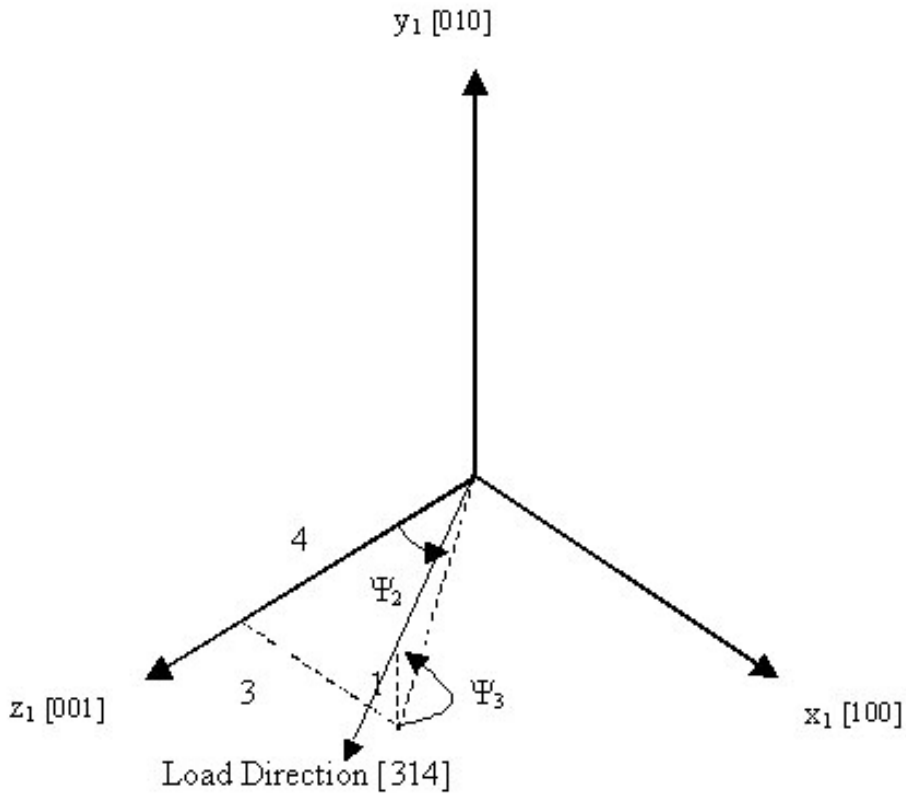

Figure 3-6. Figure showing total transformation.

In the same way, the second angle, ψ_3, forms a triangle with the hypotenuse, *h*, of the first reflection and the y-translation: $h = \sqrt{u^2} + \sqrt{w^2}$, v = 1. Therefore, the second angular translation is:

$$\psi_3 := -\operatorname{atan}\left(\frac{v}{\sqrt{u^2 + w^2}}\right) \qquad (3\text{-}10)$$

$\psi_3 = -11.31^\circ$

Therefore the directions cosines will be

$$\begin{pmatrix} \alpha_1 & \beta_1 & \gamma_1 \\ \alpha_2 & \beta_2 & \gamma_2 \\ \alpha_3 & \beta_3 & \gamma_3 \end{pmatrix} := \begin{pmatrix} 1 & 0 & 0 \\ 0 & \cos(\psi_3) & \sin(\psi_3) \\ 0 & -\sin(\psi_3) & \cos(\psi_3) \end{pmatrix} \cdot \begin{pmatrix} \cos(\psi_2) & 0 & -\sin(\psi_2) \\ 0 & 1 & 0 \\ \sin(\psi_2) & 0 & \cos(\psi_2) \end{pmatrix} \cdot \begin{pmatrix} \cos(\psi_1) & \sin(\psi_1) & 0 \\ -\sin(\psi_1) & \cos(\psi_1) & 0 \\ 0 & 0 & 1 \end{pmatrix} \quad (3\text{-}11)$$

$$\begin{pmatrix} \alpha_1 & \beta_1 & \gamma_1 \\ \alpha_2 & \beta_2 & \gamma_2 \\ \alpha_3 & \beta_3 & \gamma_3 \end{pmatrix} = \begin{pmatrix} 0.8 & 0 & -0.6 \\ -0.118 & 0.981 & -0.157 \\ 0.588 & 0.196 & 0.784 \end{pmatrix}$$

A proper orthogonal transformation can be confirmed from Appendix.

Transformation of Stress and Strain Tensors

After finding the direction cosines between the material and specimen coordinate systems transformation of stress and strain tensors between the material and specimen coordinate systems can be done by applying the proper load conditions. Later on resolved shear stresses and strains can be found from these transformed matrices on the crystallographic planes. Following Lekhnitskii (1963) the stress transformation is:

$$\{\sigma'\} = [\mathbf{Q}'_\sigma]\ \{\sigma\} \quad (3\text{-}12)$$

$$\{\sigma\} = [\mathbf{Q}'_\sigma]^{-1}\{\sigma'\} = [\mathbf{Q}_\sigma]\ \{\sigma'\} \quad (3\text{-}13)$$

Here $[\mathbf{Q_\sigma}]$ is the stress transformation matrix

$$[Q_\sigma] := \begin{bmatrix} \alpha_1^2 & \alpha_2^2 & \alpha_3^2 & 2\cdot\alpha_3\cdot\alpha_2 & 2\cdot\alpha_1\cdot\alpha_3 & 2\cdot\alpha_2\cdot\alpha_1 \\ \beta_1^2 & \beta_2^2 & \beta_3^2 & 2\cdot\beta_3\cdot\beta_2 & 2\cdot\beta_1\cdot\beta_3 & 2\cdot\beta_2\cdot\beta_1 \\ \gamma_1^2 & \gamma_2^2 & \gamma_3^2 & 2\cdot\gamma_3\cdot\gamma_2 & 2\cdot\gamma_1\cdot\gamma_3 & 2\cdot\gamma_2\cdot\gamma_1 \\ \beta_1\cdot\gamma_1 & \beta_2\cdot\gamma_2 & \beta_3\cdot\gamma_3 & (\beta_2\cdot\gamma_3+\beta_3\cdot\gamma_2) & (\beta_1\cdot\gamma_3+\beta_3\cdot\gamma_1) & (\beta_1\cdot\gamma_2+\beta_2\cdot\gamma_1) \\ \gamma_1\cdot\alpha_1 & \gamma_2\cdot\alpha_2 & \gamma_3\cdot\alpha_3 & (\gamma_2\cdot\alpha_3+\gamma_3\cdot\alpha_2) & (\gamma_1\cdot\alpha_3+\gamma_3\cdot\alpha_1) & (\gamma_1\cdot\alpha_2+\gamma_2\cdot\alpha_1) \\ \alpha_1\cdot\beta_1 & \alpha_2\cdot\beta_2 & \alpha_3\cdot\beta_3 & (\alpha_2\cdot\beta_3+\alpha_3\cdot\beta_2) & (\alpha_1\cdot\beta_3+\alpha_3\cdot\beta_1) & (\alpha_1\cdot\beta_2+\alpha_2\cdot\beta_1) \end{bmatrix}$$

The state of stress is defined in terms of the specimen $\{\sigma\}$ or material $\{\sigma'\}$ stresses by:

$$\{\sigma\} = \begin{pmatrix} \sigma_x \\ \sigma_y \\ \sigma_z \\ \tau_{yz} \\ \tau_{zx} \\ \tau_{xy} \end{pmatrix} \qquad \{\sigma'\} = \begin{pmatrix} \sigma'_x \\ \sigma'_y \\ \sigma'_z \\ \tau'_{yz} \\ \tau'_{zx} \\ \tau'_{xy} \end{pmatrix} \qquad (3\text{-}15)$$

The strain transformation is carried out by following the same approach:

$$\{\varepsilon'\} = [\mathbf{Q}'_\varepsilon]\ \{\varepsilon\} \qquad (3\text{-}16)$$

$$\{\varepsilon\} = [\mathbf{Q}'_\varepsilon]^{-1}\{\varepsilon'\} = [\mathbf{Q}_\varepsilon]\ \{\varepsilon'\} \qquad (3\text{-}17)$$

Here $[\mathbf{Q}_\varepsilon]$ is the strain transformation matrix

$$[Q_\varepsilon] = \begin{bmatrix} \alpha_1^2 & \alpha_2^2 & \alpha_3^2 & \alpha_3\cdot\alpha_2 & \alpha_1\cdot\alpha_3 & \alpha_2\cdot\alpha_1 \\ \beta_1^2 & \beta_2^2 & \beta_3^2 & \beta_3\cdot\beta_2 & \beta_1\cdot\beta_3 & \beta_2\cdot\beta_1 \\ \gamma_1^2 & \gamma_2^2 & \gamma_3^2 & \gamma_3\cdot\gamma_2 & \gamma_1\cdot\gamma_3 & \gamma_2\cdot\gamma_1 \\ 2\beta_1\cdot\gamma_1 & 2\beta_2\cdot\gamma_2 & 2\beta_3\cdot\gamma_3 & (\beta_2\cdot\gamma_3+\beta_3\cdot\gamma_2) & (\beta_1\cdot\gamma_3+\beta_3\cdot\gamma_1) & (\beta_1\cdot\gamma_2+\beta_2\cdot\gamma_1) \\ 2\gamma_1\cdot\alpha_1 & 2\gamma_2\cdot\alpha_2 & 2\gamma_3\cdot\alpha_3 & (\gamma_2\cdot\alpha_3+\gamma_3\cdot\alpha_2) & (\gamma_1\cdot\alpha_3+\gamma_3\cdot\alpha_1) & (\gamma_1\cdot\alpha_2+\gamma_2\cdot\alpha_1) \\ 2\alpha_1\cdot\beta_1 & 2\alpha_2\cdot\beta_2 & 2\alpha_3\cdot\beta_3 & (\alpha_2\cdot\beta_3+\alpha_3\cdot\beta_2) & (\alpha_1\cdot\beta_3+\alpha_3\cdot\beta_1) & (\alpha_1\cdot\beta_2+\alpha_2\cdot\beta_1) \end{bmatrix} \quad (3\text{-}18)$$

Isotropic material's stress and strain for a uniaxial state of stress According to Hooke's law is given by:

$$\sigma = E\cdot\varepsilon \quad (3\text{-}19)$$

According to Hooke's law, stress and strain relationship for a homogeneous anisotropic body is given by:

$$\{\sigma\} = [\mathbf{A}_{ij}]\ \{\varepsilon\} \quad (3\text{-}20)$$

$$[\mathbf{A}_{ij}] = [a_{ij}]^{-1} \quad (3\text{-}21)$$

Where constant a_{ij} is the coefficient of deformation and constant A_{ij} is the moduli of elasticity, which are the function of orientation and $[\mathbf{a}_{ij}]$ is a symmetric matrix such that:

$$[\mathbf{a}_{ij}] = [\mathbf{a}_{ji}]. \quad (3\text{-}22)$$

Therefore

$$\{\varepsilon\} = [\mathbf{a}_{ij}]\ \{\sigma\} \quad (3\text{-}23)$$

And

$$\{\varepsilon'\} = [\mathbf{a'}_{ij}]\ \{\sigma'\} \quad (3\text{-}24)$$

$$\text{where} \quad [\mathbf{a}_{ij}] = \begin{pmatrix} a_{12} & a_{22} & a_{23} & a_{24} & a_{25} & a_{26} \\ a_{13} & a_{23} & a_{33} & a_{34} & a_{35} & a_{36} \\ a_{14} & a_{24} & a_{34} & a_{44} & a_{45} & a_{46} \\ a_{15} & a_{25} & a_{35} & a_{45} & a_{55} & a_{56} \\ a_{16} & a_{26} & a_{36} & a_{46} & a_{55} & a_{66} \end{pmatrix} \quad (3\text{-}25)$$

The elastic properties of FCC crystals exhibit cubic symmetry, also described as cubic syngony. The majority of pure metals-iron, copper, nickel, silver, gold, and others form crystals of cubic syngony. Materials with cubic syngony have only three independent elastic constants designated as the elastic modulus, shear modulus, and poisson ratio.

Here the elastic constants are defined as:

$$a_{11} = \frac{1}{E_{xx}} \qquad a_{44} = \frac{1}{G_{yz}} \qquad a_{12} = -\frac{\nu_{yx}}{E_{xx}} = -\frac{\nu_{xy}}{E_{yy}}$$

$$\text{Therefore} \quad [a_{ij}] = \begin{pmatrix} a_{11} & a_{12} & a_{12} & 0 & 0 & 0 \\ a_{12} & a_{11} & a_{12} & 0 & 0 & 0 \\ a_{12} & a_{12} & a_{11} & 0 & 0 & 0 \\ 0 & 0 & 0 & a_{44} & 0 & 0 \\ 0 & 0 & 0 & 0 & a_{44} & 0 \\ 0 & 0 & 0 & 0 & 0 & a_{44} \end{pmatrix} \quad (3\text{-}26)$$

$$[\mathbf{a'}_{ij}] = [Q]^T[\mathbf{a}_{ij}][Q] \qquad (3\text{-}27)$$

By using the component stresses in the specimen coordinate system, the above equations can be applied for working out the component stresses in the material coordinate system.

Calculation of Shear Stresses and Strains on Crystallographic Slip Systems.

Now we have all the component stresses, but since they don't give the clear picture about the individual slip systems, we have to calculate RSS on 12 primary slip systems. Here both the slip plane and slip direction define the primary slip systems. Below outlined are the calculation procedure inspired from Stouffer and Dame.

$$\{\tau\} = c[S]\{\sigma\} \tag{3-28}$$

Where

$$c_i = \frac{1}{\sqrt{h'^2_i + k'^2_i + l'^2_i}\cdot\sqrt{u'^2_i + v'^2_i + w'^2_i}} \tag{3-29}$$

$$S_i = \begin{pmatrix} h'_i\cdot u'_i & k'_i\cdot v'_i & l'_i\cdot w'_i & -w'_i & -v'_i & -u'_i \end{pmatrix} \tag{3-30}$$

Here, [u' v' w'] is the slip direction and (h' k' l') is the slip plane (Recall Figure 2-1). Constant *c* is constant for all the 12 primary systems.

Combining all the result in one matrix we have:

$$\begin{pmatrix} \tau_1 \\ \tau_2 \\ \tau_3 \\ \tau_4 \\ \tau_5 \\ \tau_6 \\ \tau_7 \\ \tau_8 \\ \tau_9 \\ \tau_{10} \\ \tau_{11} \\ \tau_{12} \end{pmatrix} = c\cdot \begin{pmatrix} h'_1\cdot u'_1 & k'_1\cdot v'_1 & l'_1\cdot w'_1 & -w'_1 & -v'_1 & -u'_1 \\ h'_2\cdot u'_2 & k'_2\cdot v'_2 & l'_2\cdot w'_2 & -w'_2 & -v'_2 & -u'_2 \\ h'_3\cdot u'_3 & k'_3\cdot v'_3 & l'_3\cdot w'_3 & -w'_3 & -v'_3 & -u'_3 \\ h'_4\cdot u'_4 & k'_4\cdot v'_4 & l'_4\cdot w'_4 & -w'_4 & -v'_4 & -u'_4 \\ h'_5\cdot u'_5 & k'_5\cdot v'_5 & l'_5\cdot w'_5 & -w'_5 & -v'_5 & -u'_5 \\ h'_6\cdot u'_6 & k'_6\cdot v'_6 & l'_6\cdot w'_6 & -w'_6 & -v'_6 & -u'_6 \\ h'_7\cdot u'_7 & k'_7\cdot v'_7 & l'_7\cdot w'_7 & -w'_7 & -v'_7 & -u'_7 \\ h'_8\cdot u'_8 & k'_8\cdot v'_8 & l'_8\cdot w'_8 & -w'_8 & -v'_8 & -u'_8 \\ h'_9\cdot u'_9 & k'_9\cdot v'_9 & l'_9\cdot w'_9 & -w'_9 & -v'_9 & -u'_9 \\ h'_{10}\cdot u'_{10} & k'_{10}\cdot v'_{10} & l'_{10}\cdot w'_{10} & -w'_{10} & -v'_{10} & -u'_{10} \\ h'_{11}\cdot u'_{11} & k'_{11}\cdot v'_{11} & l'_{11}\cdot w'_{11} & -w'_{11} & -v'_{11} & -u'_{11} \\ h'_{12}\cdot u'_{12} & k'_{12}\cdot v'_{12} & l'_{12}\cdot w'_{12} & -w'_{12} & -v'_{12} & -u'_{12} \end{pmatrix} \cdot \begin{pmatrix} \sigma_x \\ \sigma_y \\ \sigma_z \\ \tau_{xy} \\ \tau_{zx} \\ \tau_{yz} \end{pmatrix} \tag{3-31}$$

Solving Eq. 3-30 for the 12 primary slip systems we have:

$$\begin{pmatrix} \tau_1 \\ \tau_2 \\ \tau_3 \\ \tau_4 \\ \tau_5 \\ \tau_6 \\ \tau_7 \\ \tau_8 \\ \tau_9 \\ \tau_{10} \\ \tau_{11} \\ \tau_{12} \end{pmatrix} = \frac{1}{\sqrt{6}} \cdot \begin{pmatrix} 1 & 0 & -1 & 1 & 0 & -1 \\ 0 & -1 & 1 & -1 & 1 & 0 \\ 1 & -1 & 0 & 0 & 1 & -1 \\ -1 & 0 & 1 & 1 & 0 & -1 \\ -1 & 1 & 0 & 0 & -1 & -1 \\ 0 & 1 & -1 & -1 & -1 & 0 \\ 1 & -1 & 0 & 0 & -1 & -1 \\ 0 & 1 & -1 & -1 & 1 & 0 \\ 1 & 0 & -1 & -1 & 0 & -1 \\ 0 & -1 & 1 & -1 & -1 & 0 \\ -1 & 0 & 1 & -1 & 0 & -1 \\ -1 & 1 & 0 & 0 & 1 & -1 \end{pmatrix} \cdot \begin{pmatrix} \sigma_x \\ \sigma_y \\ \sigma_z \\ \tau_{xy} \\ \tau_{zx} \\ \tau_{yz} \end{pmatrix} \qquad (3\text{-}32)$$

We can calculate shear strains in the same way as the shear stresses described above:

$$\{\gamma\} = c[S]\{\varepsilon\} \qquad (3\text{-}33)$$

After knowing shear stresses and strains on 12 primary octahedral slip systems, we can use them to predict slip within a particular system.

Finite Element Solution

The finite element method is a numerical method for solving problems of engineering and mathematical physics. For problems involving complicated geometries, loadings and materials properties, it is generally not possible to obtain analytical mathematical solutions. Following the study and inspection of various approaches available for modeling, the method most appropriate for a notched single crystal specimen is the FEA (finite element method). It is also the only feasible type of computer

simulation available for this purpose. The micro structural properties, such as dislocation mechanism for instance, play an important role in determining the yield strength of the material specimen. In order to account for the micro structural properties, small –scale atomic simulations may be employed which can predict dislocation generation, interaction etc; however the cost factor for such an approach would be considerably high even for the analysis of very small specimen with actual dimension, on the atomic level. Another limiting factor of using the atomic simulation method is the distortion of the model to an extent that may lead to invalid prediction.

Thus, FEA is the most appropriate tool for such an analysis as it can predict the influence of the geometry and anisotropy of the specimen on the behavior of its material properties without considering atomic interactions. FEA proves itself in its capability of accounting for gross material properties such as modulus of elasticity and Poisson's ratio; and in addition also the directional counterparts of these properties in the case of anisotropic materials.

The Finite Element Model

The commercial software ANSYS (Finite Element Software Version 5.7) is used to model the specific geometries and orientations of the tensile test specimen. The analysis consists of the modeling of two different samples for prediction of slip activity and sectors around the notch (Figure 3-7), which correlate to collaborative work between the Mechanical And Aerospace Engineering and Materials Science And Engineering Department of University of Florida.

The prediction of the slip deformation is based on numerical model's highest individual resolved shear stresses. There is a definite co-relation between the slip lines observed in the experimental test samples and the slip systems that are represented by the highest resolved shear stresses in the numerical model.

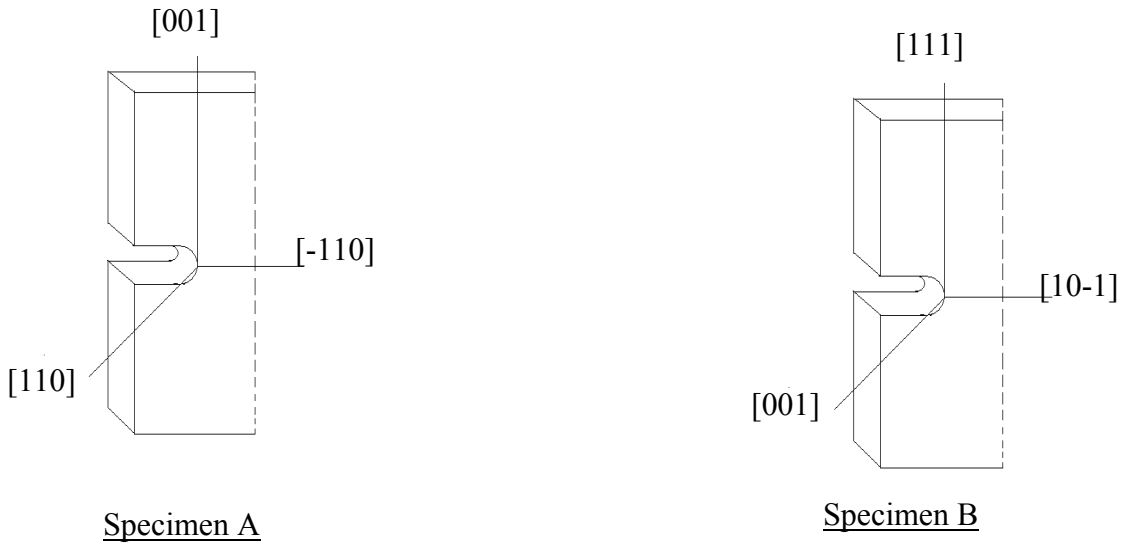

Figure 3-7 Orientations of specimen A and specimen B.

MathCAD 2000 professional was used to make a comparison between the numerically modeled specimen for the given load condition and the analytical solution of an un-notched specimen. Thereafter, in order to make a comparison of the numerical model with the experimental test specimen, a double notch was introduced in the model specimen. The FEA component stresses were taken from the material coordinate system, around the notch, and then used in the transformation equations to calculate the individual resolved shear stresses. The analysis of the data was done, for a complete stress field including a wide range of radial and angular distances. The results of this analysis were subsequently used to make predictions about sectors and slip activity.

Criteria of Testing the Numerical Model

The Finite element model of the entire tensile specimen without any notches was verified using the following two step procedure.

Initial Check

The chapter on analytical method describes the process required to verify the initial finite element model. The complete tensile specimen, without any notches has been analyzed in accordance with this process. Any dimension given for the model would result in a correct solution through the analytical method. For consistency, the same dimensions as those used in the experimental model were used for the numerical method. Provided that the material stays within the elastic range, the stresses will vary linearly with the load. The load of 100 lbs, which is used for all numerical models, results in stresses lower than the yield point. The stresses are scaled proportionally for other loads. The initial check gave the following results, which are tabulated below. (Table 3-2).

Table 3-2 Comparison of analytical and numerical component stresses for specimen A. (Material co-ordinate system)

σ (psi)	σ_x	σ_y	σ_z	σ_{xy}	σ_{yz}	σ_{xz}
Analytical	0	0	7027.9	0	0	0
Numerical	3.6642	3.6643	7028.4	-3.7176	4.86E-03	-2.49E-02
% Error			0.007%			

The component stresses are in excellent agreement according to the preliminary check. The percentage error is within acceptable limits, confirming the accuracy of the co-ordinate and stress transformation of the model.

Final Check

After the initial check, the model was tested for the strain components because that would provide a better test of a correct anisotropic model. Such testing incorporates

the use of the transformed stress tensor matrix. The component strain is tabulated below. The negligible amount or error shown below, confirms the correctness of the model.

Table 3-3 Comparison of analytical and numerical component strains for specimen A. (Material co-ordinate system)

ε	ε_x	ε_y	ε_z	ε_{xy}	ε_{yz}	ε_{xz}
Analytical	-1.83E-04	-1.83E-04	4.56E-04	0	0	0
Numerical	-1.83E-04	-1.83E-04	4.56E-04	-2.37E-07	3.09E-10	-1.59E-09
% Error	0.016%	0.016%	0.044%			

The above two-step testing procedure was repeated for each orientation before the introduction of the notch in the specimen. Finally, the notch geometry was incorporated onto the existing model, which completed the actual specimen model.

Model Features and Characteristics

Spatial Characteristics.

The FEM does not take into account the entire geometry of the specimen and is limited to the body of the specimen. The specimen end grips are excluded mainly because the mechanics at the grips differ from those at the specimen center and include other effects such as loading rate and tensile rig contact pressure. The grip is most susceptible to early deformations of different kinds and also to fracture, as seen in the experimental model. Also, most often it is seen that grips are changed/updated in order to gain better and accurate results. The numerical model will therefore not be subject to the type of grip used or any variations that it may cause, keeping in mind that our main focus is to model those specimens, which fail at the central area of the specimen and thereafter analyze those stresses.

Both the numerical models utilize the same geometry (including the notch geometry), to observe the effects of orientations without other defect / size considerations. The geometry of both the models was simplified, based on the

experimental counter part to Specimen, A which are shown below (Figure 3-8). Also Table 3-4 shows the actual specimen geometry of Specimen A.

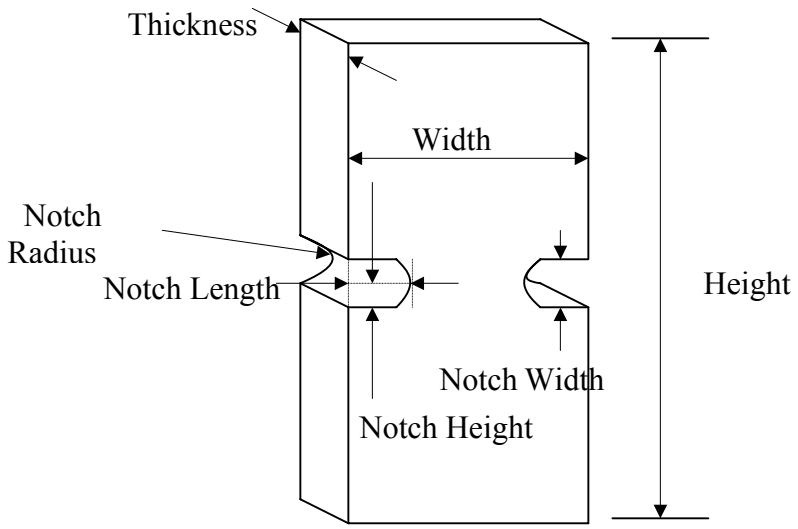

Figure 3-8 Dimensions of the Specimen.

Simplified Geometry of the Notch

The modeled notch consists of a combination of a rectangle and a semicircle. In the experimental model, the notch is likely to have an angular offset within the horizontal, and also some y – displacement offset from the specimen center. In addition, the actual notch tip has an arc smaller than a semicircle. The geometrical; simplifications used for the notch model were 1) Setting both notch lengths and heights equal to those of the largest actual dimension.2) Setting the notch radius equal to the notch height (one half of the notch width) to form a half circle. This simplification provides accurate results in our limited scope of focus on orientation. To study specific test results, these geometrical simplifications may be removed.

Table 3-4 Actual (Specimen A) and finite element specimen geometry.

Specimen Geometry		
(mm)	Actual	FEM
Height	19.000	19.000
Width	5.100	5.100
Thickness	1.800	1.800
Right Notch Length	1.300	1.550
Left Notch Length	1.550	1.550
Right Notch Height	0.113	0.113
Left Notch Height	0.111	0.113
Right Notch Radius	0.045	0.055
Left Notch Radius	0.055	0.055

Material Properties

An accurate model of a single crystal material can be created in ANSYS from our finite element model, which is linear, elastic and orthotropic. The three dimensional elements available in ANSYS can be used to justify orthotropic or anisotropic material properties. These elements in conjunction with the three independent stress tensors (a_{11}, a_{12}, a_{44}) or the three independent directional properties (G, E and ν) can be used to model a single crystal material. The model is created around a global specimen coordinate system in ANSYS (Figure 3-9). The use of proper direction cosines will create the material coordinate system. The stress can now be calculated in any direction as the properties have been defined in the material coordinate system. The directional material properties are duly applicable as in ANSYS the element coordinate system is aligned with the material coordinate system.

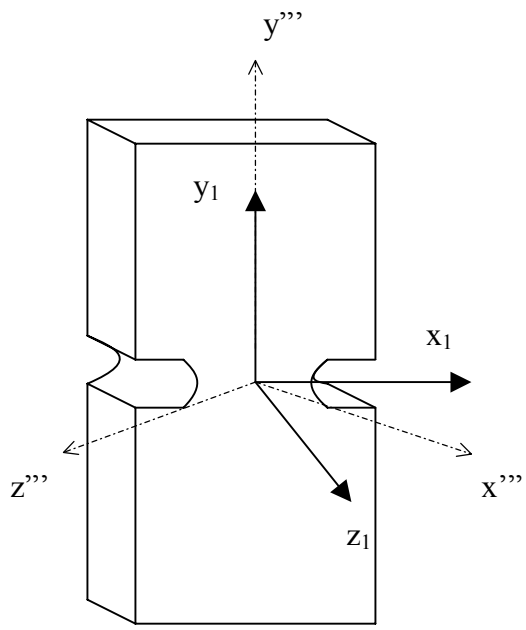

Figure 3-9 Specimen and material coordinate systems. (The specimen is created around the global system (x''', y''', z''') and the material system (x_1, y_1, z_1) is later specified)

Meshing Technique

Initially the three –dimensional solid model is created and the front face is meshed with the PLANE2 elements (ANSYS 5.7 Element Reference, 1999). It is a two-dimensional six node triangular structural solid.

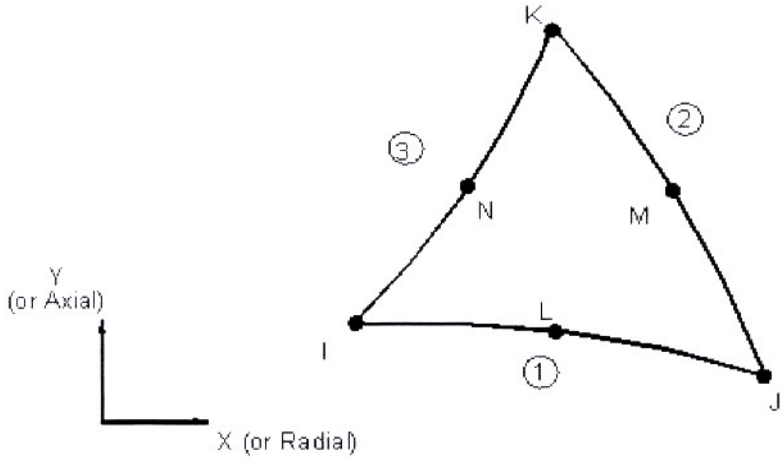

Figure 3-10 PLANE2 2-D 6-NODE triangular structural solid. (ANSYS 5.7 elements reference, 1999).

The element has a quadratic displacement behavior and is well suited to model irregular meshes. This element also has plasticity, creep, large deflection and large strain capabilities. Besides the nodes it also includes orthotropic material properties. However their material properties are not applicable for the modeling purpose it can be deleted later. Front face has precise element sizing along the defined radial lines around the notch tip at a 5° intervals. As soon as the front face is meshed, three –dimensional element, SOLID 95 (Prism option) is swept through the volume of the three-dimensional model to complete meshing of the model. SOLID 95 is a three –dimensional structural solid with 20 nodes. Each node has three degree of freedom with translation in the x, y and z directions. It works in combination with the two dimensional elements (PLANE 2) on the front face, and retain their sizing definitions on each of the x-y planes through the specimen thickness. It has same basic structure as of SOLID 45(Three dimensional element) but it is chosen since it can accurately model the area around the notch because of the presence of the mid size nodes. Also it includes the orthotropic material properties. Among others SOLID 95 also supports plasticity, creep, large deflections and large strains and is well suited for the future development of the model.

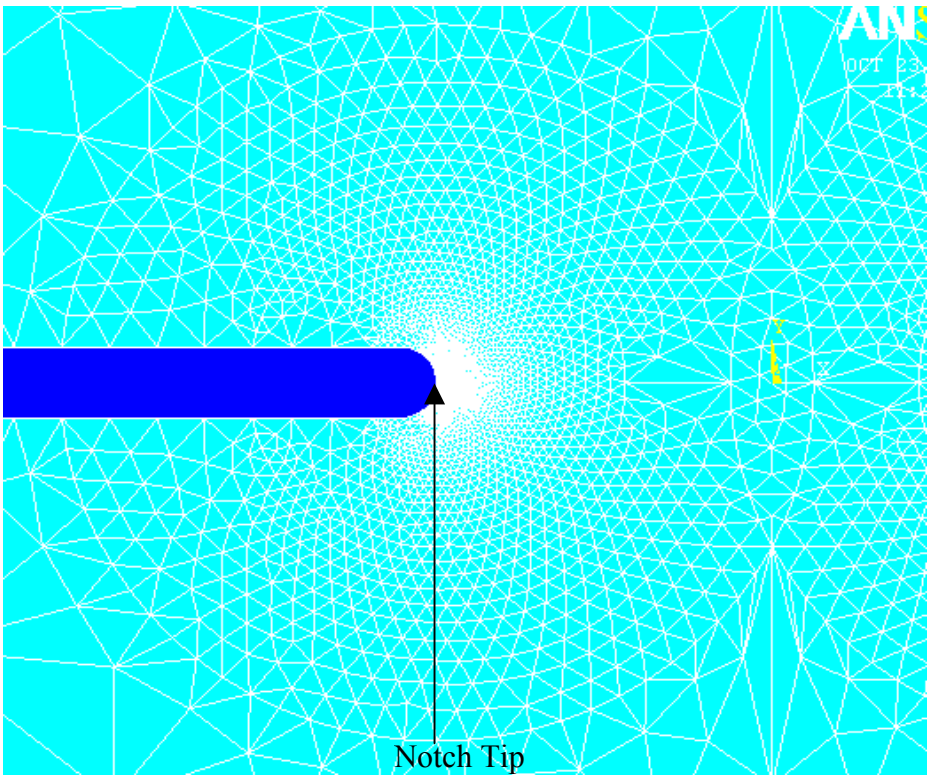

Figure 3-11 Figure showing the meshing near the notch tip in specimen A.

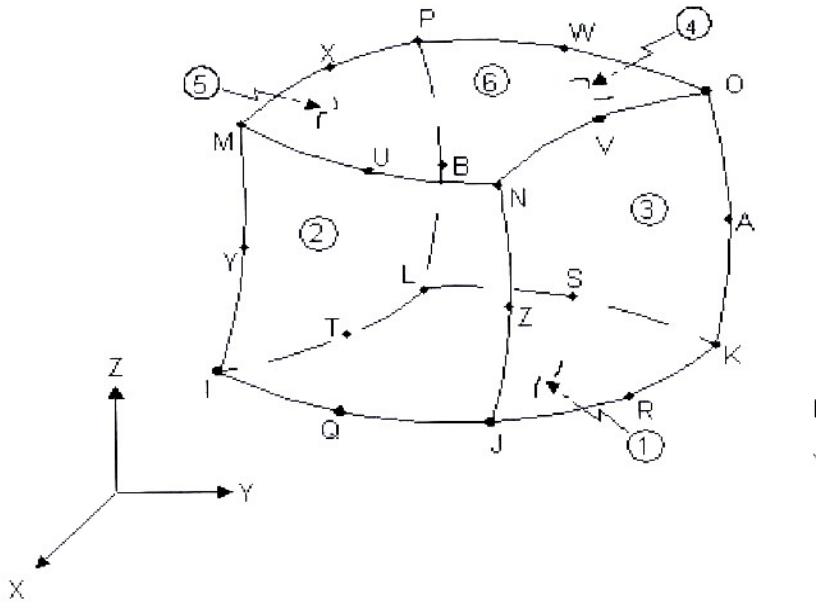

Figure 3-12 SOLID95 3-D 20-node structural solid.(ANSYS 5.7 elements reference, 1999).

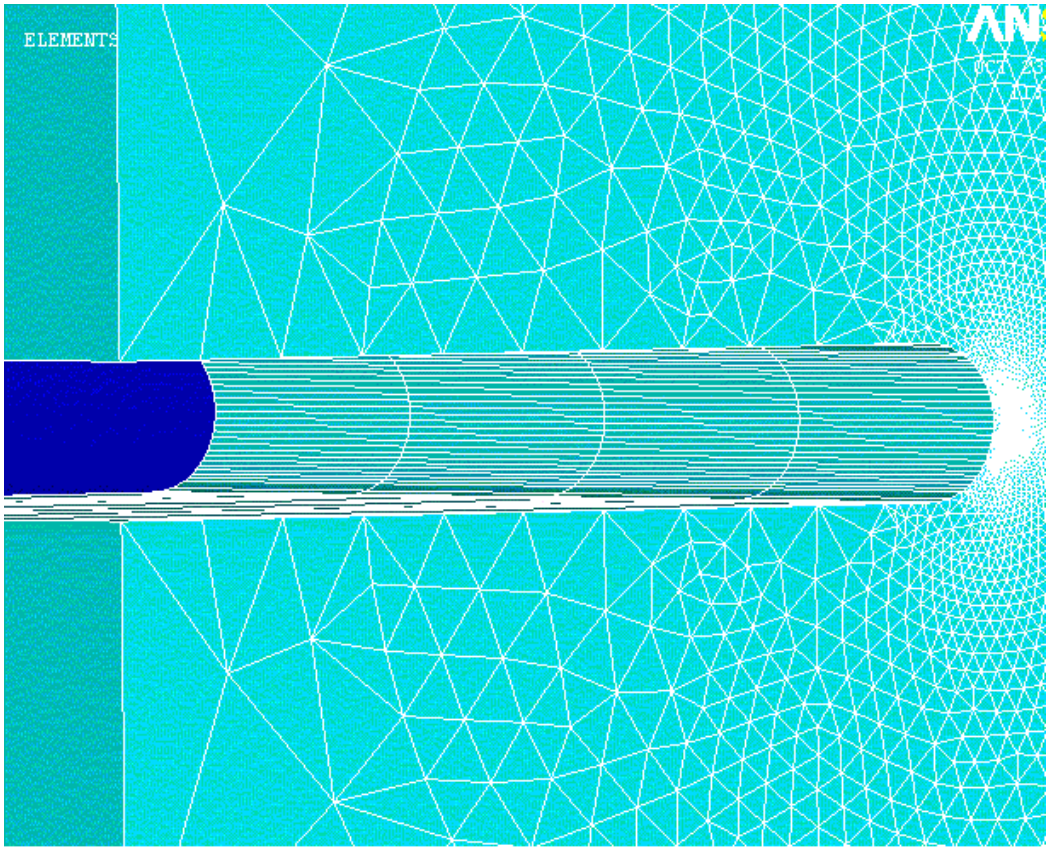

Figure 3-13 Element through the thickness.

Six concentric arcs were created to examine stresses at angular and at radial distances from the notch (to examine near field and far field stresses). The six concentric circles are as follows: 0.25*ρ, 0.50*ρ, 1.00*ρ, 2.00*ρ, 3.00*ρ, and 5.00*ρ; where ρ is the notch radius (Figure 3-14).

Assumption Used in Modeling

Following are the assumptions used for the modeling purpose 1) Low temperature deformation 2) Microstructural behavior are not considered 3) There is no crystal lattice rotation in the model. Finite element analysis is capable of calculating the results for changing temperature. However to simplify the problem, and to collaborate more closely with the MSE department, material properties at a constant room temperature is applied in the numerical model. We also assume that the elastic deformation is taking place and

there is no plasticity near the notch tip. Plasticity can be included in the current model for future research.

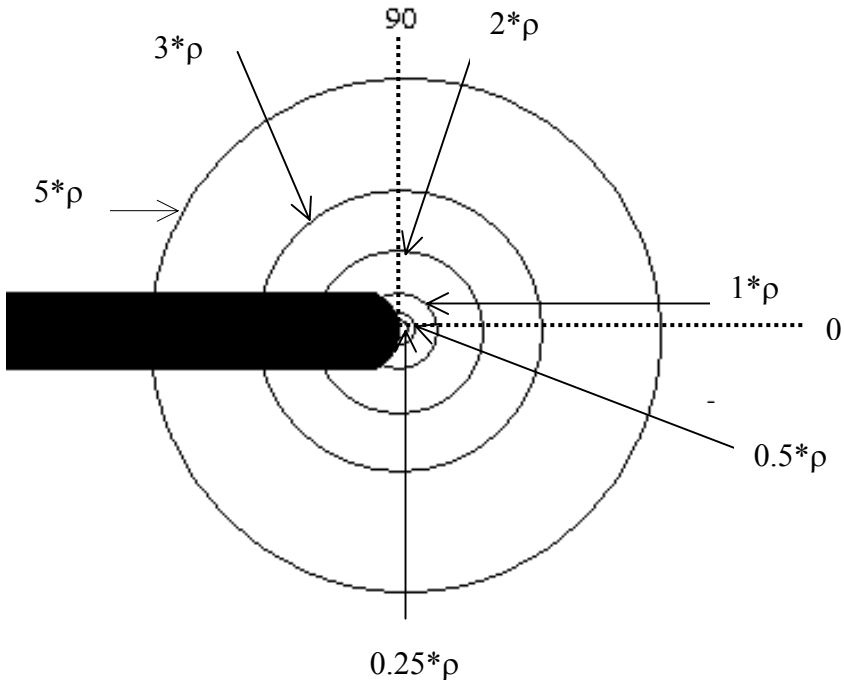

Figure 3-14 Radial arcs around the notch tip.

Experimental Method

The FEA results presented in my thesis will be compared with the results of experimental testing, which have been carried out (Forerro et al, 2002) for the single crystal superalloy. The specimen is tested to observe the effect of load orientation on the "sectors"(the active slip region), about the notch. This experimental approach, based on tensile testing is used to measure various material properties like stress strain behavior and yield strength etc .It employs a double-edged notched tensile specimen as the test sample. The tensile specimen is loaded to observe and study the stress and stain fields, particularly slip line deformation and also the effect of overall displacement of the material. The reason of introducing a notch in the specimen is the production of triaxial

state of stress in its proximity, which provides an environment to study slip systems formation in 3-dimensional stress field. In the experimental approach, unlike the FEA; a compact load is applied to several test specimen with different crystallographic orientations and the response to failure is studied in order to observe the active slip planes. On the contrary, The FEA essentially studies an elastic response where in the magnitude of the applied stress is an indication of which planes will first allow plastic deformation.

The correlation between the most highly- stressed planes in the elastic analysis and the slip lines observed in the experimental approach determines the degree of influence of others dislocation mechanisms on fracture.

CHAPTER 4
RESULTS AND DISCUSSION

This chapter will present results of resolved shear stresses on principal octahedral planes [{111}<110>] and evolution of slip systems in 3-Dimensional anisotropic stress fields. A rectangular single crystal notched specimen in two crystallographic orientations is analyzed and the slip systems predictions are compared with the experimental results. The two specimens are, Specimen A with [001] load orientation and [-110] notch growth direction and Specimen B with [111] load orientation and [10-1] notch growth direction (Figure 3.7). Results on the surface and the mid planes of the specimen are compared and contrasted to examine condition of plane stress and plane strain.

Specimen A

The states of stress and slip systems were analyzed both on the surface and on the mid plane of the specimen in the vicinity of the notch. Only the upper half of the specimen was analyzed (from 0° to 180°) since stress fields and hence the RSS in Specimen A are symmetric about the growth axis [-110].

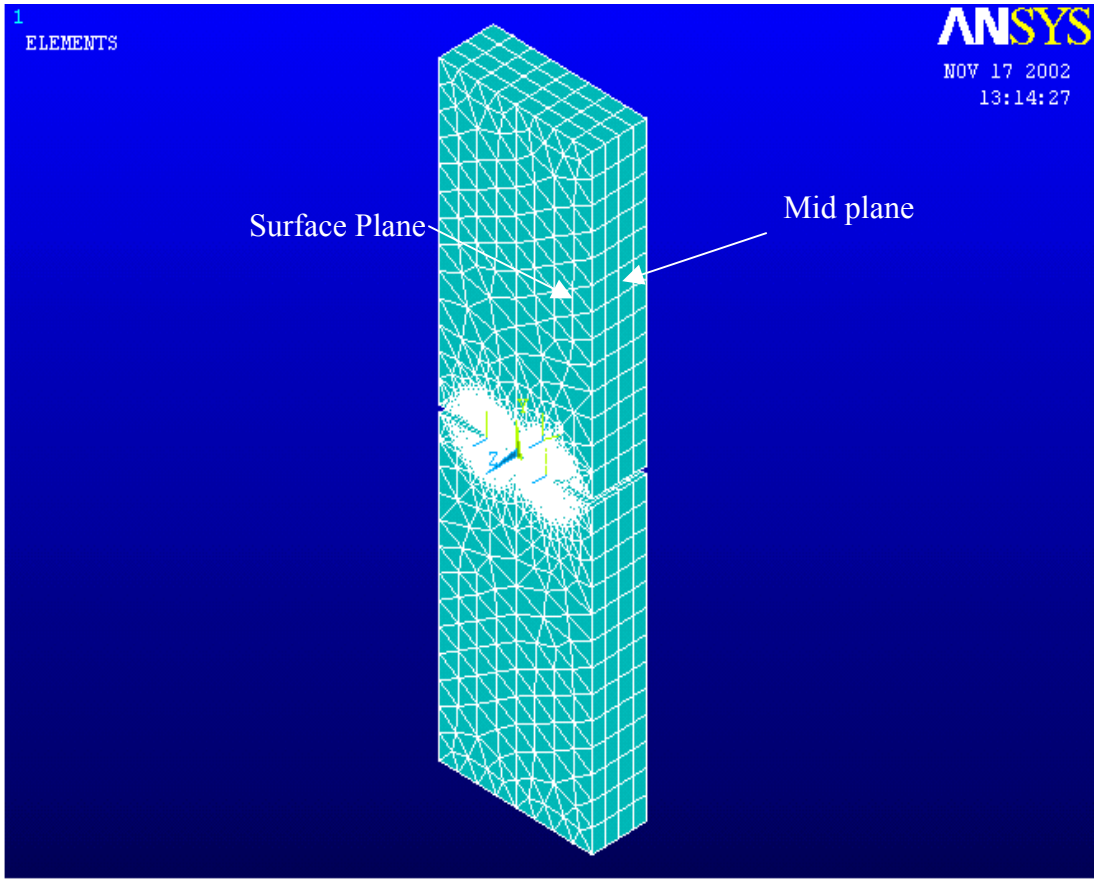

Figure 4-1 Figure showing mid plane and surface plane on which RSS is calculated for specimen A and B.

Surface Results for Specimen A

Twelve primary resolved shear stresses are calculated from 0.25*ρ to 5*ρ (in the radial direction) and from 0˚ to the top of the notch (in angular directions; 100˚ for 0.25*ρ up to 170˚ for 5*ρ) (Figures 4-2 to 4-6). The slip system with the maximum RSS varies with radial and angular position. The maximum RSS near the notch is τ_2 =25,000 psi and occurs at a radius = 0.5*ρ at ± 105˚ angle. The dominant slip system and sectors were determined for each radius, by the overall maximum RSS at that radius (Table 4-1). The stress gradients are very steep in the vicinity of the notch and hence the RSS also vary strongly as a function of the position near the notch.

The effects of variations of theta on RSS can be clearly seen in figures 4-2 to figure 4-6. To observe the effect of theta at a given radius, consider the variation of maximum RSS as a function of radial position. At r = 0.25*ρ, τ_{11}, τ_2 and τ_6 are indicating the dominant slip systems and have maximum RSS from 0° to 17°, 17° to 82° and 82° to 100° respectively.. However, at r = 0.5*ρ, τ_1 and τ_2 are the dominant slip systems from 0° to 35° and from 35° to 105°,respectively, demonstrating that slip system activation is not uniform for all radial distances from a notch. The effect of radius on resolved shear stresses can be seen by plotting the results with the 12 primary stresses for the entire range of radii (Figure 4-9) In order to show stresses on different radii (from 0.25*ρ to 5*ρ), all stresses at each radius have been scaled so they appear in ascending order (with respect to radial distance) from the origin. To observe the effect of radius at a given angle, look at how the RSS changes along θ = 50˚. For example, at r = 0.25*ρ, τ_2 is the maximum RSS; τ_2 remains the maximum RSS at r = 0.5*ρ and then quickly shifts to τ_1 at r = 5*ρ. By analyzing the results we can see the variation in dominant slip systems, though some angles do maintain a single dominant slip systems for all radii (τ_2 at 59°-68°). The RSS field is dominated by τ_1, τ_2, and τ_3 on the (111) plane and by τ_6, τ_9 and τ_{11} on the (-11-1), (-11-1) and (-1-11) planes, respectively.

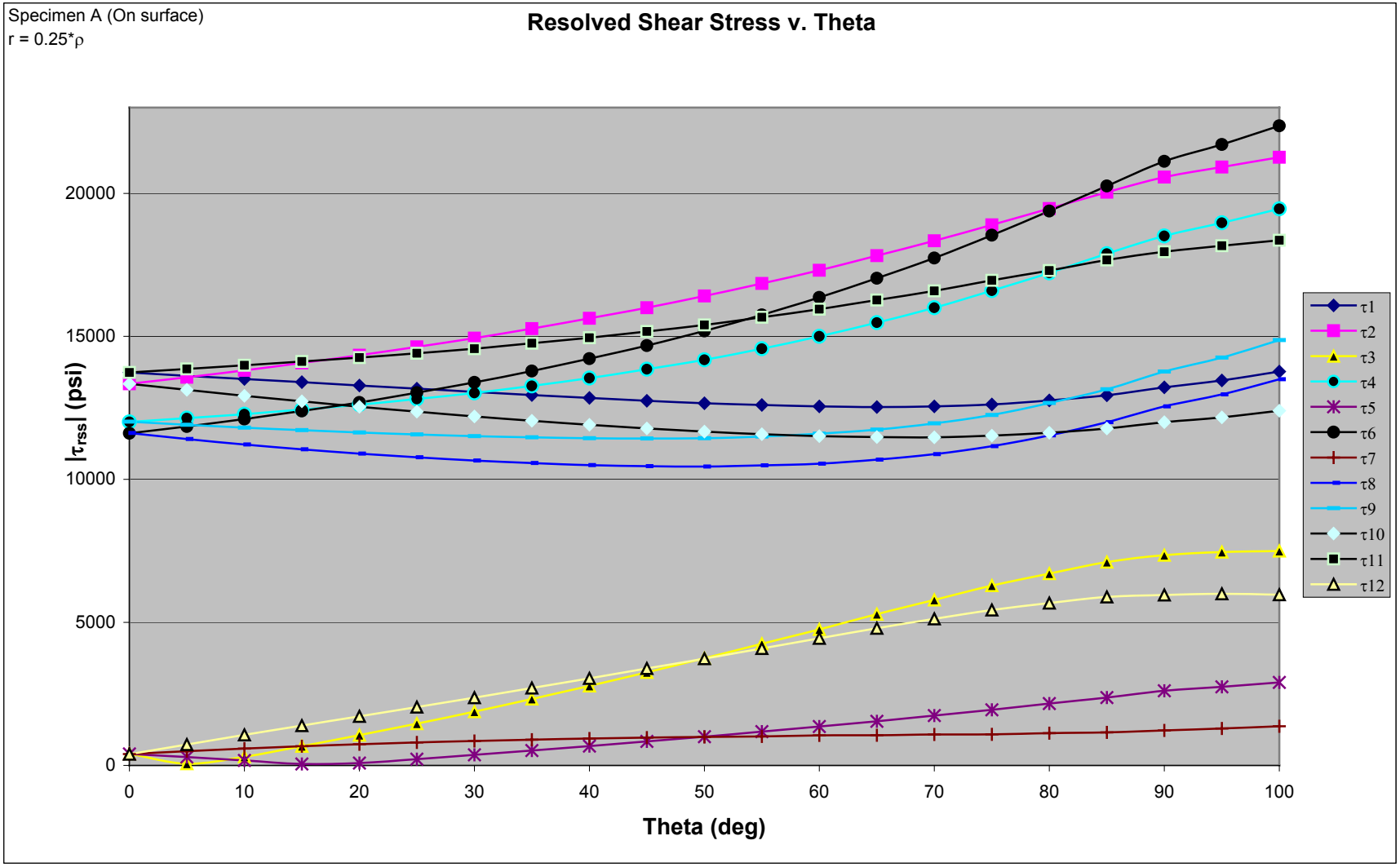

Figure 4-2 Twelve primary resolved shear stresses on the surface of specimen A; r = 0.25*ρ

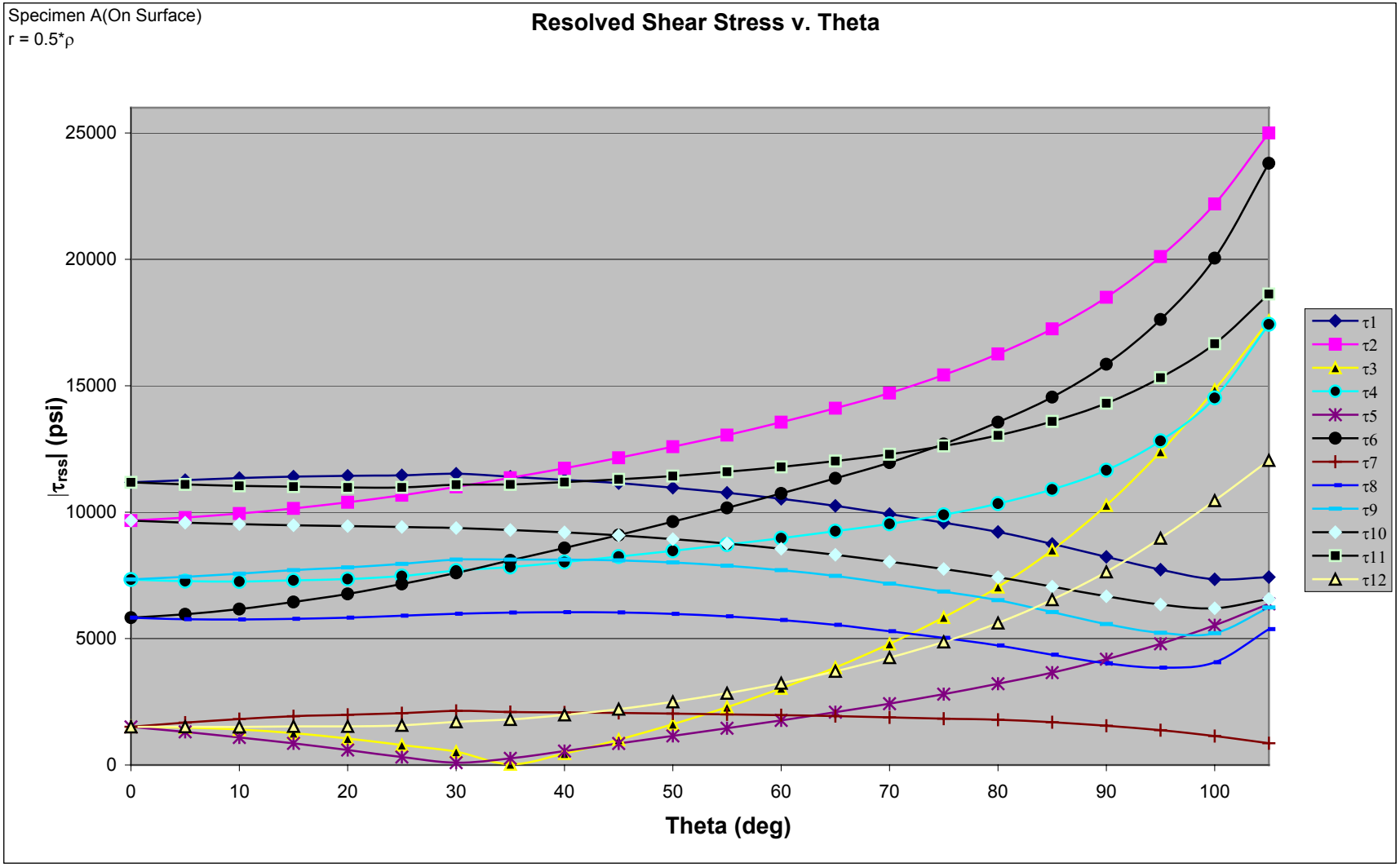

Figure 4-3 Twelve primary resolved shear stresses on the surface of specimen A; r = 0.5*ρ

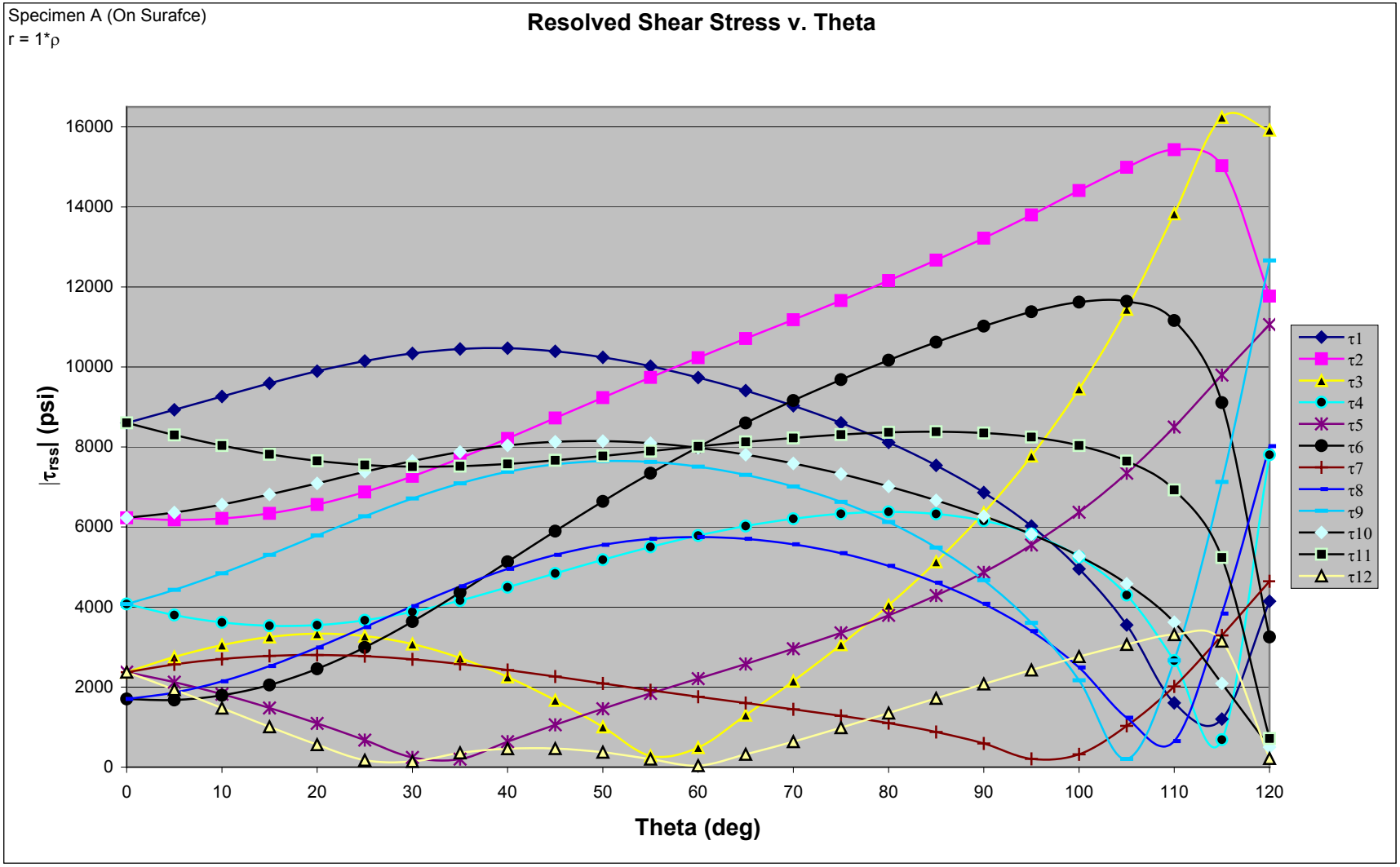

Figure 4-4 Twelve primary resolved shear stresses on the surface of specimen A; r = 1*ρ

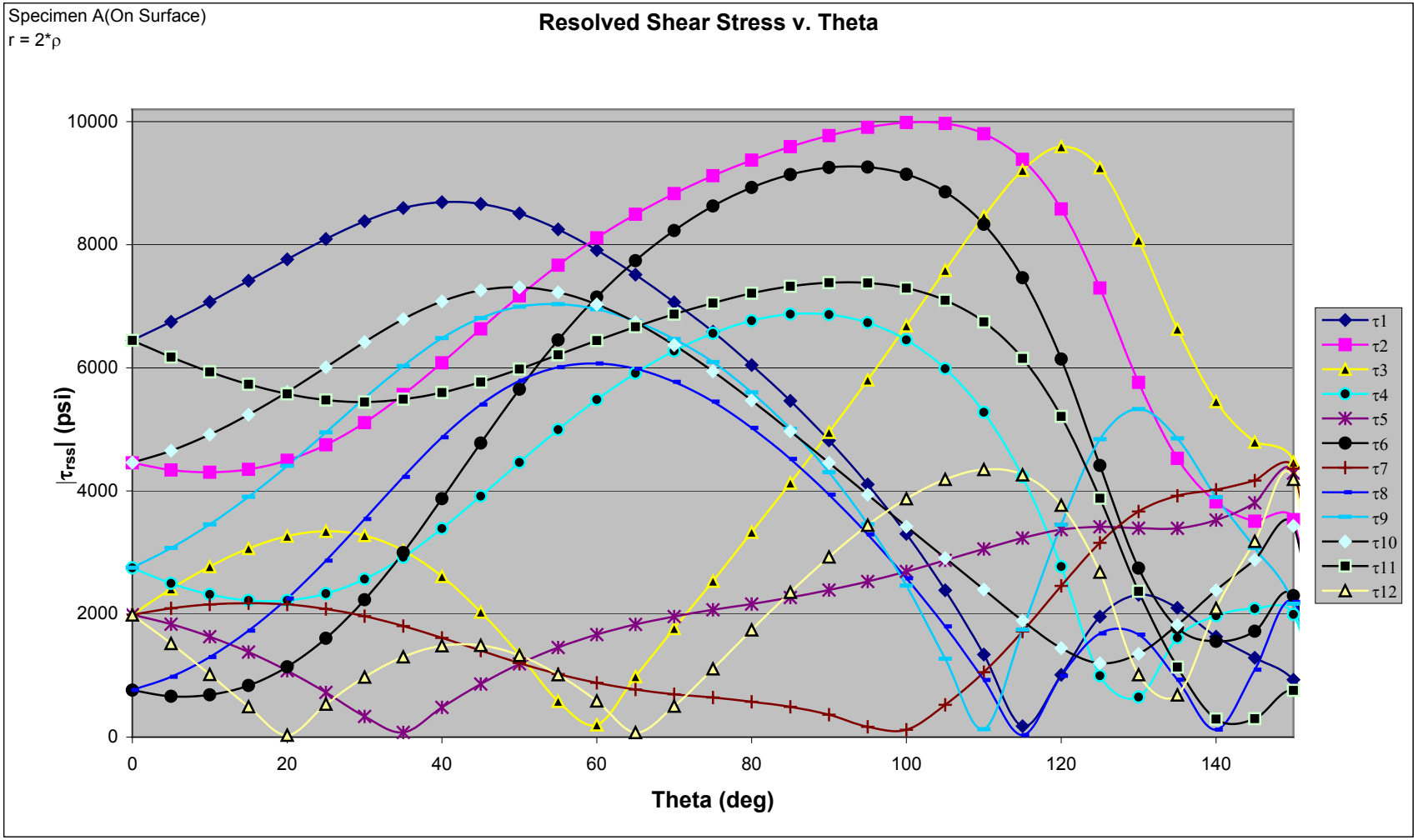

Figure 4-5 Twelve primary resolved shear stresses on the surface of specimen A; r = 2.0*ρ

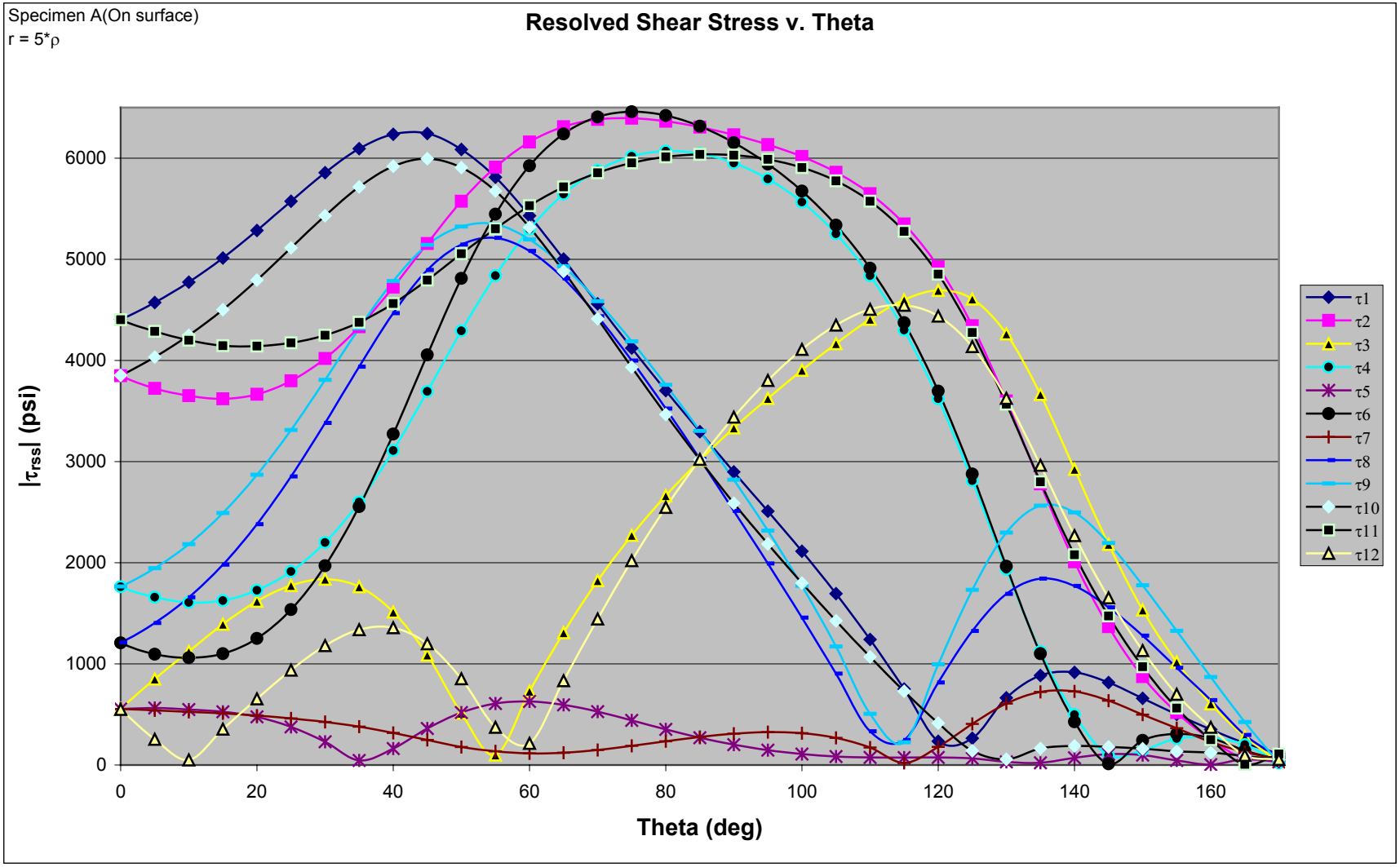

Figure 4-6 Twelve primary resolved shear stresses on the surface of specimen A; r = 5.0*ρ

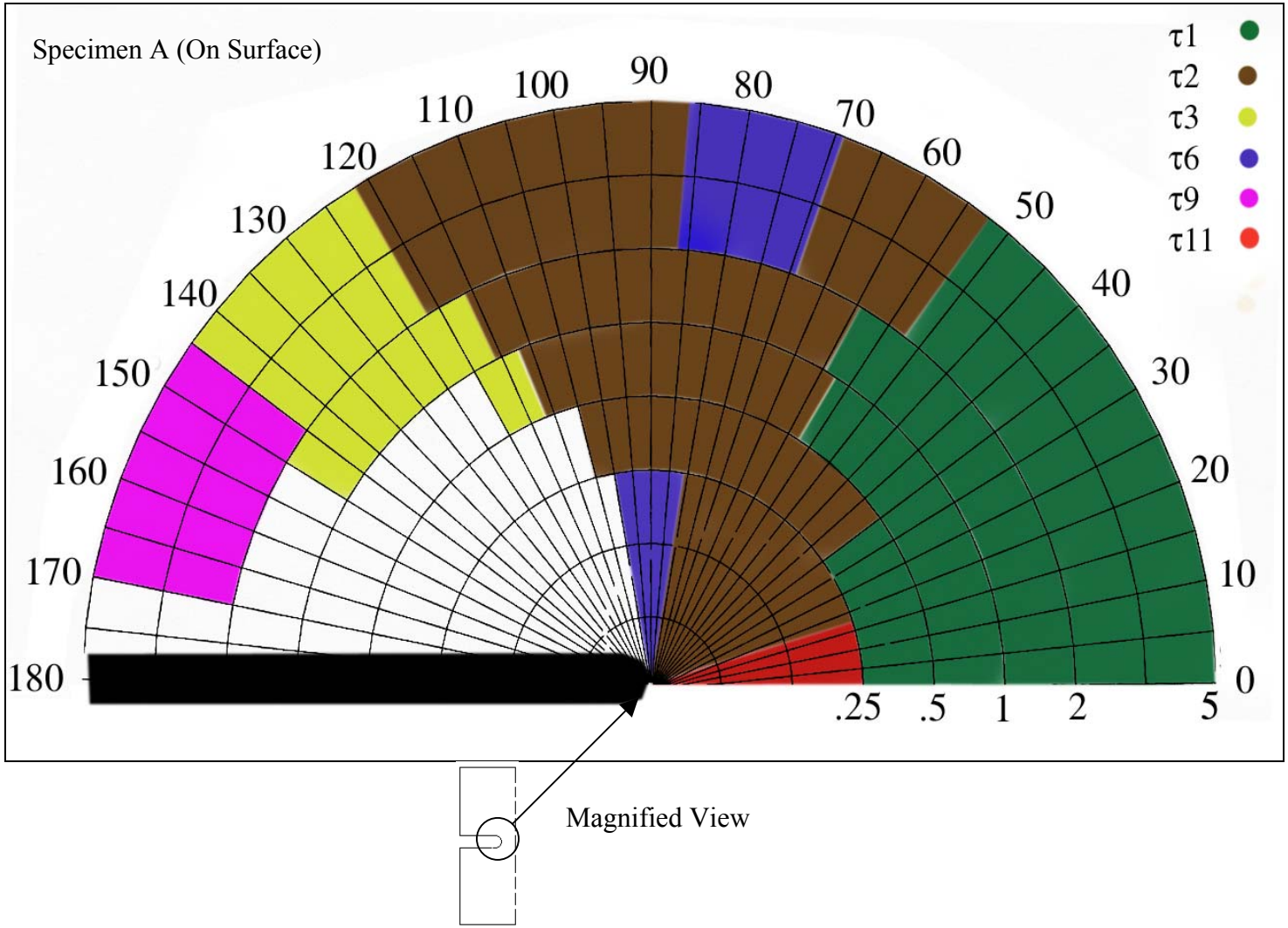

Figure 4-7 Maximum resolved shear stress on each radius occurring on the surface of specimen A. RSS scaled for each radius to plot as one.

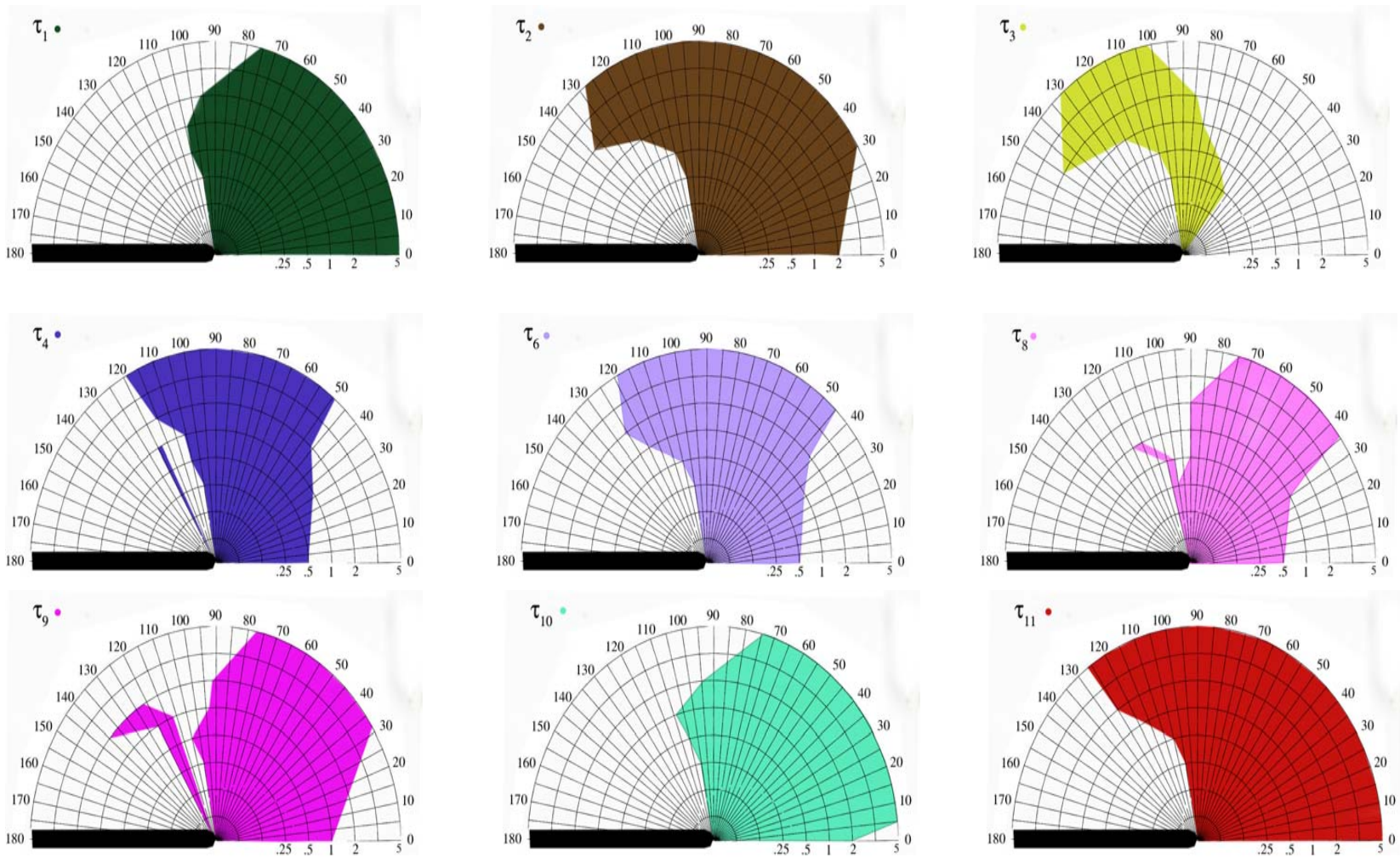

Figure 4-8 Active slip sectors on the surface of specimen A from 0.25*ρ to 5*ρ.

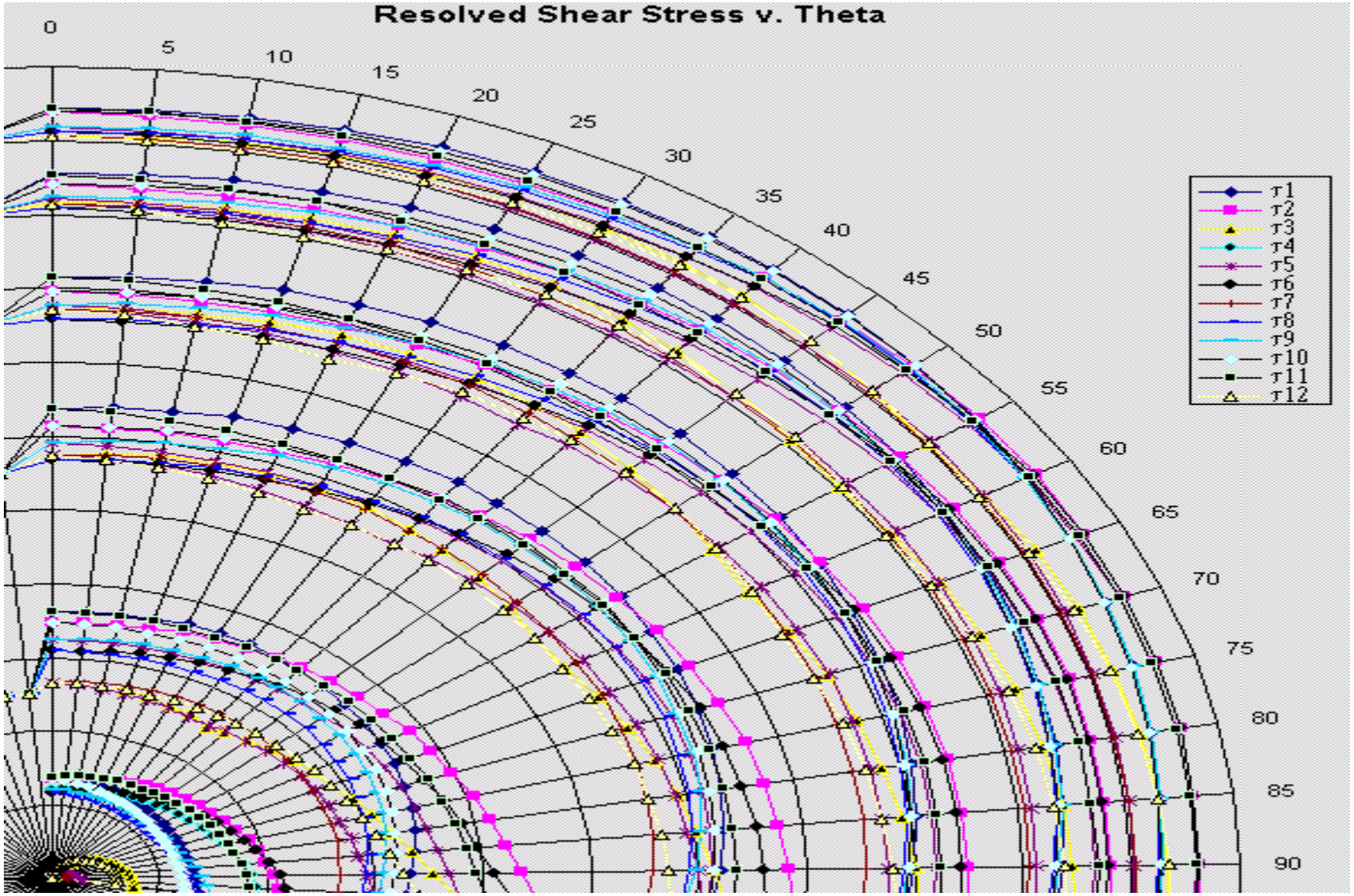
Resolved Shear Stress v. Theta
0
5
10
15
20
25
30
35
40
45
50
55
60
65
70
75
80
85
90
τ1
τ2
τ3
τ4
τ5
τ6
τ7
τ8
τ9
τ10
τ11
τ12

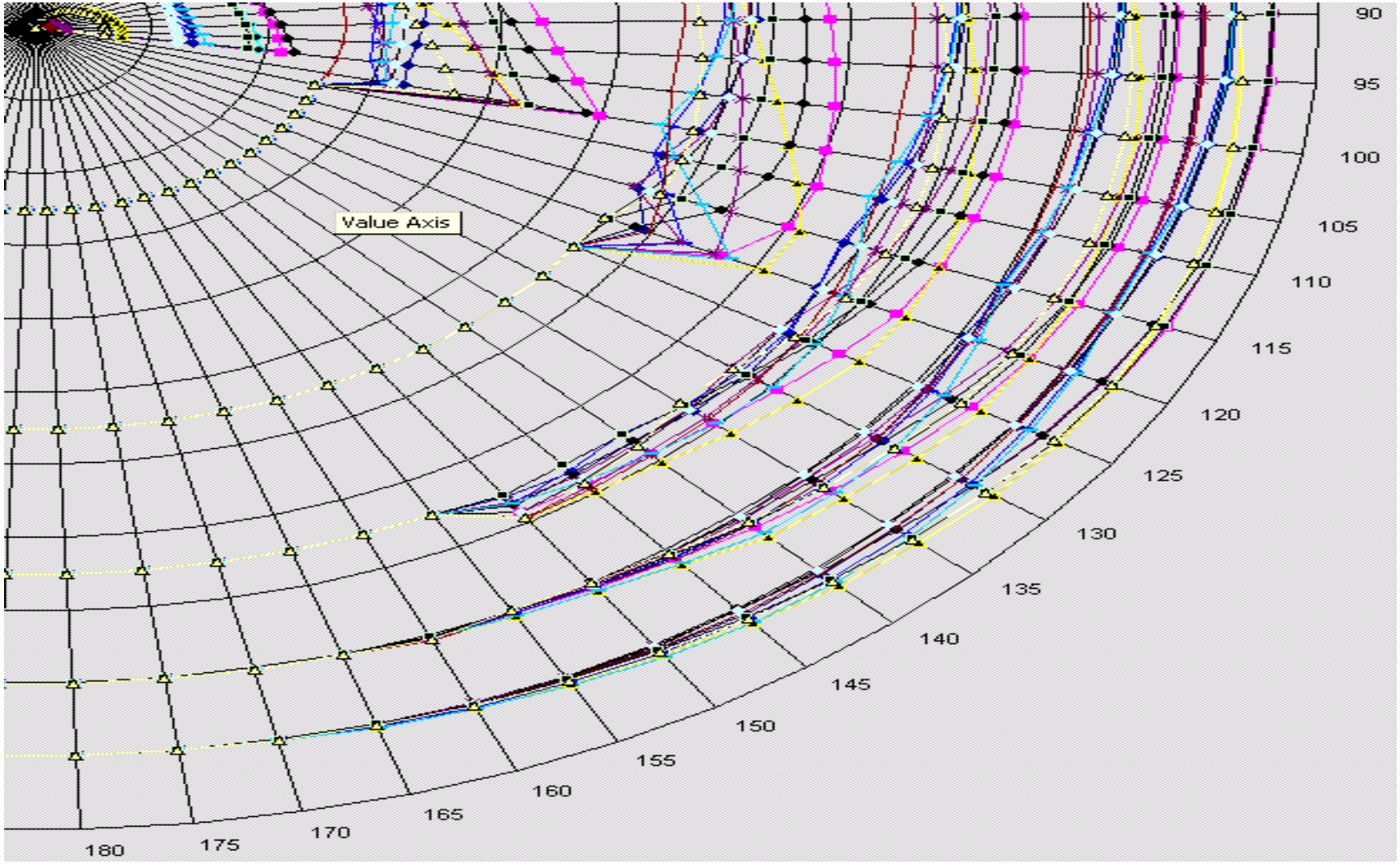

Figure 4-9 Complete RSS field on the surface of Specimen A.

65

Table 4-1 Specimen A dominant slip systems (Surface plane).

Dominant Slip System Sectors Specimen A									
	r = 0.25*ρ			r = 0.5*ρ			r = 1*ρ		
Sector	θ	τ_{max}	Slip System	θ	τ_{max}	Slip System	θ	τ_{max}	Slip System
I	0-17	τ_{11}	(-1-11)[101]	0-35	τ_1	(111)[10-1]	0-57	τ_1	(111)[10-1]
II	17-82	τ_2	(111)[0-11]	35-105	τ_2	(111)[0-11]	57-113	τ_2	(111)[0-11]
III	82-100	τ_6	(-11-1)[011]				113-120	τ_3	(111)[1-10]

	r = 2.0*ρ			r = 5.0*ρ		
Sector	θ	τ_{max}	Slip System	θ	τ_{max}	Slip System
I	0-59	τ_1	(111)[10-1]	0-54	τ_1	(111)[10-1]
II	59-116	τ_2	(111)[0-11]	54-68	τ_2	(111)[0-11]
III	116-150	τ_3	(111)[1-10]	68-86	τ_6	(-11-1)[011]
IV				86-122	τ_2	(111)[0-11]
V				122-145	τ_3	(111)[1-10]
VI				145-165	τ_9	(-11-1)[011]

Mid Plane Results for Specimen A

Twelve primary resolved shear stresses are calculated from 0.25*ρ to 5*ρ and from 0˚ to the top of the notch in order to calculate stresses in angular directions (100˚ for 0.25*ρ up to 170˚ for 5*ρ) (Figures 4-10 to 4-14). The maximum RSS near the notch is τ_4 and τ_6=28,380 psi at a radius = 0.5*ρ at an angle of ± 105˚ angle. The maximum RSS on the mid plane is greater than the maximum RSS on the surface plane. The dominant slip system and sectors were determined for each radius by the overall maximum RSS (Table 4-2).

Results obtained at the mid plane were obtained and analyzed similarly to the results obtained at the surface of specimen A. The number of activated slip systems is higher here as compared to the slip systems on the surface. It shows dominant systems on each of the four possible primary slip planes in the RSS fields. Overall the RSS field is dominated by τ_1, τ_2, and τ_3 on the (111) plane and by τ_4, τ_6, τ_8, τ_9, τ_{10}, τ_{11} and τ_{12} on the {-1-11} family of planes.

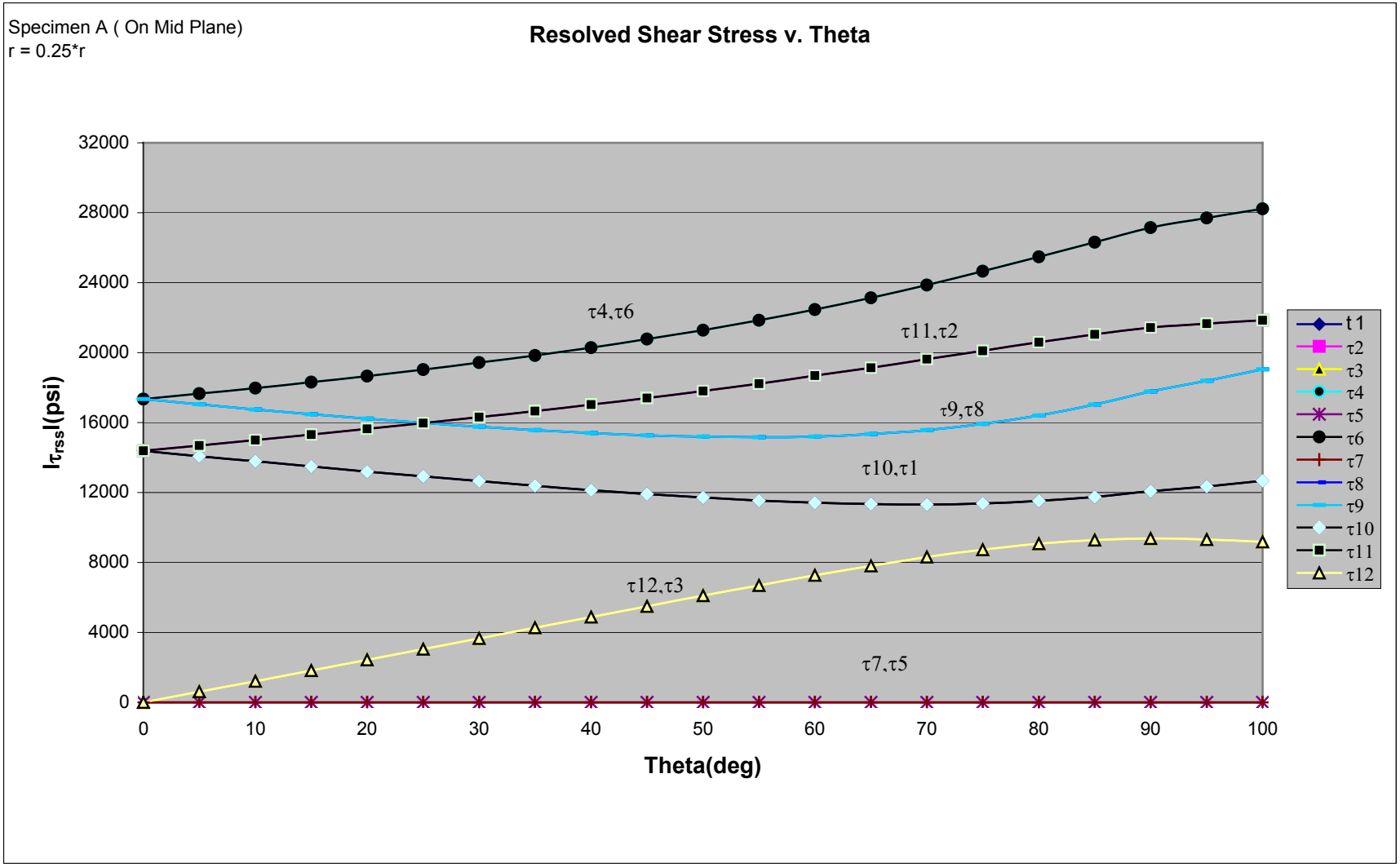

Figure 4-10 Twelve primary resolved shear stresses on the mid plane of specimen A; r = 0.25* ρ

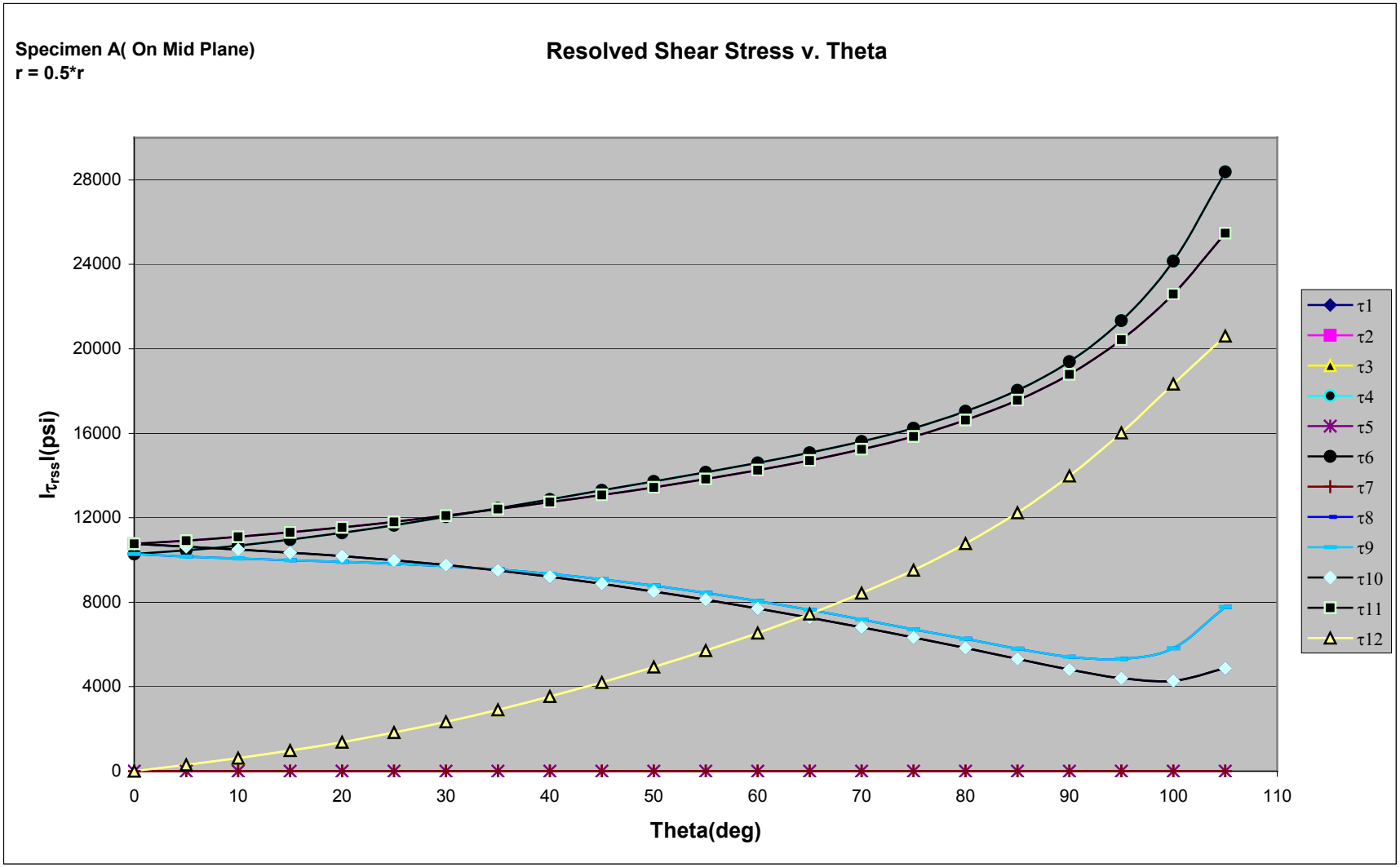

Figure 4-11 Twelve primary resolved shear stresses on the mid plane of Specimen A; r = 0.5* ρ

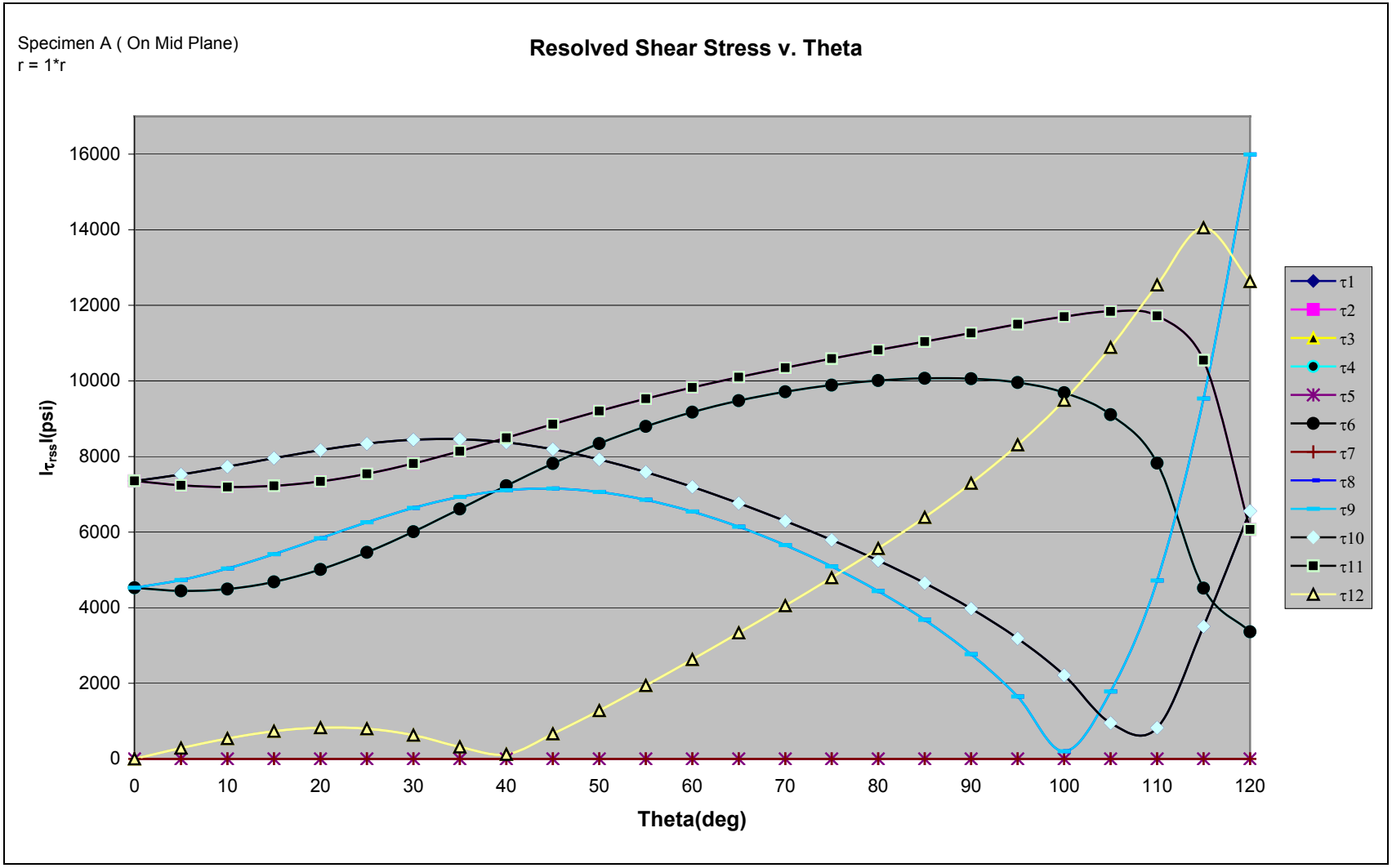

Figure 4-12 Twelve primary resolved shear stresses on the mid plane of specimen A; r = 1.0* ρ

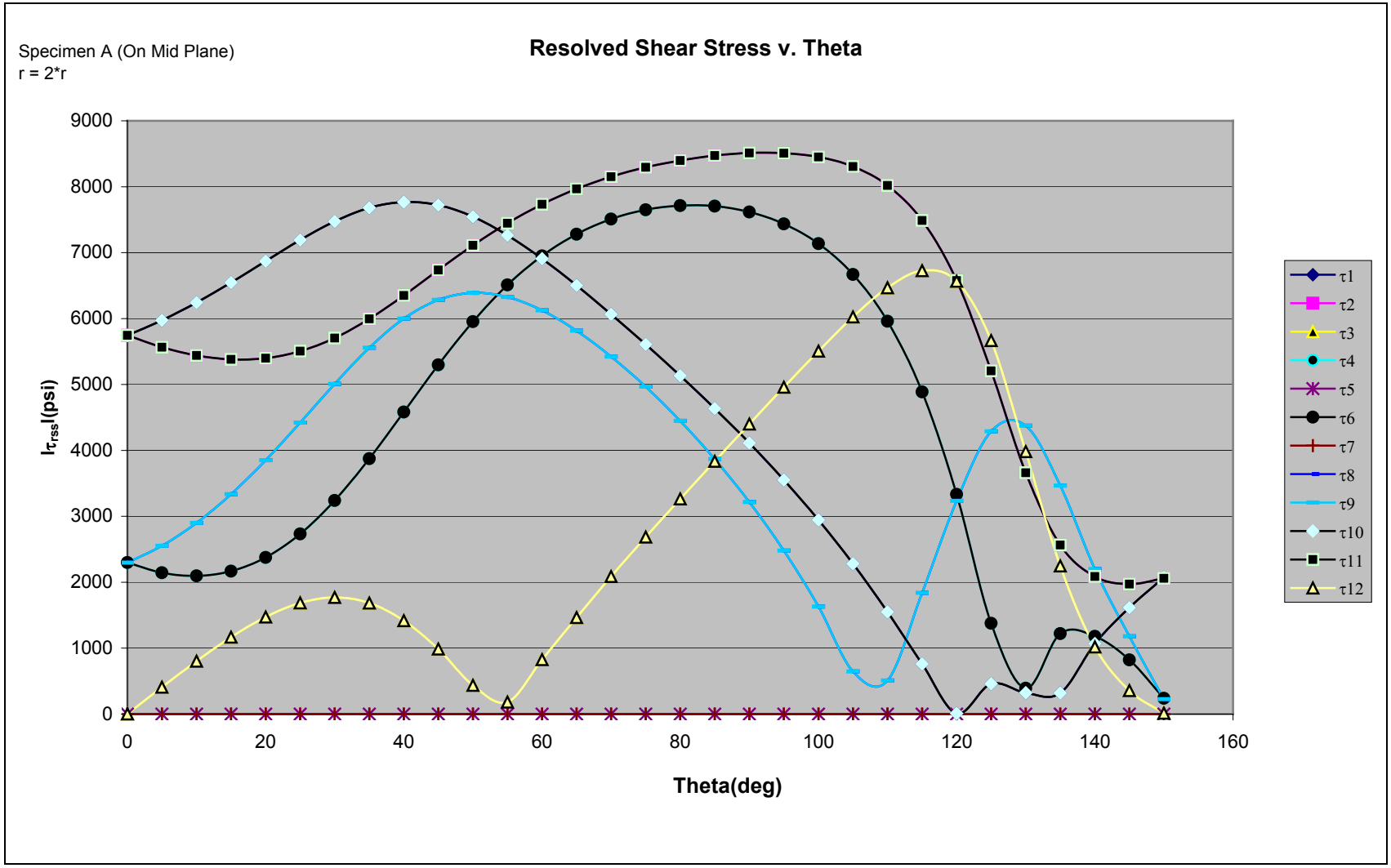

Figure 4-13 Twelve primary resolved shear stresses on the mid plane of specimen A; r = 2.0* ρ

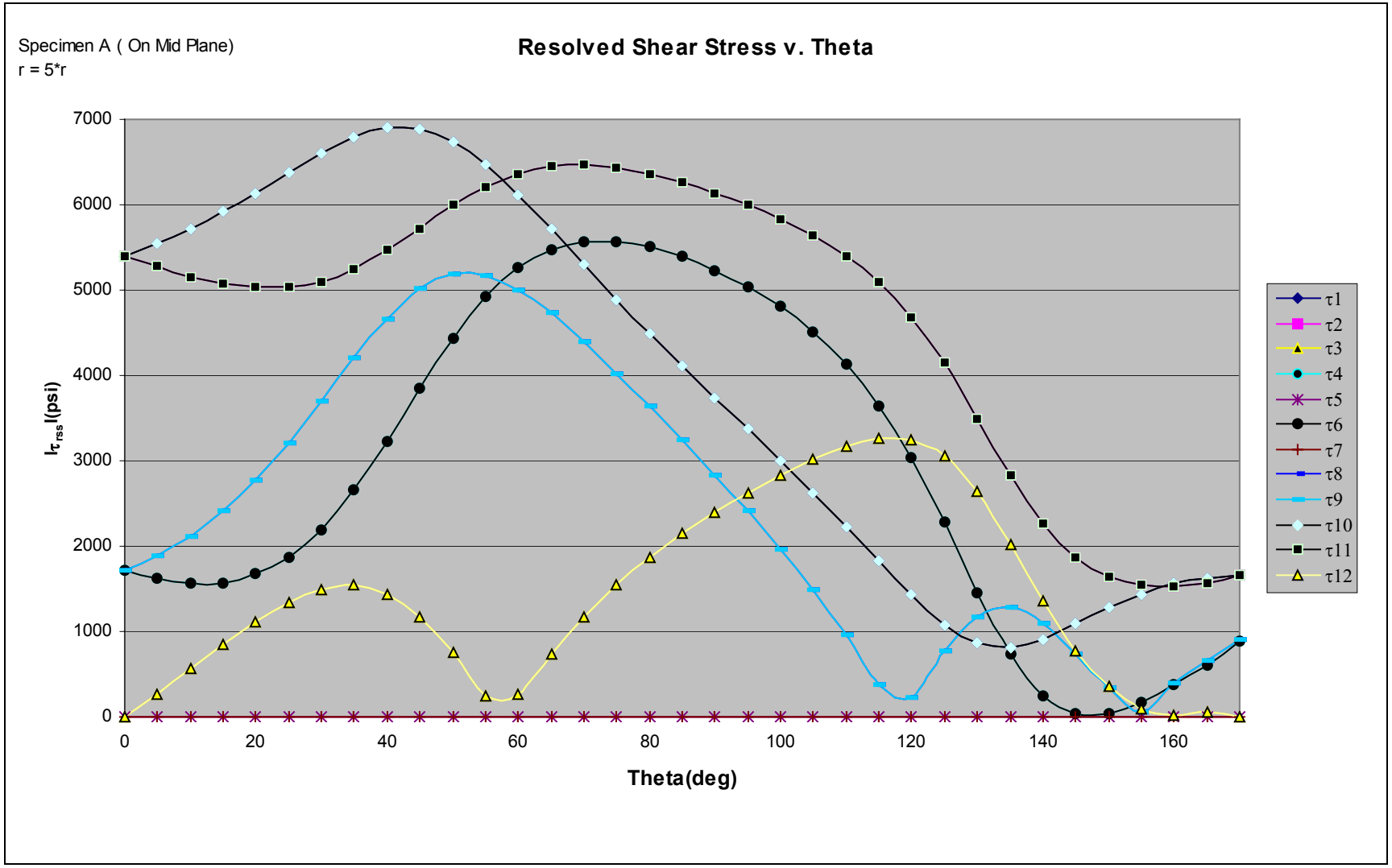

Figure 4-14 Twelve primary resolved shear stresses on the mid plane of specimen A; r = 5.0* ρ

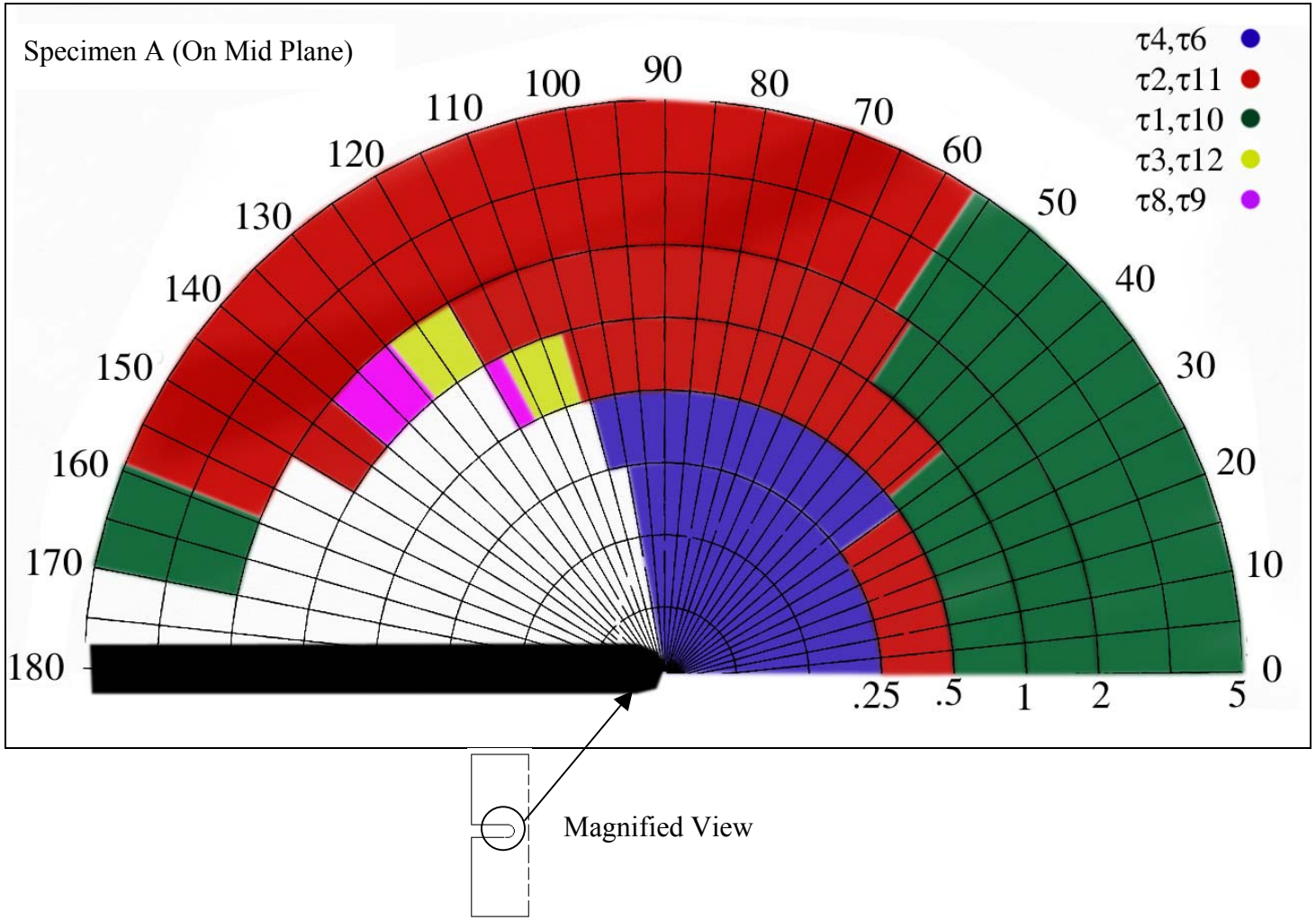

Figure 4-15 Maximum resolved shear stress on each radius occurring on the mid plane of specimen A.

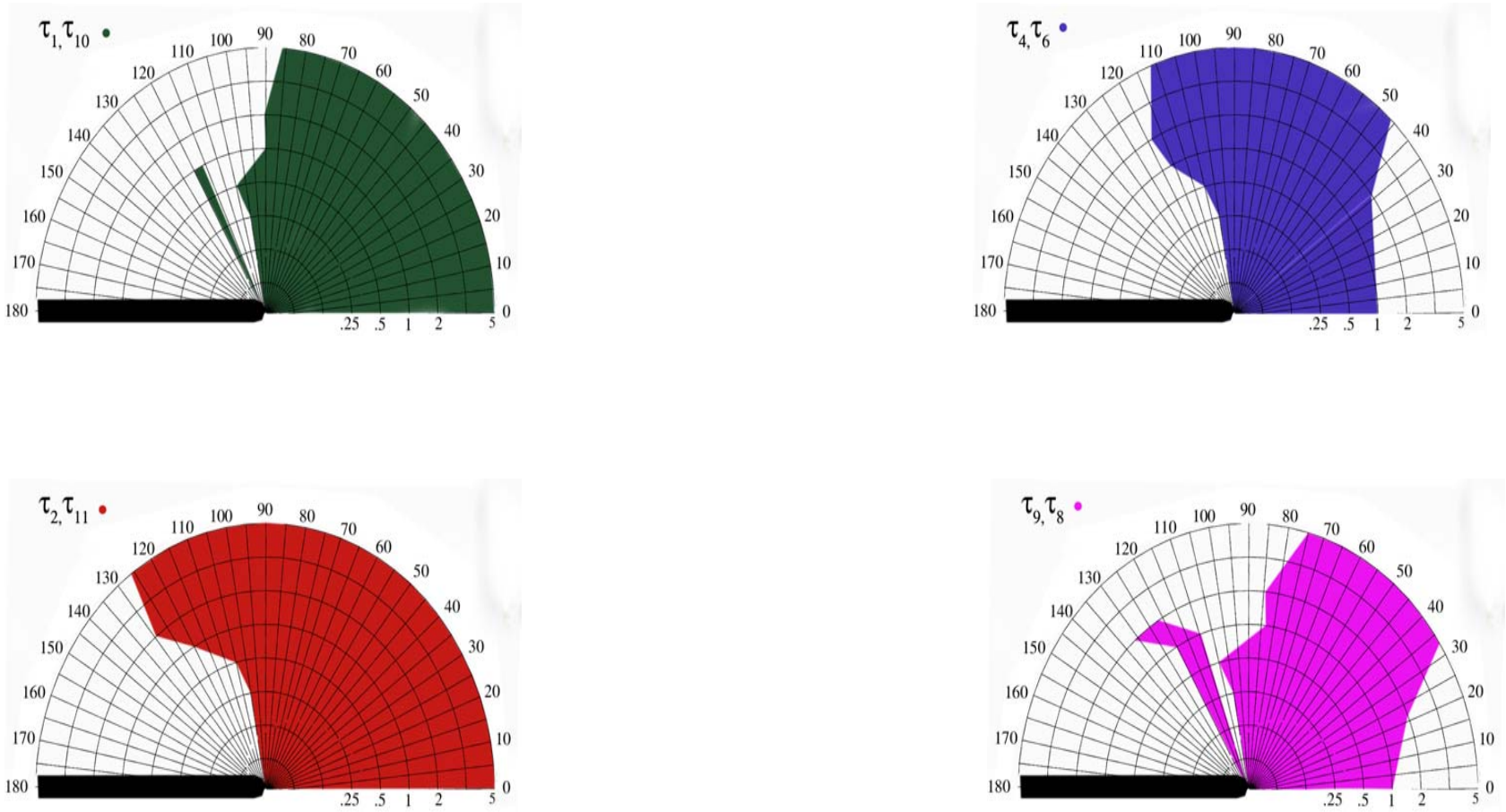

Figure 4-16 Active slip sectors on the mid plane of specimen A from 0.25*ρ to 5*ρ.

Table 4-2 Specimen A dominant slip systems (Mid plane).

Dominant Slip System Sectors									
Specimen A									
	r = 0.25*ρ			r = 0.5*ρ			r = 1*ρ		
Secto	θ	τmax	Slip System	θ	τmax	Slip System	θ	τmax	Slip System
I	0-100	τ_4	(-11-1)[10-1]	0-35	τ_2	(111)[0-11]	0-38	τ_1	(111)[10-1]
II	0-100	τ_6	(-11-1)[011]	0-35	τ_{11}	(-1-11)[101]	0-38	τ_{10}	(-1-11)[011]
III				35-105	τ_4	(-11-1)[10-1]	38-107	τ_2	(111)[0-11]
IV				35-105	τ_6	(-11-1)[011]	38-107	τ_{11}	(-1-11)[101]
V							107-117	τ_3	(111)[1-10]
VI							107-117	τ_{12}	(-1-11)[1-10]
VII							117-120	τ_8	(1-1-1)[0-11]
VIII							117-120	τ_9	(1-1-1)[101]

	r = 2.0*ρ			r = 5.0*ρ		
Secto	θ	τmax	Slip System	θ	τmax	Slip System
I	0-54	τ_1	(111)[10-1]	0-57	τ_1	(111)[10-1]
II	0-54	τ_{10}	(-1-11)[011]	0-57	τ_{10}	(-1-11)[011]
III	54-120	τ_2	(111)[0-11]	57-159	τ_2	(111)[0-11]
IV	54-120	τ_{11}	(-1-11)[101]	57-159	τ_{11}	(-1-11)[101]
V	120-129	τ_3	(111)[1-10]	159-170	τ_1	(111)[10-1]
VI	120-129	τ_{12}	(-1-11)[1-10]	159-170	τ_{10}	(-1-11)[011]
VII	129-140	τ_8	(1-1-1)[0-11]			
VIII	129-140	τ_9	(1-1-1)[101]			
IX	140-150	τ_2	(111)[0-11]			
X	140-150	τ_{11}	(-1-11)[101]			

Specimen B

The states of stress and slip systems of Specimen B were also analyzed both on the surface and on the mid plane of the specimen, in the vicinity of the notch. Both the upper and the lower half of the specimen were analyzed (from 0° to 180° and from 0° to -180°) since RSS is not symmetric about the growth axis [10-1]. The results of Specimen B on surface and mid planes are given below.

Surface Results on Upper Half of Specimen B

Twelve primary resolved shear stresses are calculated here from 0.25*ρ to 5*ρ and from 0˚ to the top of the notch. (Figures 4-18 to 4-22). The maximum RSS near the notch is τ_9=27,100 psi at radius = 0.5*ρ and at 105˚. This stress is a fair amount higher and in different slip systems than the maximum RSS for Specimen A on the surface (max RSS τ_2=25,000 psi), though it does occur at the same location. The dominant slip system and sectors were determined for each radius by the overall maximum RSS, (Table 4-3).

Like Specimen A, The RSS change values and shifts positions relative to each other with respect to theta. The effects of theta on resolved shear stresses can be seen in figure 4-18 to figure 4-22. It also shows dominant systems on each of the four possible primary slip planes in the RSS fields .In conclusion the RSS field is dominated by τ_1 on the (111) plane and by τ_4, τ_5, τ_6, τ_8, τ_9, τ_{10} and τ_{11} on the {-1-11} family of planes.

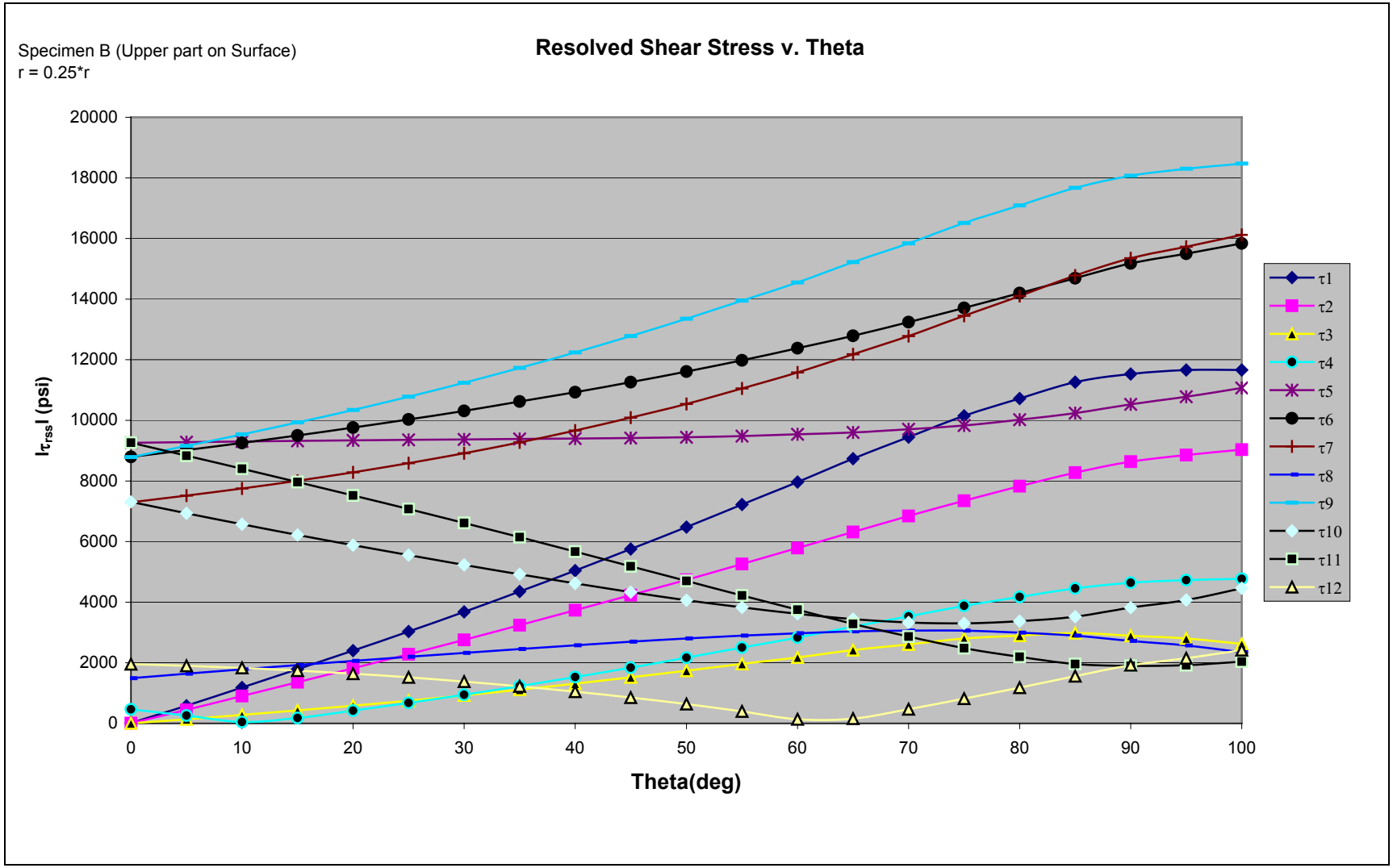

Figure 4-18 Twelve primary resolved shear stresses on the upper half of the surface of specimen B; r = 0.25* ρ

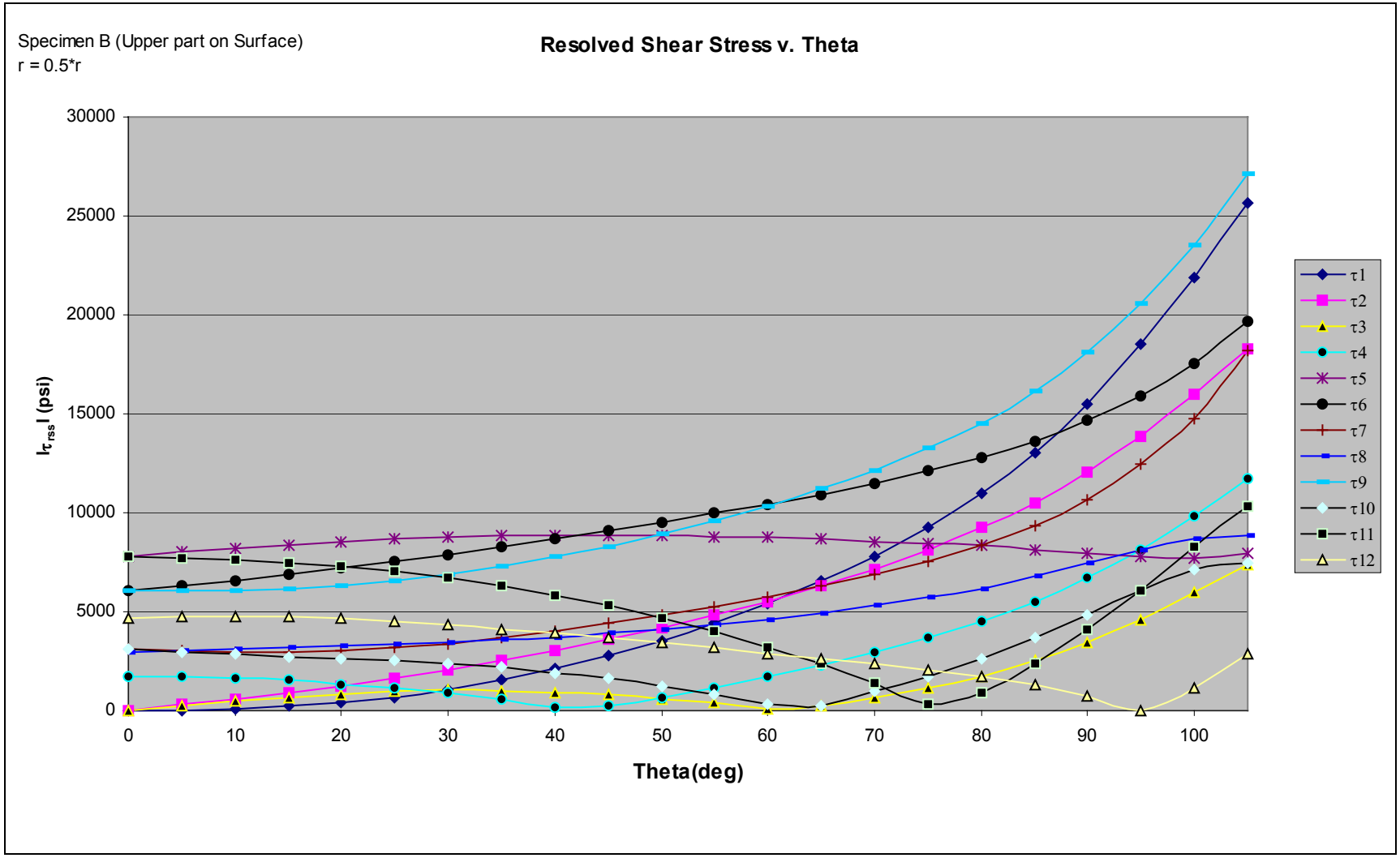

Figure 4-19 Twelve primary resolved shear stresses on the upper half of the surface of specimen B; r = 0.5* ρ

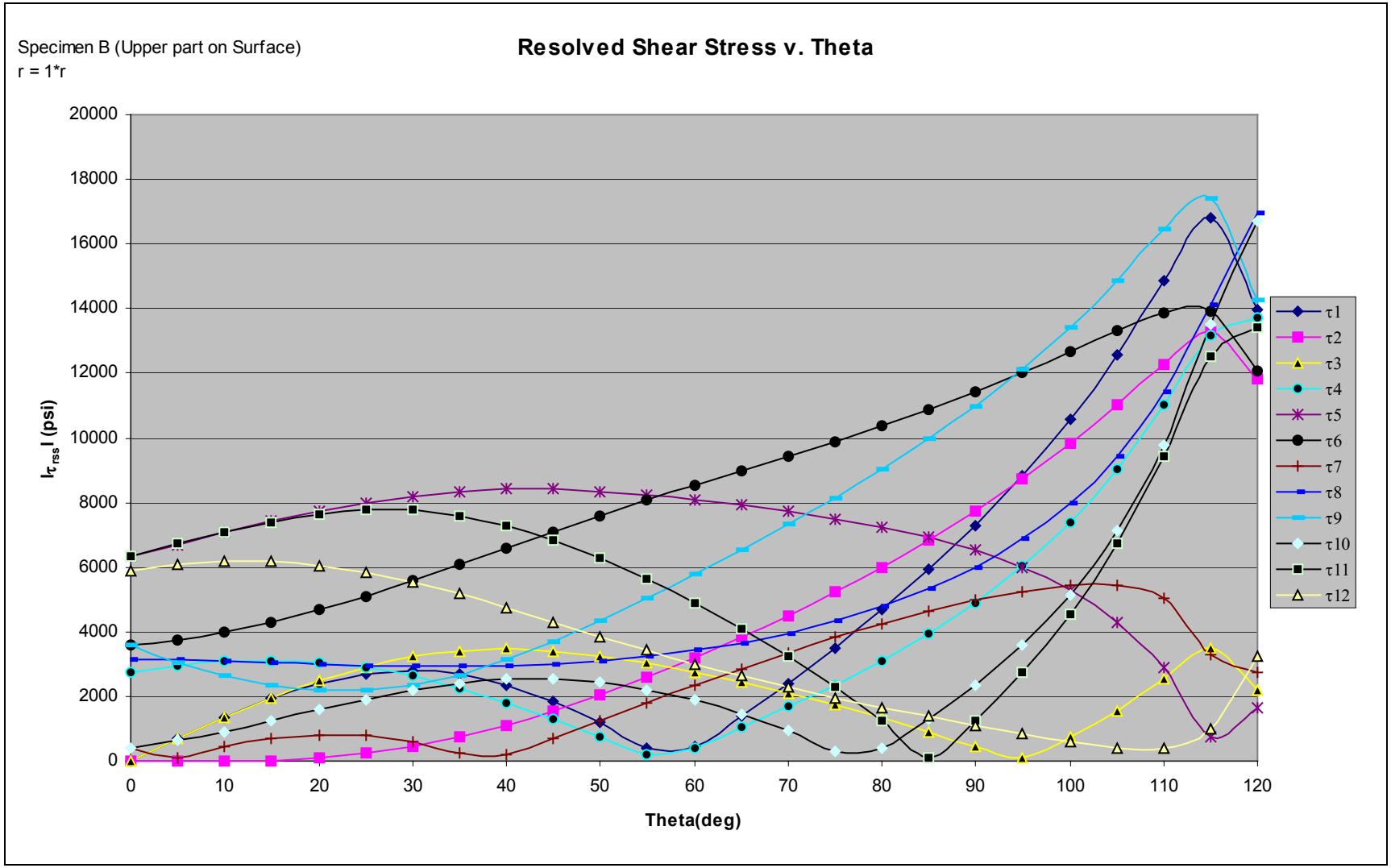

Figure 4-20 Twelve primary resolved shear stresses on the upper half of the surface of specimen B; r = 1* ρ

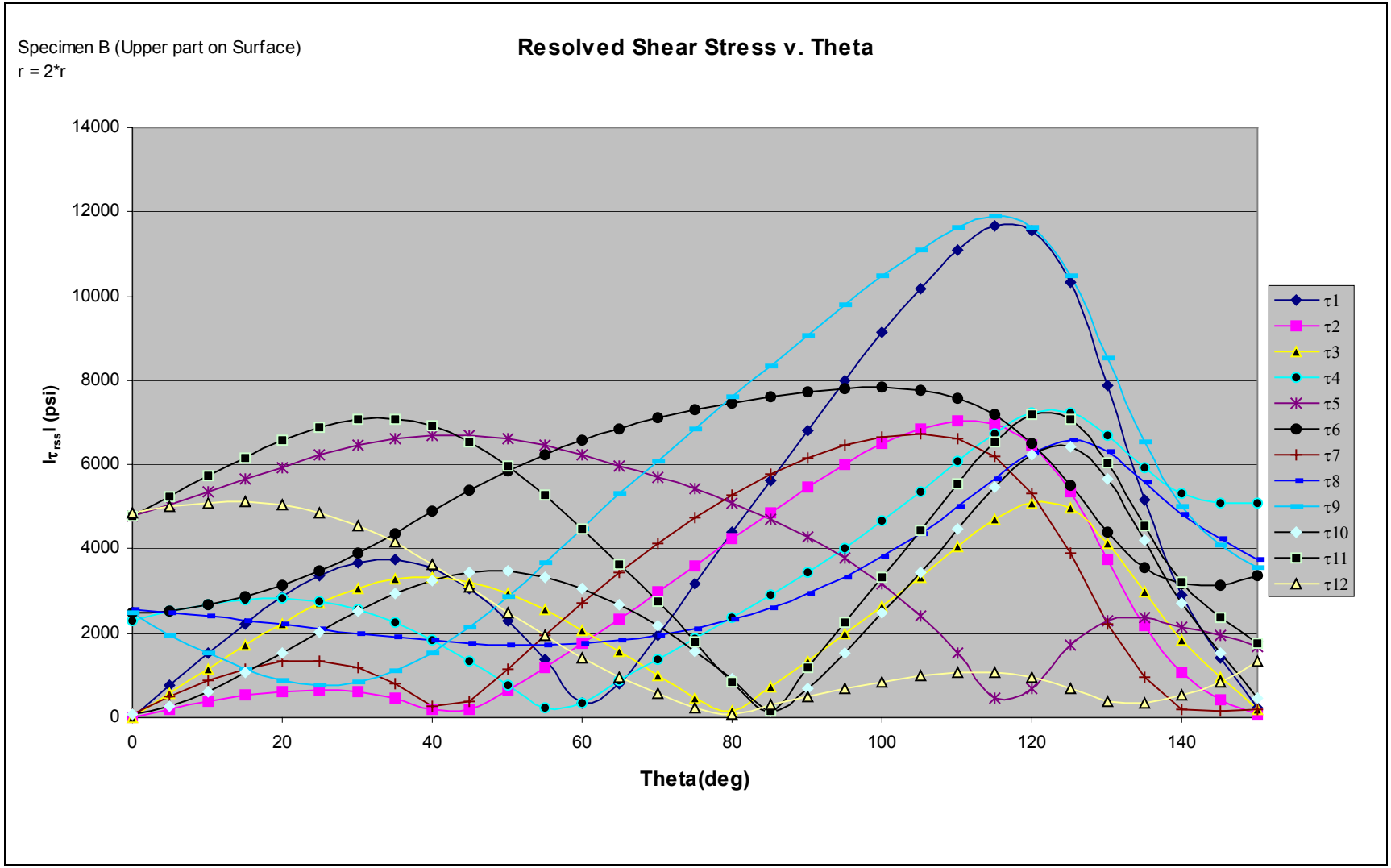

Figure 4-21 Twelve primary resolved shear stresses on the upper half of the surface of specimen B; r = 2* ρ

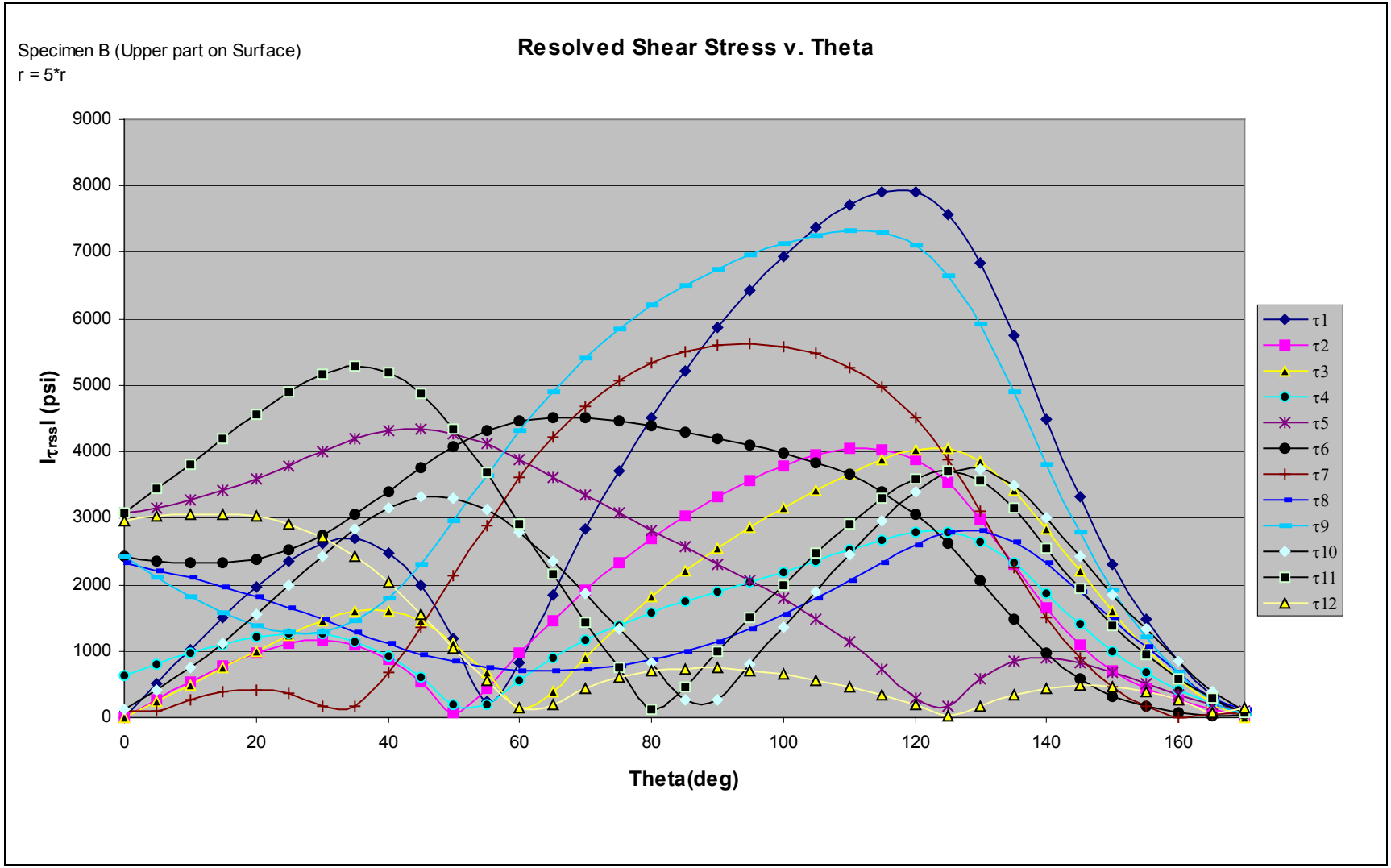

Figure 4-22 Twelve primary resolved shear stresses on the upper half of the surface of specimen B; r = 5* ρ

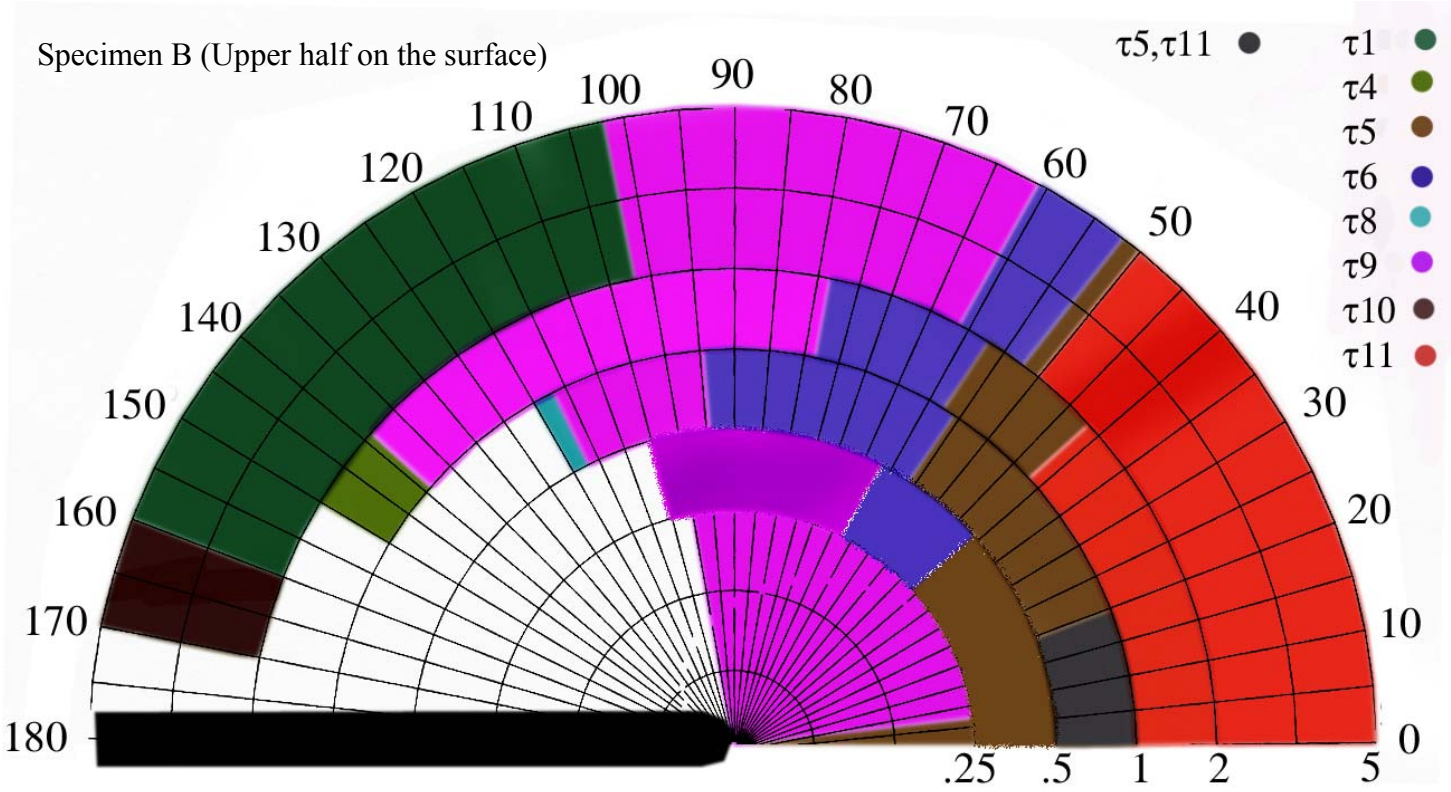

Figure 4-23 Maximum resolved shear stress on each radius occurring on the upper half of the surface of specimen B.

Table 4-3 Specimen B dominant slip system. (Upper half on surface).

Dominant Slip System Sectors Specimen B									
	r = 0.25*ρ			r = 0.5*ρ			r = 1*ρ		
Sector	θ	τ_{max}	Slip System	θ	τ_{max}	Slip System	θ	τ_{max}	Slip System
I	0-7	τ_5	(-11-1)[110]	0-42	τ_5	(-11-1)[110]	0-19	τ_5	(-11-1)[110]
II	7-100	τ_9	(1-1-1)[101]	42-62	τ_6	(-11-1)[011]	0-19	τ_{11}	(-1-11)[101]
III				62-105	τ_9	(1-1-1)[101]	19-56	τ_5	(-11-1)[110]
IV							56-94	τ_6	(-11-1)[011]
V							94-117	τ_9	(1-1-1)[101]
VI							117-120	τ_8	(1-1-1)[0-11]

	r = 2.0*ρ			r = 5.0*ρ		
Sector	θ	τ_{max}	Slip System	θ	τ_{max}	Slip System
I	0-43	τ_{11}	(-1-11)[101]	0-50	τ_{11}	(-1-11)[101]
II	43-57	τ_5	(-11-1)[110]	50-53	τ_5	(-11-1)[110]
III	57-78	τ_6	(-11-1)[011]	53-61	τ_6	(-11-1)[011]
IV	78-138	τ_9	(1-1-1)[101]	61-103	τ_9	(1-1-1)[101]
V	138-150	τ_4	(-11-1)[10-1]	103-160	τ_1	(111)[10-1]
VI				160-170	τ_{10}	(-1-11)[011]

Surface Results on Lower Half of Specimen B

Twelve primary RSS are calculated from 0.25*ρ to 5*ρ and from 0˚ to the bottom of the notch (Figures 4-24 to 4-28). The maximum RSS near the notch is τ_{11}=26,290 psi at radius = 0.5*ρ and at 105˚ angle. This stress is lower than maximum RSS of upper half of Specimen B and quite higher than the maximum RSS for Specimen A on the surface, but it occurs at the same location in the RSS field. Here also, the dominant slip system and sectors were determined for each radius. (Table 4-4).

Here also the RSS change values and shifts positions relative to each other with respect to theta. Overall the RSS field is dominated by τ_1 and τ_3 on the (111) plane and by τ_4, τ_5, τ_6, τ_7, τ_8, τ_9, τ_{10} τ_{11}, and τ_{12} on the {-1-11} family of planes.

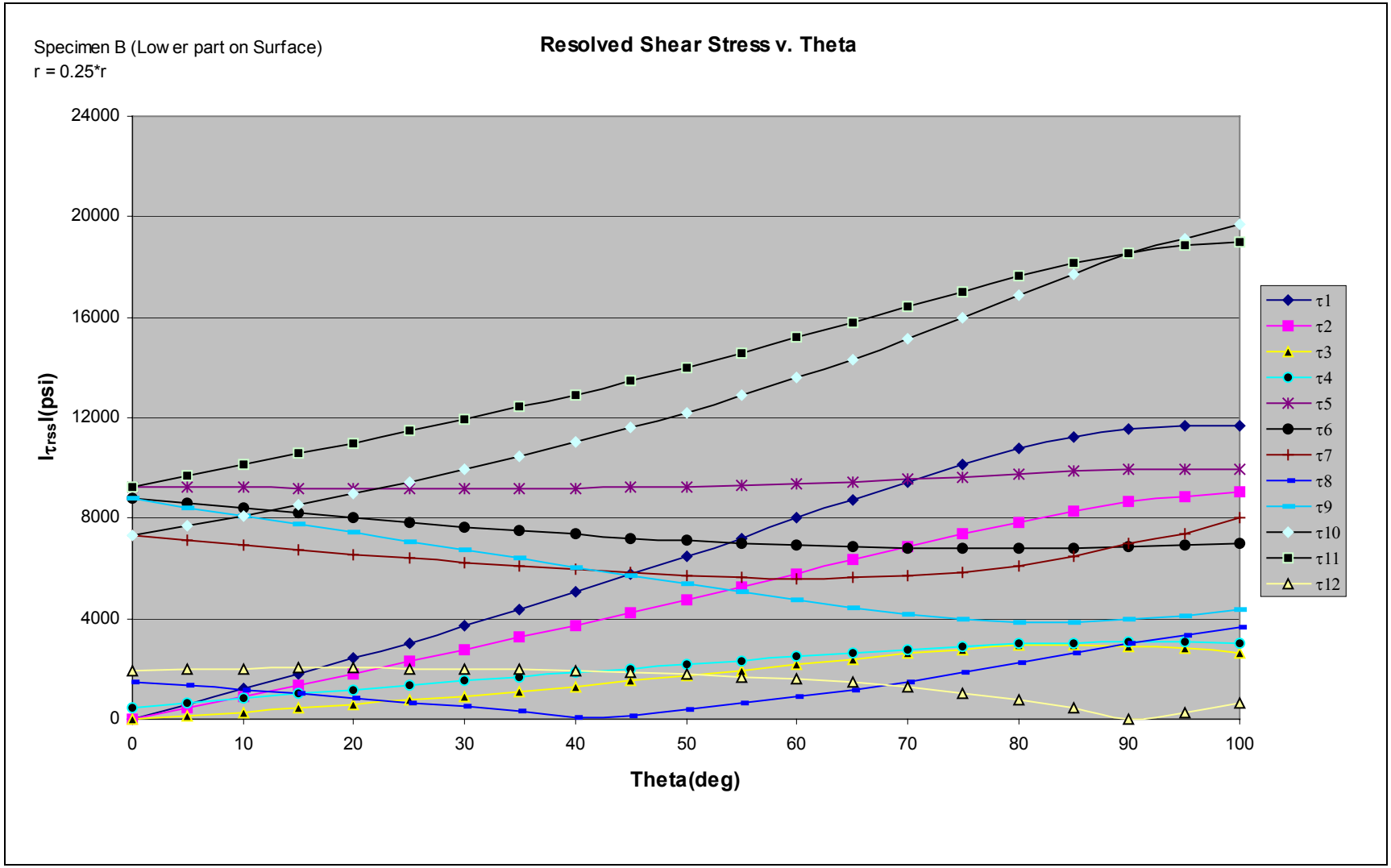

Figure 4-24 Twelve primary resolved shear stresses on the lower half of the surface of specimen B; r = 0.25* ρ

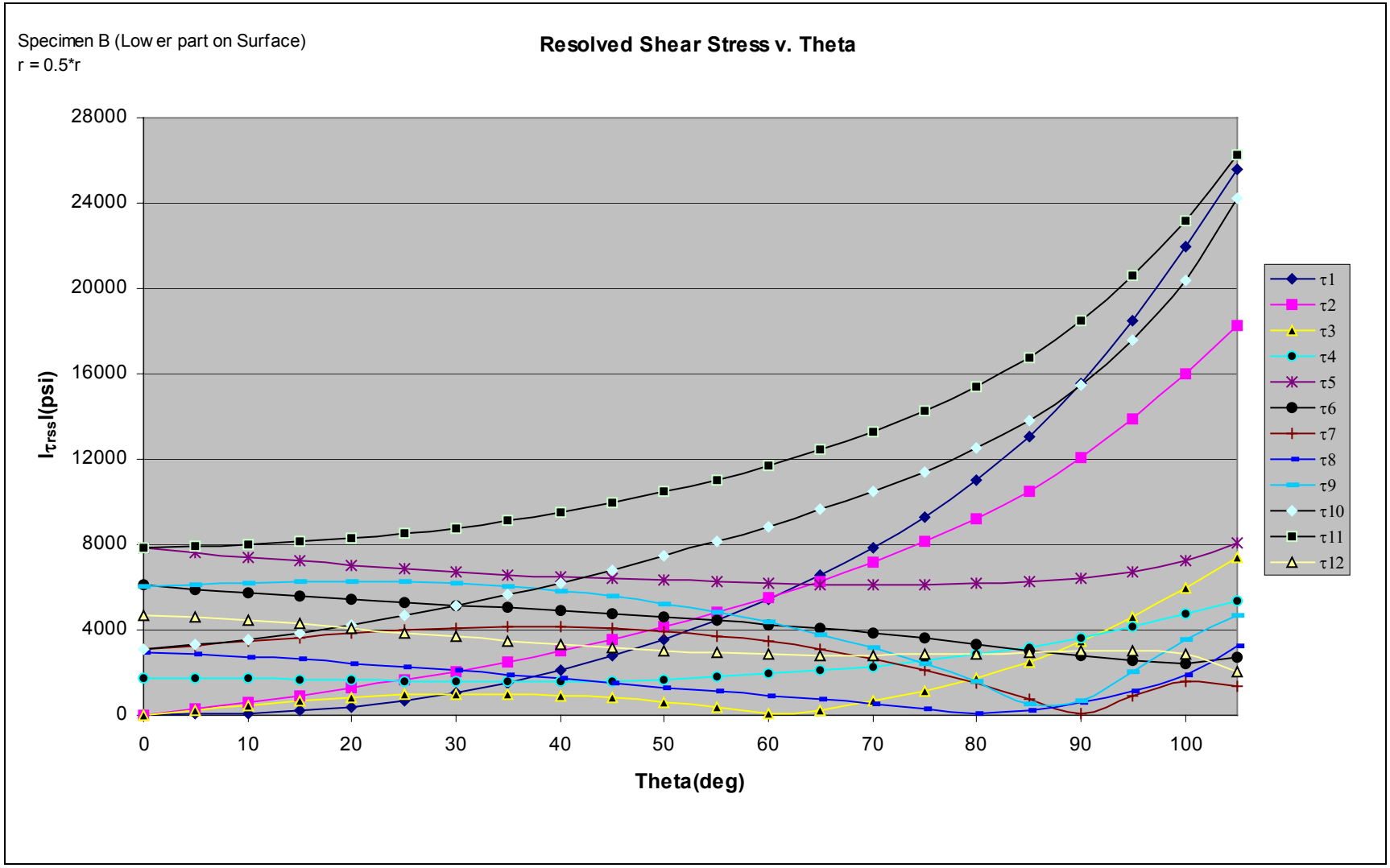

Figure 4-25 Twelve primary resolved shear stresses on the lower half of the surface of specimen B; r = 0.5* ρ

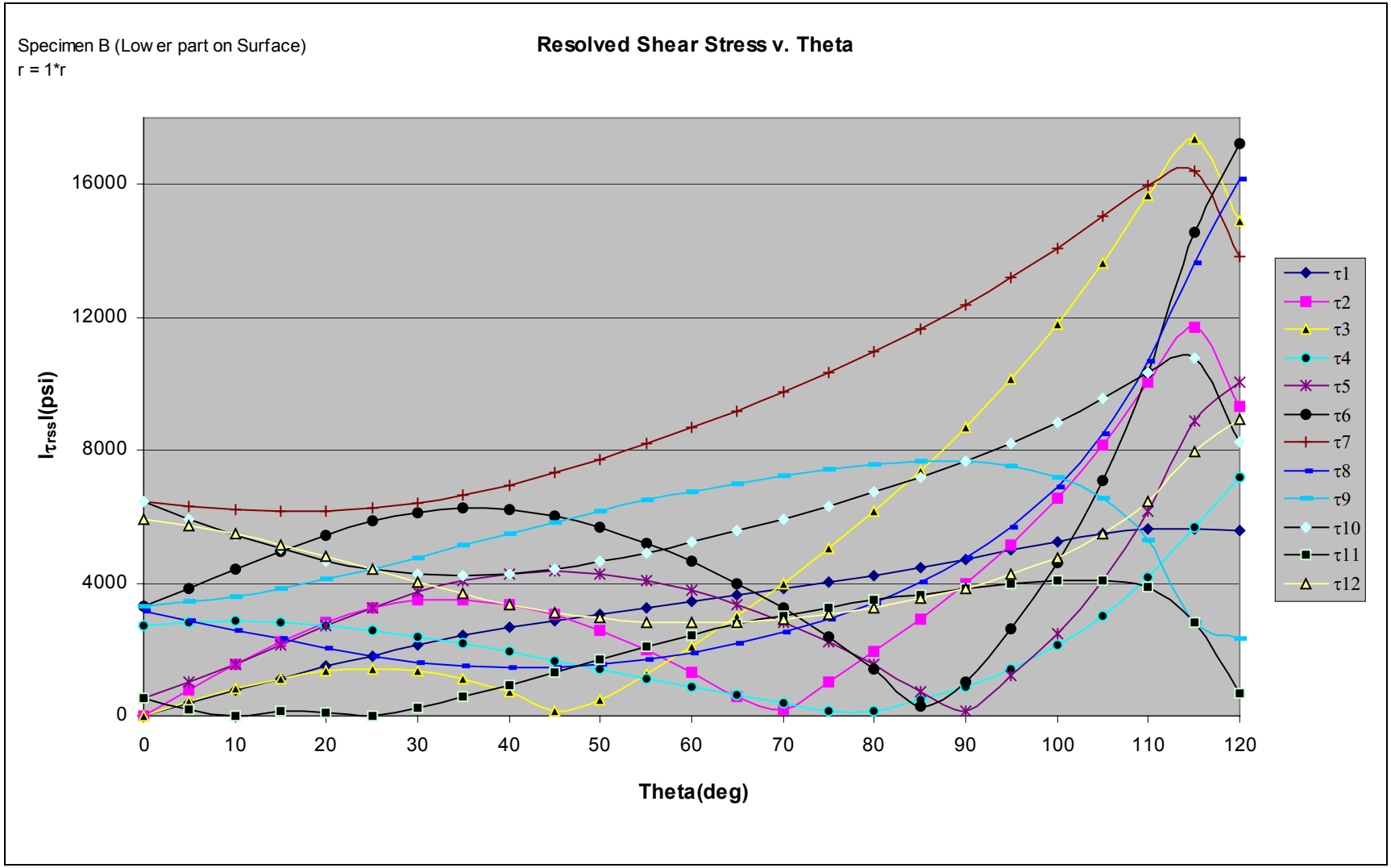

Figure 4-26 Twelve primary resolved shear stresses on the lower half of the surface of specimen B; r = 1* ρ

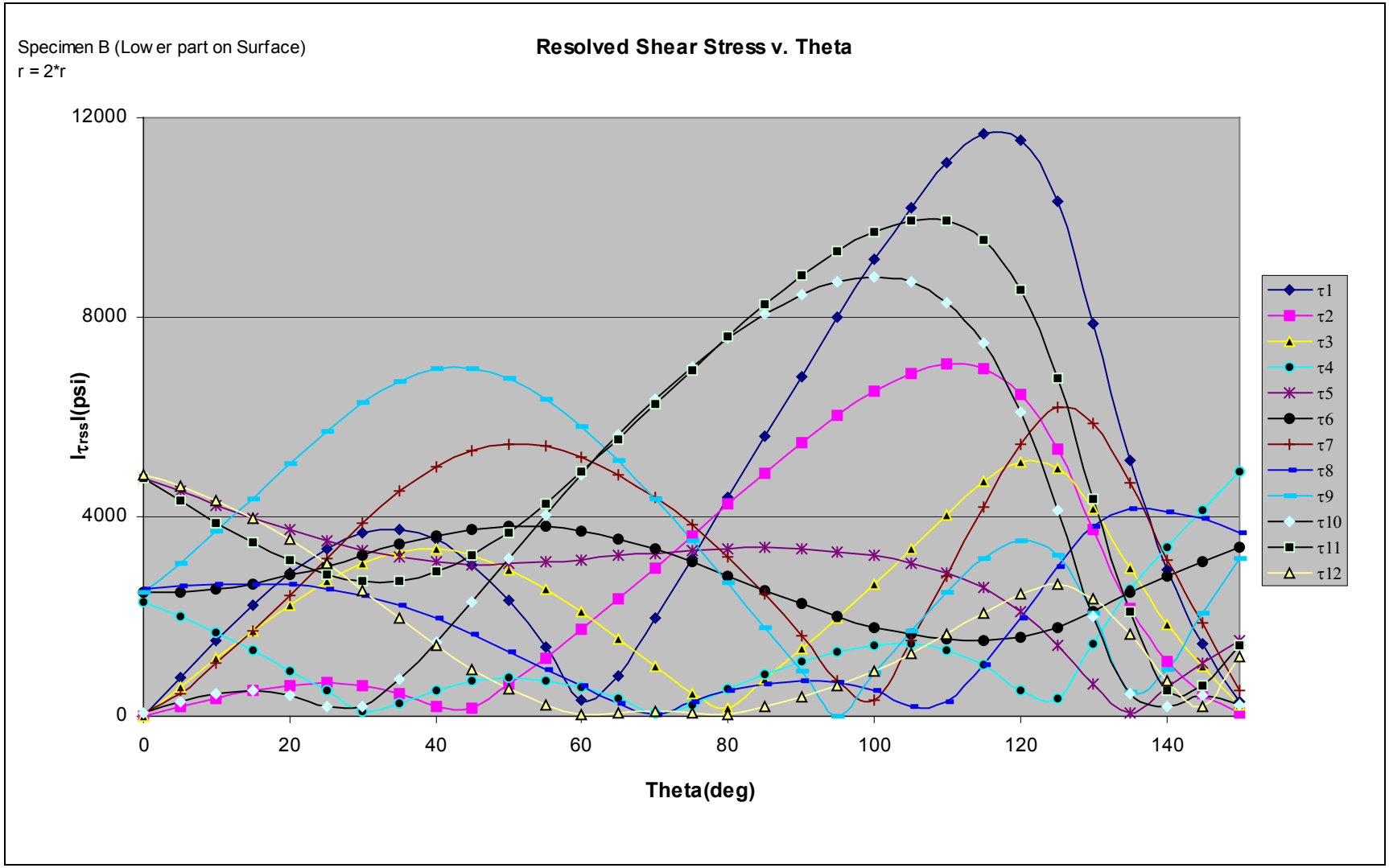

Figure 4-27 Twelve primary resolved shear stresses on the lower half of the surface of specimen B; r = 2* ρ

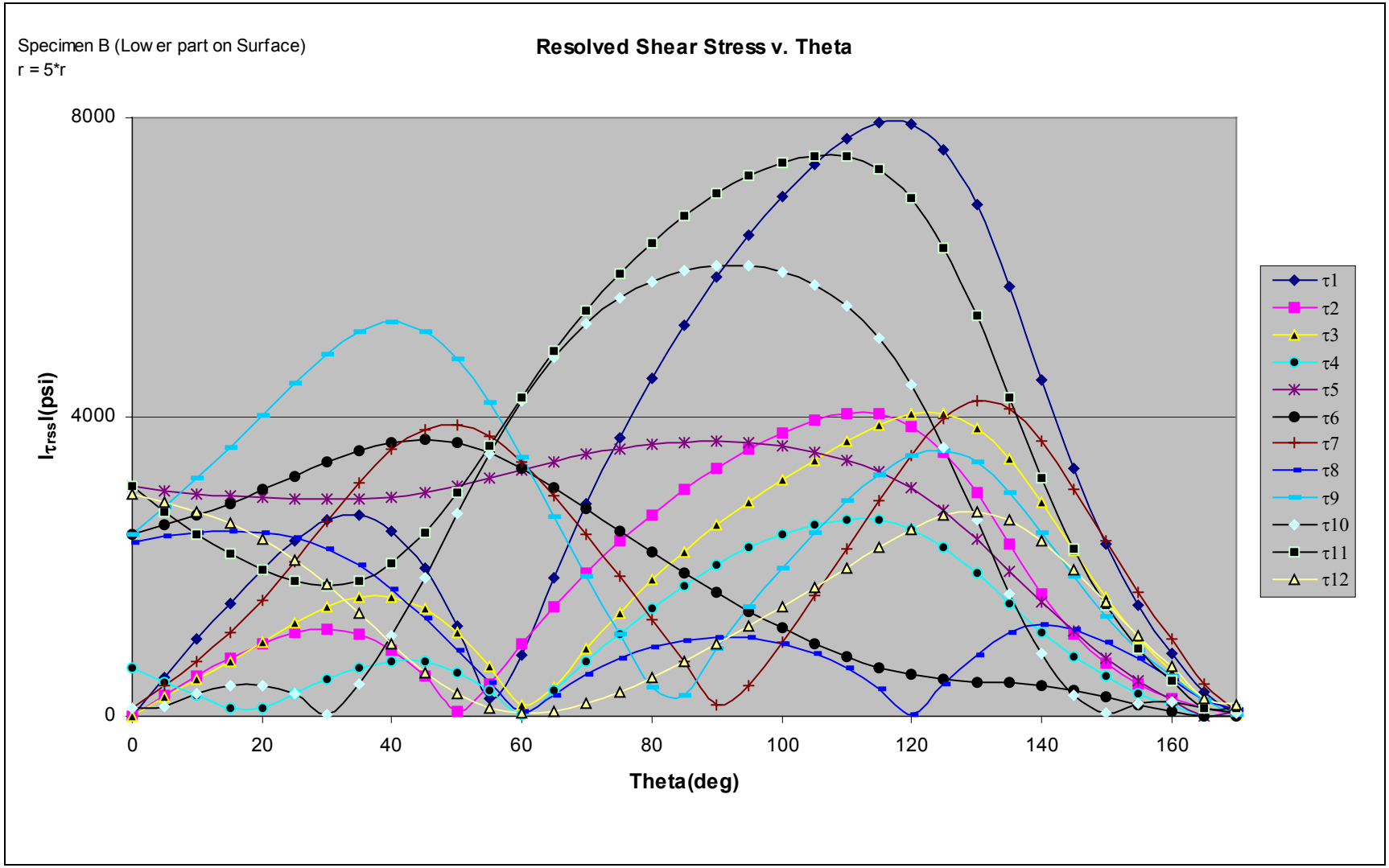

Figure 4-28 Twelve primary resolved shear stresses on the lower half of the surface of specimen B; r = 5* ρ

Specimen B (Lower half on the surface)

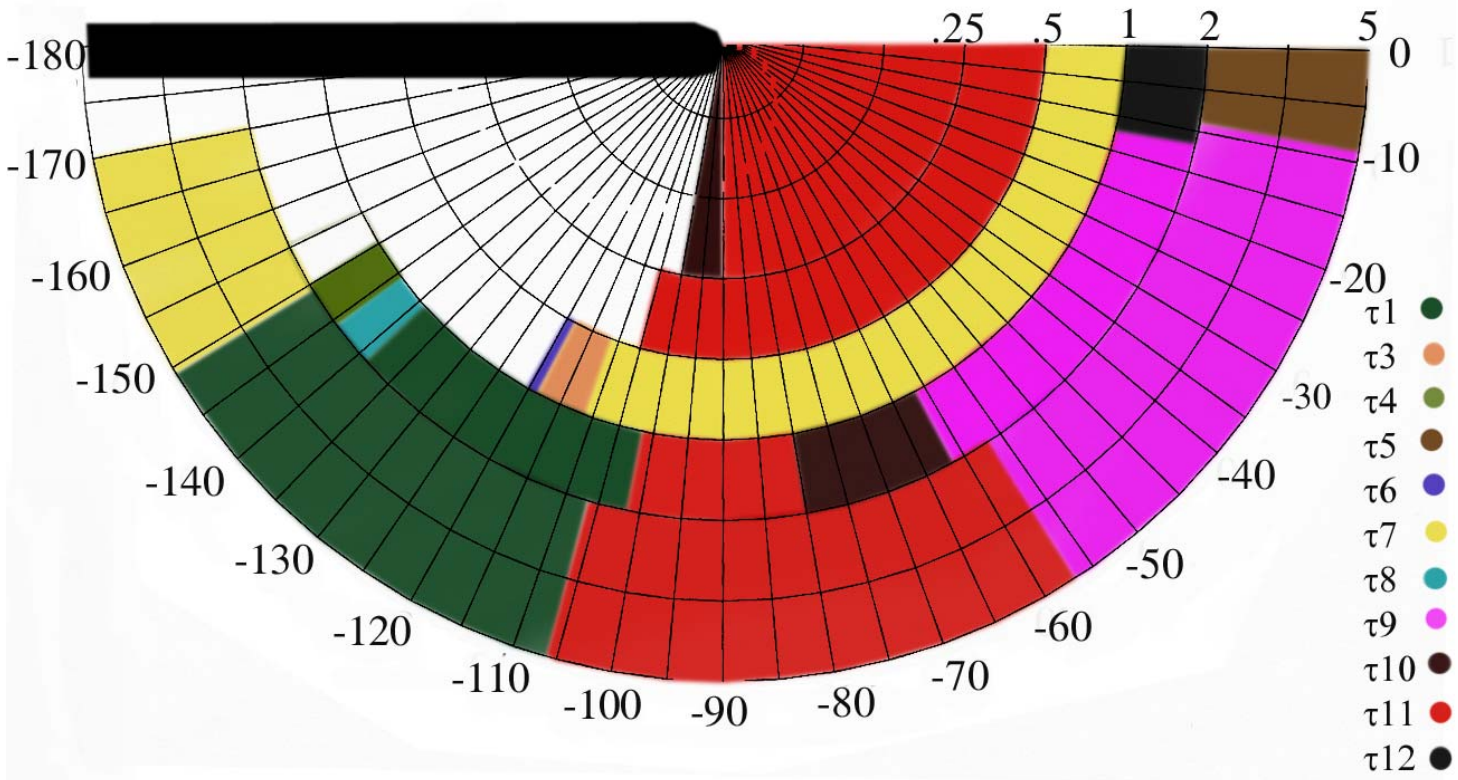

Figure 4-29 Maximum resolved shear stress on each radius occurring on the lower half of the surface of specimen B.

Table 4-4 Specimen B dominant slip system (Lower half on surface)

Dominant Slip System Sectors Specimen B									
	r = 0.25*ρ			r = 0.5*ρ			r = 1*ρ		
Sector	θ	τmax	Slip System	θ	τmax	Slip System	θ	τmax	Slip System
I	0-90	τ_{11}	(-1-11)[101]	0-105	τ_{11}	(-1-11)[101]	0-111	τ_7	(1-1-1)[110]
II	90-100	τ_{10}	(-1-11)[011]				111-118	τ_3	(111)[1-10]
III							118-120	τ_6	(-11-1)[011]

	r = 2.0*ρ			r = 5.0*ρ		
Sector	θ	τmax	Slip System	θ	τmax	Slip System
I	0-13	τ_{12}	(-1-11)[1-10]	0-8	τ_5	(-11-1)[110]
II	13-63	τ_9	(1-1-1)[101]	8-57	τ_9	(1-1-1)[101]
III	63-80	τ_{10}	(-1-11)[011]	57-106	τ_{11}	(-1-11)[101]
IV	80-103	τ_{11}	(-1-11)[101]	106-149	τ_1	(111)[10-1]
V	103-137	τ_1	(111)[10-1]	149-170	τ_7	(1-1-1)[110]
VI	137-144	τ_8	(1-1-1)[0-11]			
VII	144-150	τ_4	(-11-1)[10-1]			

Mid Planes Results on Upper Half of Specimen B

Twelve primary resolved shear stresses are calculated here from 0.25*ρ to 5*ρ and from 0˚ to the top of the notch (Figures 4-30 to 4-34). The maximum RSS near the notch is τ_1=35,690 psi at a radius = 0.5*ρ and at a 105˚ angle. Again for Specimen B the RSS on mid plane is higher than RSS on the surface, occurring in a different slip systems but at the same location.

The RSS change values and shifts positions relative to each other with respect to theta and radius. The dominating slip systems are τ_1 on the (111) plane, τ_7, τ_8, τ_9 and τ_{10}, τ_{11} on (1-1-1) and (-1-11) planes respectively.

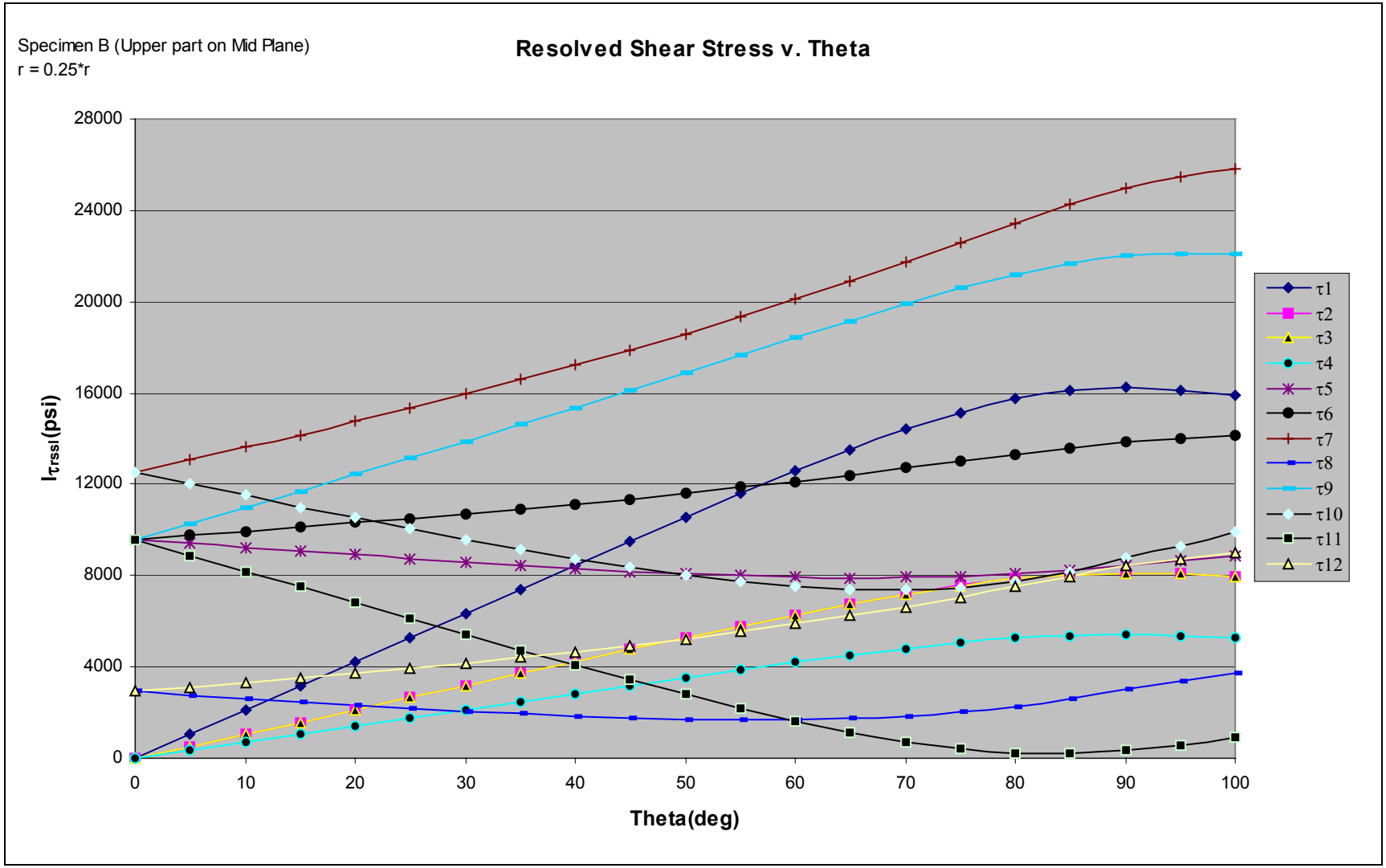

Figure 4-30 Twelve primary resolved shear stresses on the upper half of the mid plane of specimen B; r = 0.25* ρ

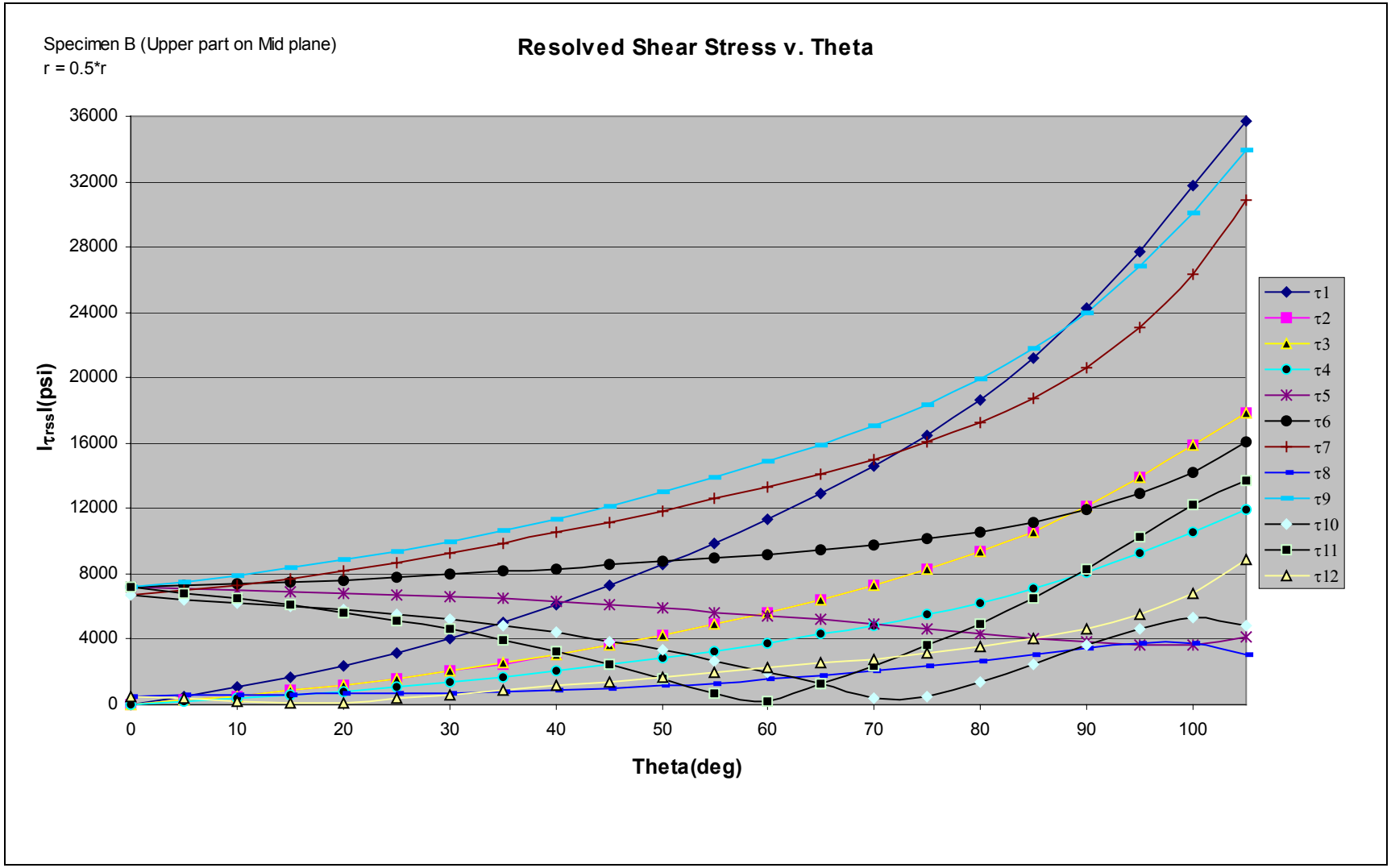

Figure 4-31 Twelve primary resolved shear stresses on the upper half of the mid plane of specimen B; r = 0.5* ρ

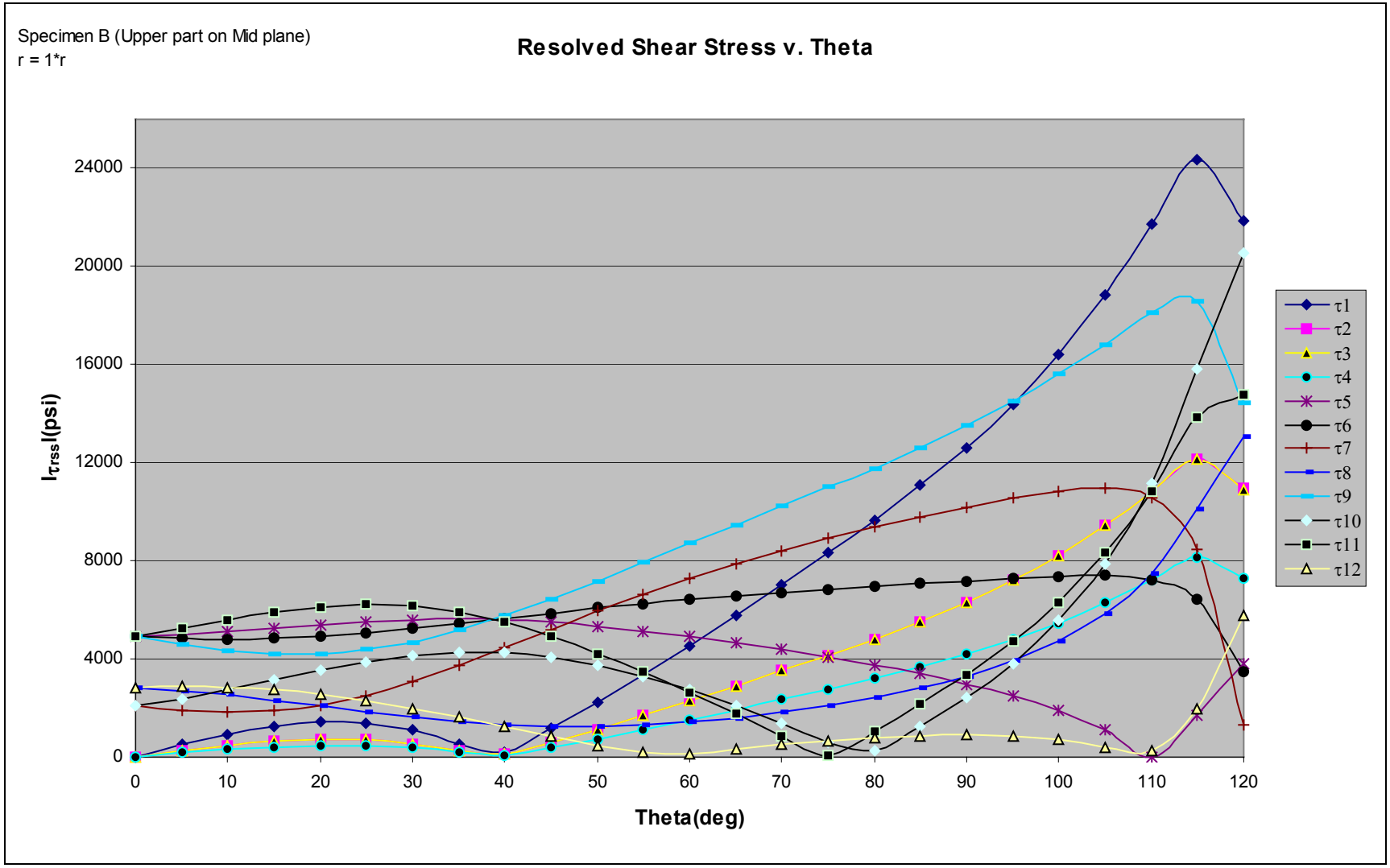

Figure 4-32 Twelve primary resolved shear stresses on the upper half of the mid plane of specimen B; r = 1* ρ

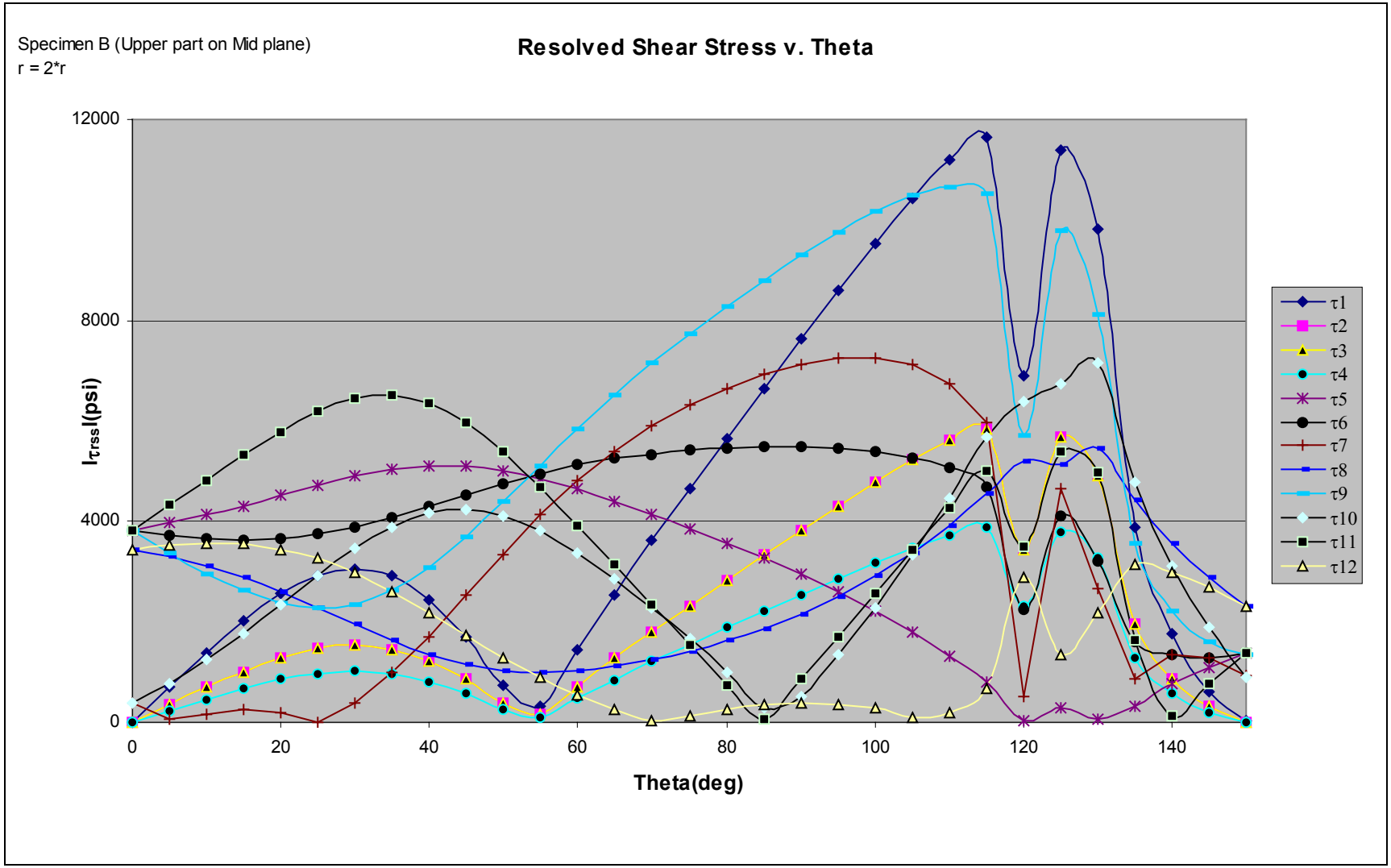

Figure 4-33 Twelve primary resolved shear stresses on the upper half of the mid plane of specimen B; r = 2* ρ

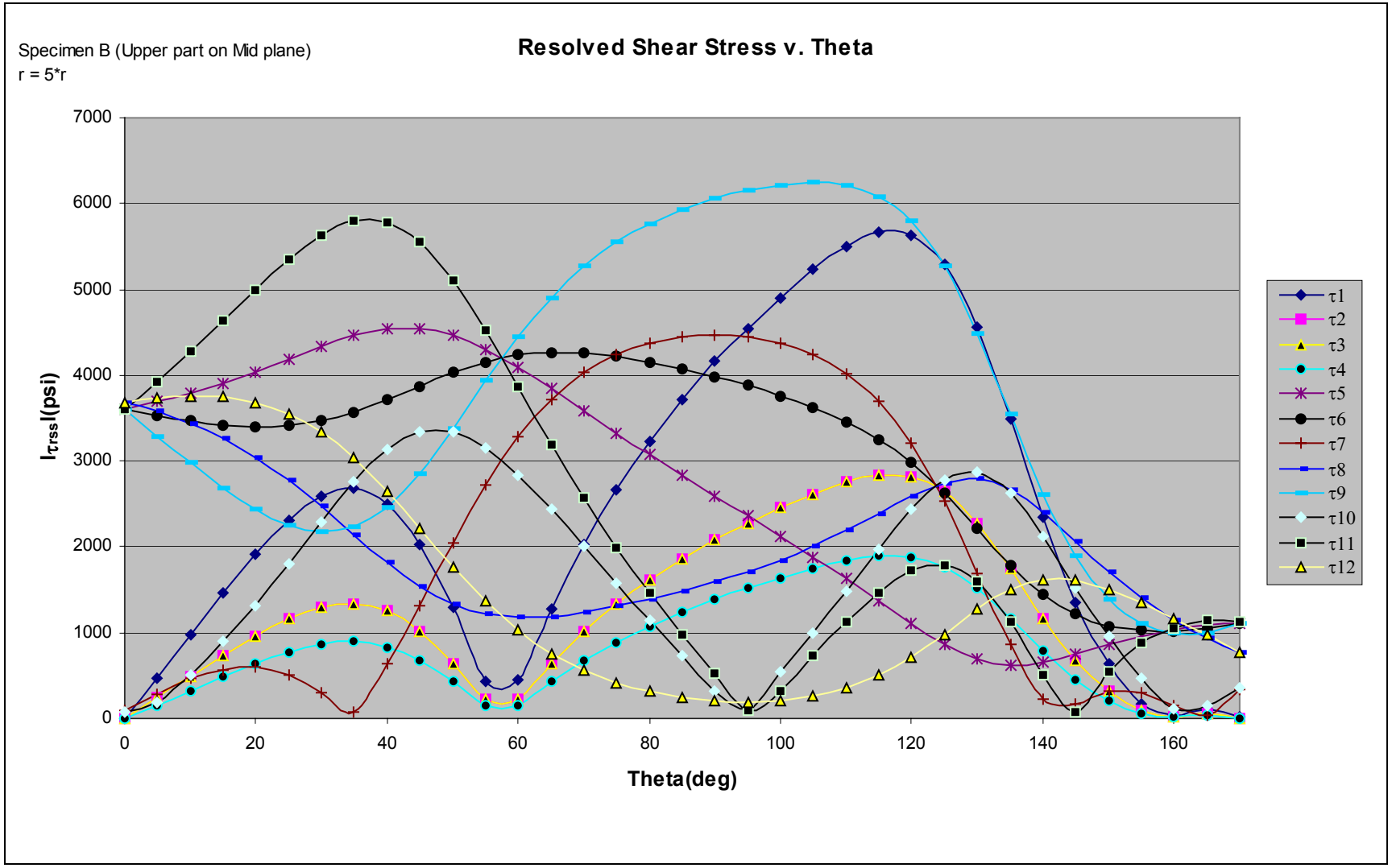

Figure 4-34 Twelve primary resolved shear stresses on the upper half of the mid plane of specimen B; r = 5* ρ

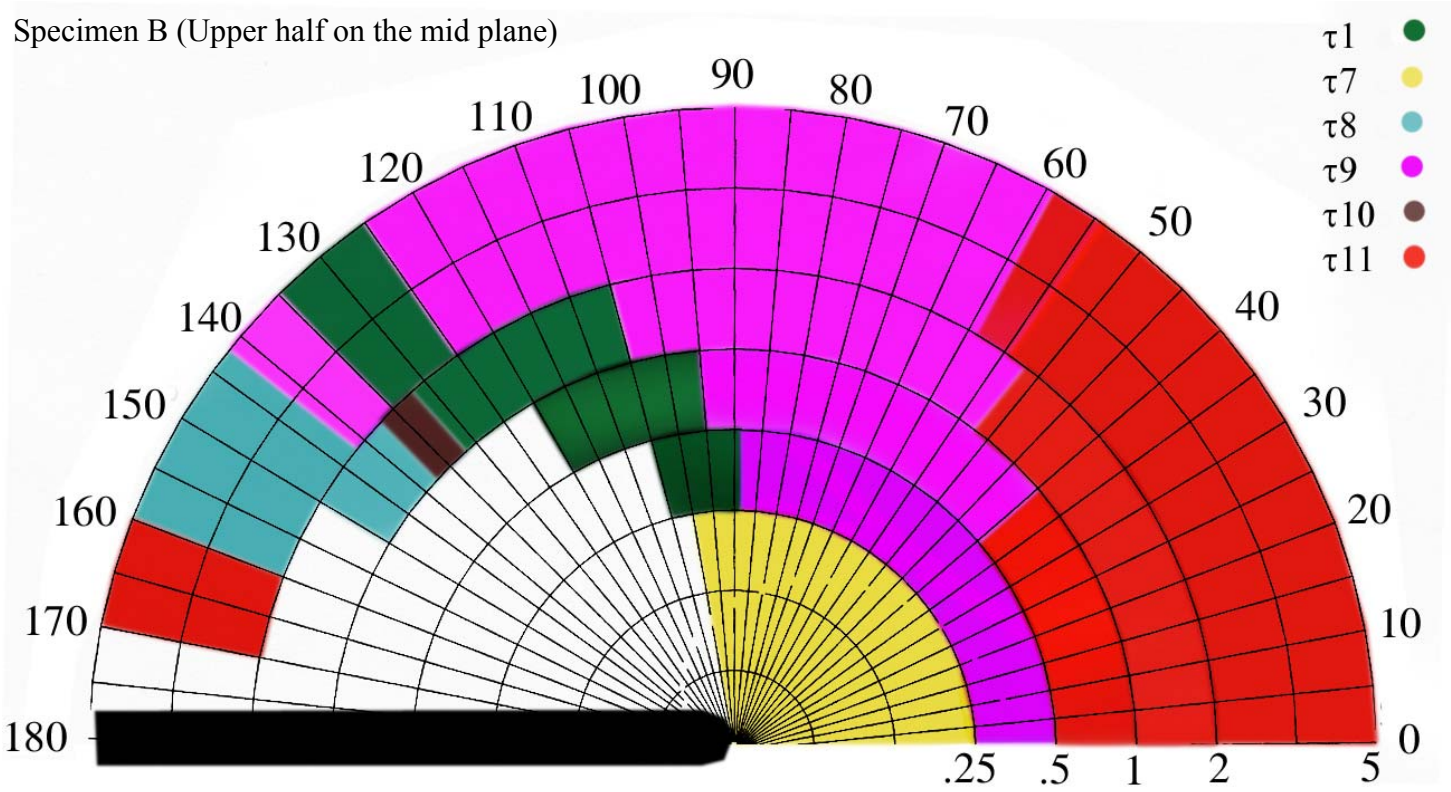

Figure 4-35 Maximum resolved shear stress on each radius occurring on the upper half of the mid plane of specimen B.

Table 4-5 Specimen B dominant slip system sectors (Upper half on mid plane)

Dominant Slip System Sectors Specimen B									
	r = 0.25*ρ			r = 0.5*ρ			r = 1*ρ		
Sector	θ	τmax	Slip System	θ	τmax	Slip System	θ	τmax	Slip System
I	0-100	τ_7	(1-1-1)[110]	0-88	τ_9	(1-1-1)[101	0-39	τ_{11}	(-1-11)[101]
II				88-105	τ_1	(111)[10-1]	39-95	τ_9	(1-1-1)[101]
III							95-120	τ_1	(111)[10-1]

	r = 2.0*ρ			r = 5.0*ρ		
Sector	θ	τmax	Slip System	θ	τmax	Slip System
I	0-54	τ_{11}	(-1-11)[101]	0-58	τ_{11}	(-1-11)[101]
II	54-105	τ_9	(1-1-1)[101]	58-125	τ_9	(1-1-1)[101]
III	105-134	τ_1	(111)[10-1]	125-135	τ_1	(111)[10-1]
IV	134-137	τ_{10}	(-1-11)[011]	135-143	τ_9	(1-1-1)[101]
V	137-150	τ_8	(1-1-1)[0-11]	143-160	τ_8	(1-1-1)[0-11]
VI				160-170	τ_{11}	(-1-11)[101]

Mid Planes Results on Lower Half of Specimen B

Twelve primary resolved shear stresses are calculated here from 0.25*ρ to 5*ρ (in radial direction) and from 0˚ to the bottom of the notch (Figures 4-36 to 4-40). The maximum RSS near the notch is τ_{11}=35,670 psi at a radius = 0.5*ρ and at a 105˚ angle. This stress is lower than the RSS on the upper half of mid plane of Specimen B.

The RSS change values and shifts positions relative to each other with respect to theta and radius. Here the angle for the dominant slip systems are the same as compared with the dominant slip systems on the upper half of the mid plane of Specimen B but the slip systems are interchanging. In conclusion the RSS field is dominated by τ_1 on the (111) plane and by τ_7, τ_9, and τ_{10}, τ_{11} τ_{12} on (1-1-1) and (-1-11) planes respectively.

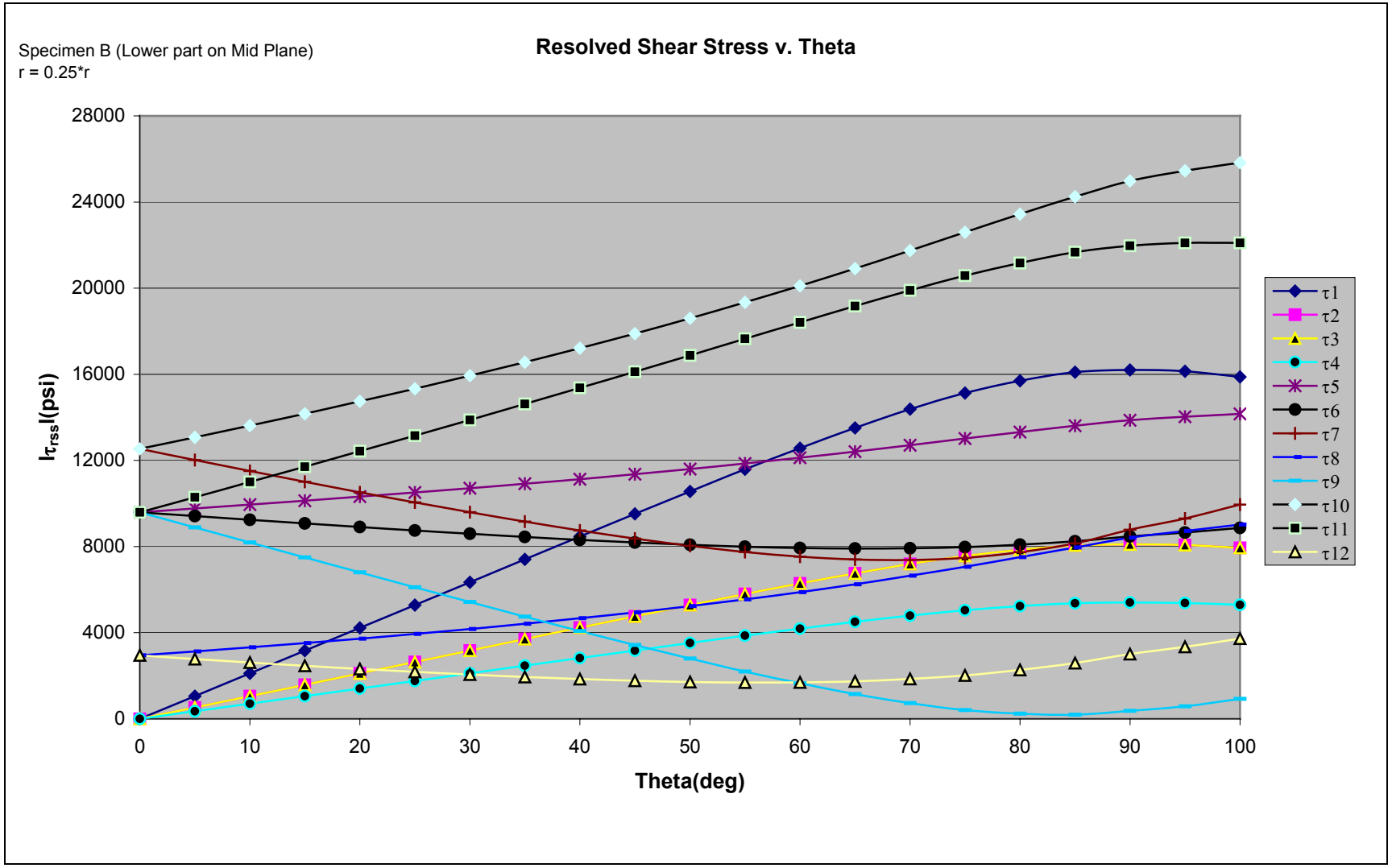

Figure 4-36 Twelve primary resolved shear stresses on the lower half of the mid plane of specimen B; r = 0.25* ρ

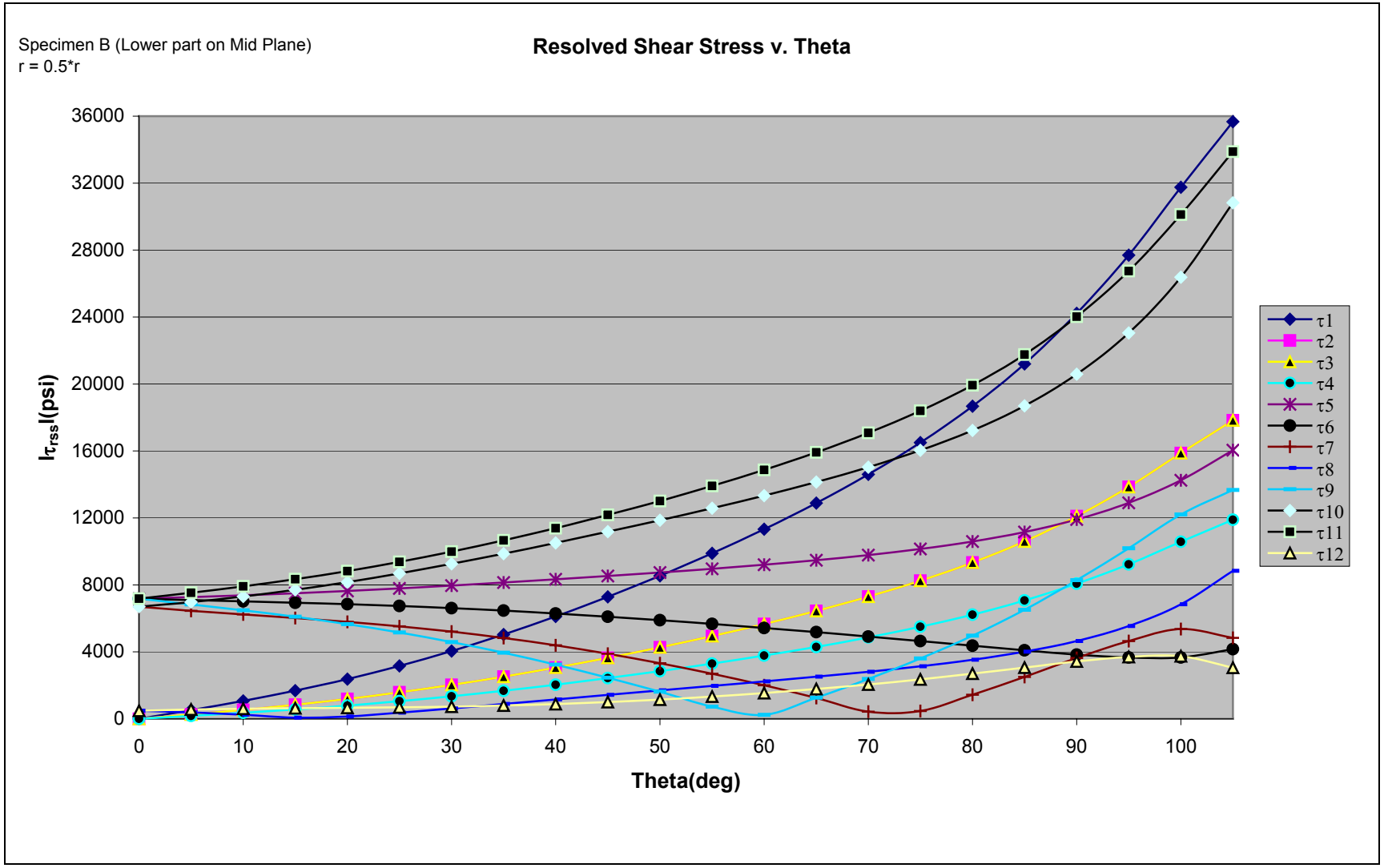

Figure 4-37 Twelve primary resolved shear stresses on the lower half of the mid plane of specimen B; r = 0.5* ρ

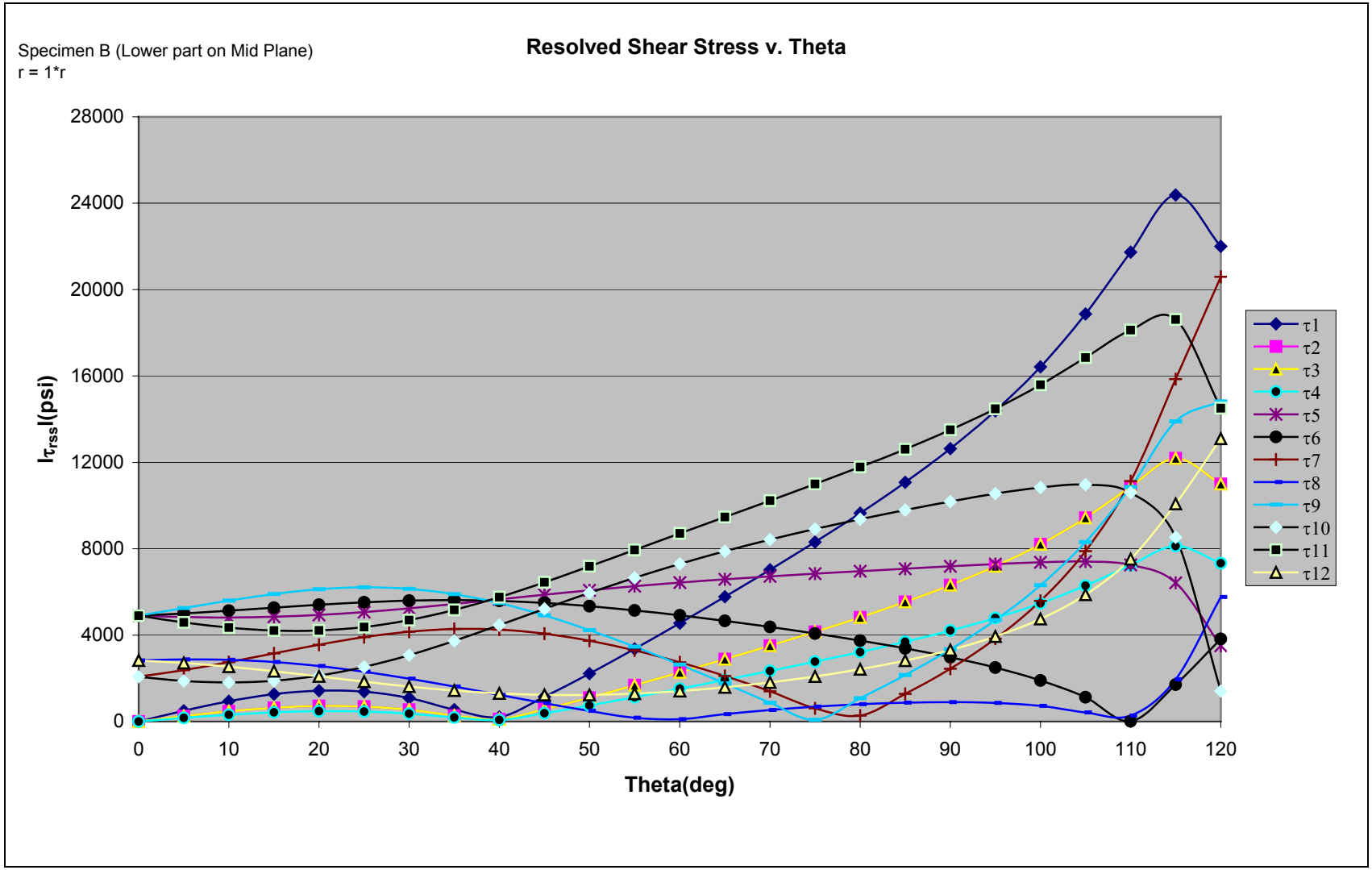

Figure 4-38 Twelve primary resolved shear stresses on the lower half of the mid plane of specimen B; r = 1* ρ

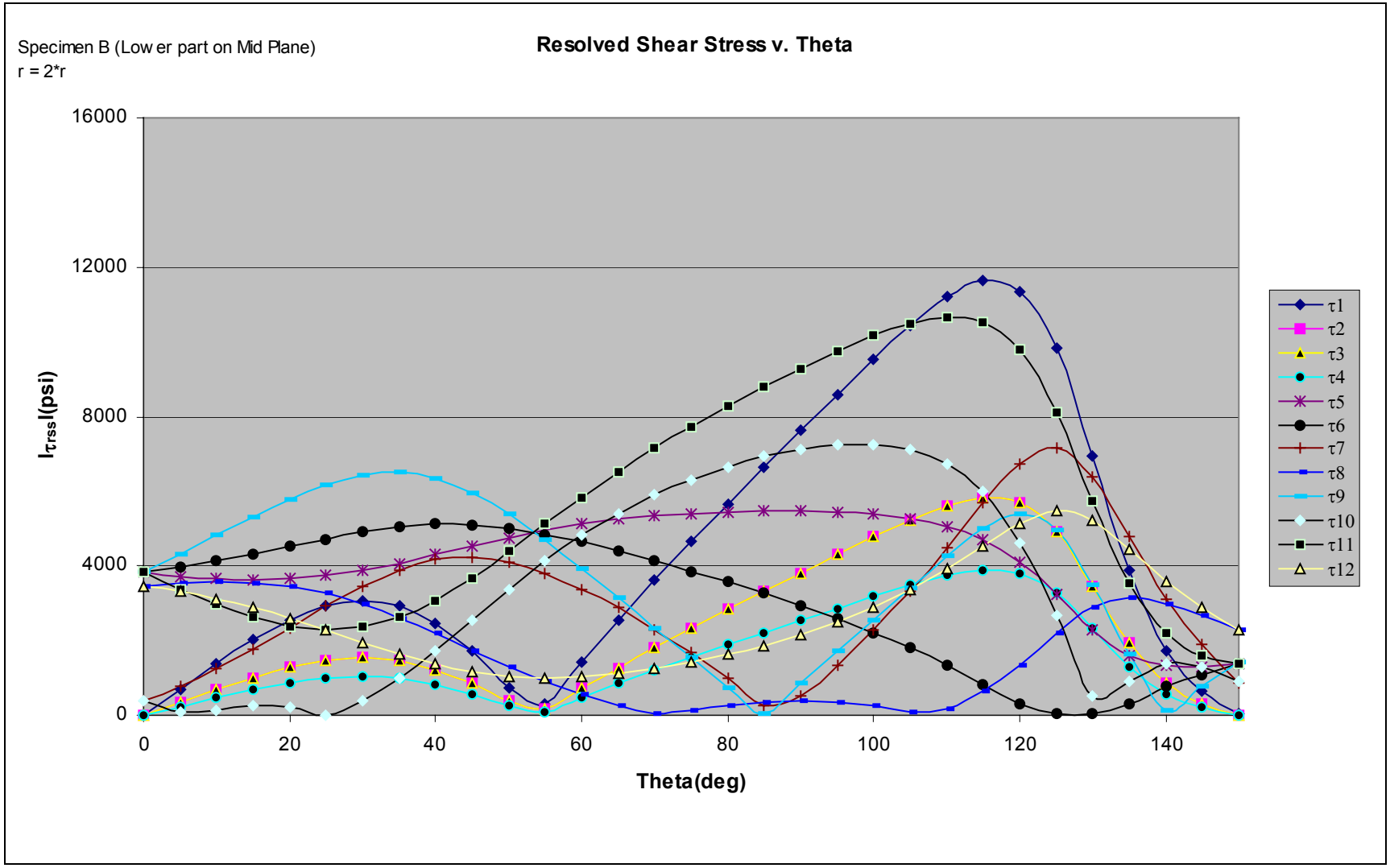

Figure 4-39 Twelve primary resolved shear stresses on the lower half of the mid plane of specimen B; r = 2* ρ

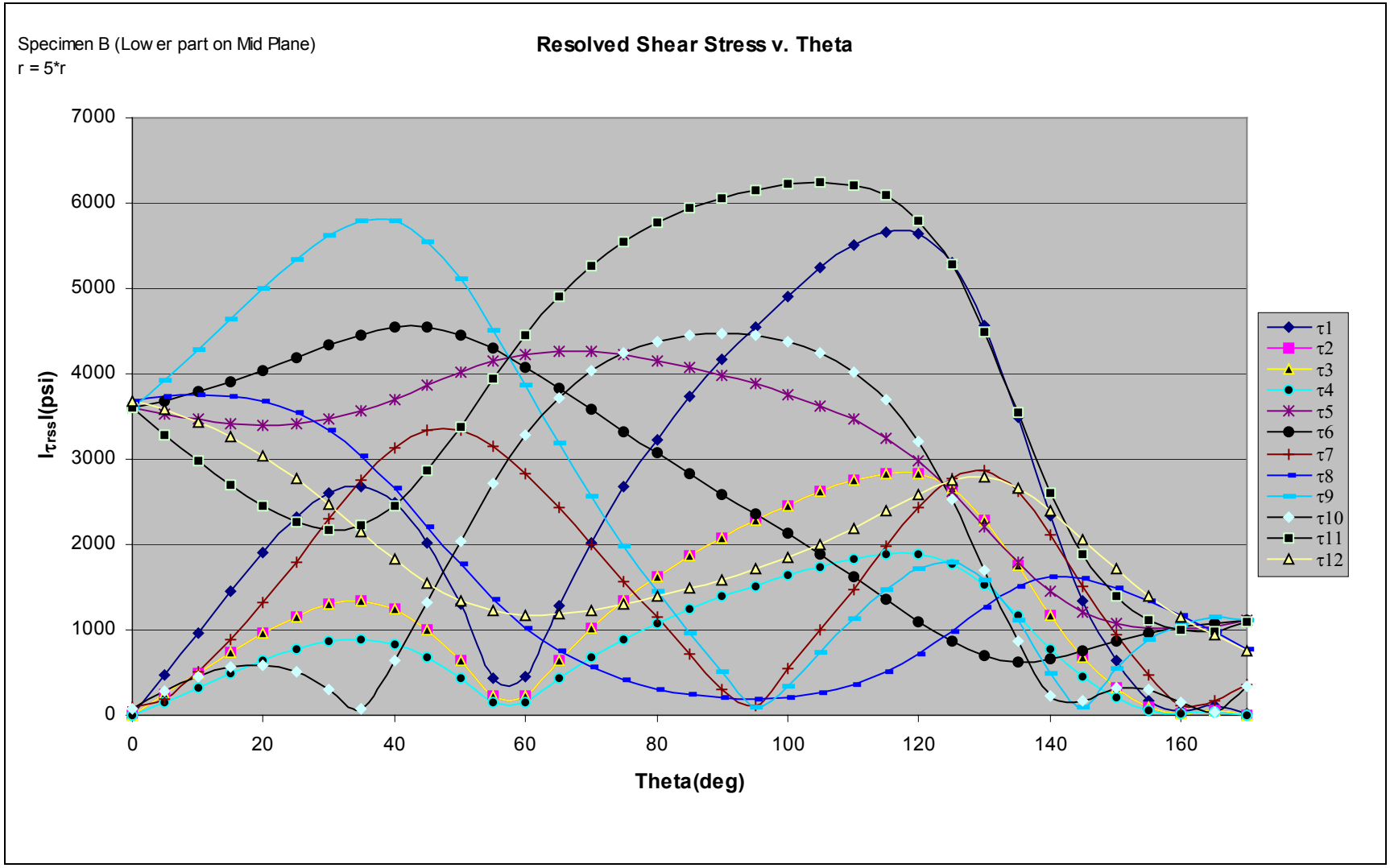

Figure 4-40 Twelve primary resolved shear stresses on the lower half of the mid plane of specimen B; r = 5* ρ

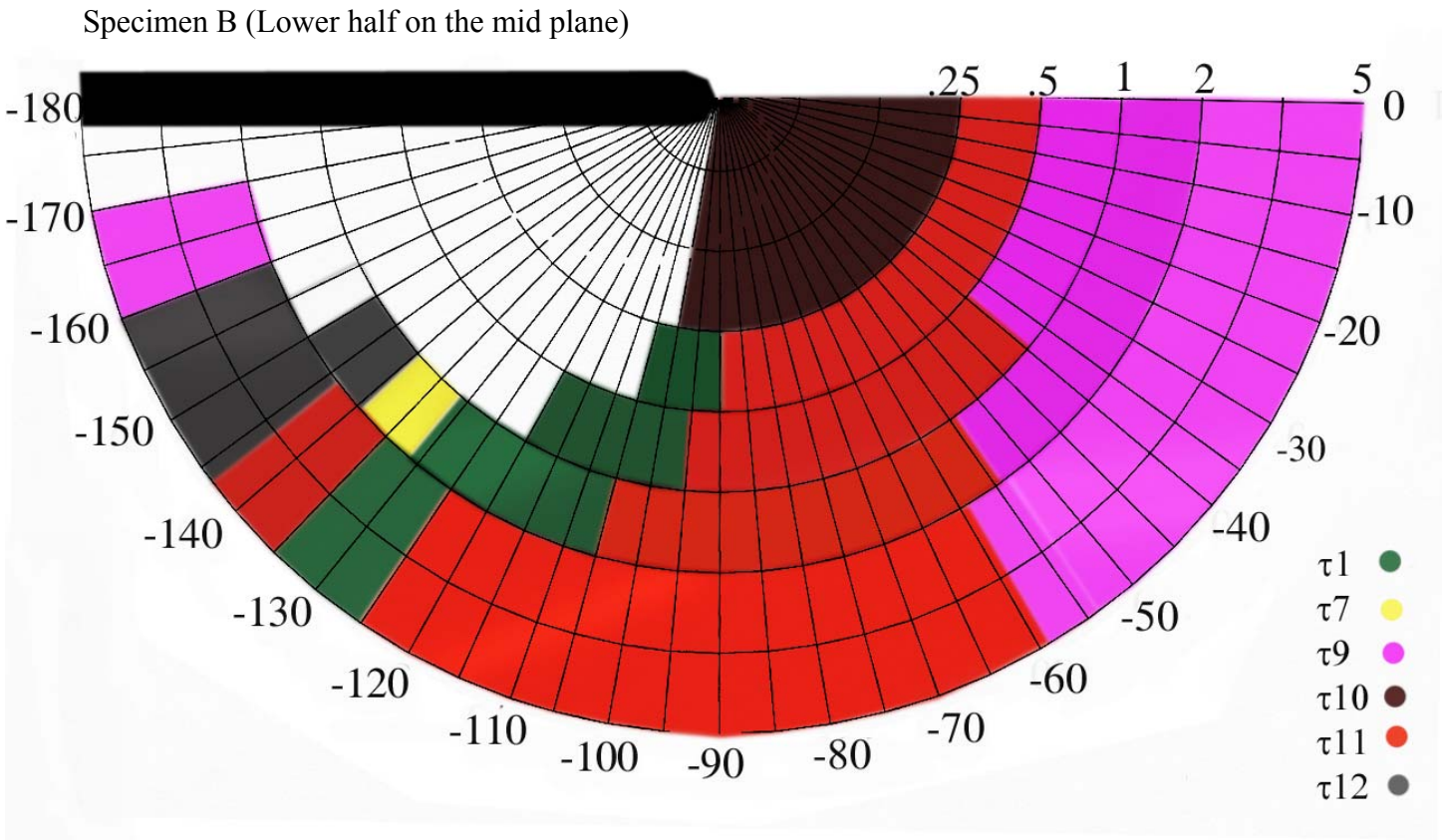

Figure 4-41Maximum resolved shear stress on each radius occurring on the lower half of the mid plane of specimen B.

Table 4-6 Specimen B dominant slip system sectors (Lower half on mid plane)

Dominant Slip System Sectors Specimen B									
	r = 0.25*ρ			r = 0.5*ρ			r = 1*ρ		
Sector	θ	τ_{max}	Slip System	θ	τ_{max}	Slip System	θ	τ_{max}	Slip System
I	0-100	τ_{10}	(-1-11)[011]	0-89	τ_{11}	(-1-11)[101]	0-38	τ_{9}	(1-1-1)[101]
II				89-105	τ_{1}	(111)[10-1]	39-95	τ_{11}	(-1-11)[101]
III							95-120	τ_{1}	(111)[10-1]

	r = 2.0*ρ			r = 5.0*ρ		
Sector	θ	τ_{max}	Slip System	θ	τ_{max}	Slip System
I	0-54	τ_{9}	(1-1-1)[101]	0-58	τ_{9}	(1-1-1)[101]
II	54-105	τ_{11}	(-1-11)[101]	58-125	τ_{11}	(-1-11)[101]
III	105-132	τ_{1}	(111)[10-1]	125-135	τ_{1}	(111)[10-1]
IV	132-137	τ_{7}	(1-1-1)[110]	135-143	τ_{11}	(-1-11)[101]
V	137-150	τ_{12}	(-1-11)[1-10]	143-160	τ_{12}	(-1-11)[1-10]
VI				160-170	τ_{9}	(1-1-1)[101]

Comparison of Specimen Results.

The results of the two specimens A and B were compared on the surface and the mid planes of the specimens. For the specimen A, [001] direction is aligned to the load axis in contrast with specimen B where it is aligned to the notch tip direction.

The results of the two specimens are compared at $r = 0.5*\rho$ since the maximum RSS always occur at this location for both of the specimen on mid planes and on surface planes. For both the specimens, the number of dominant slip systems are small at this radius as compared to the other radii except at $r = 0.25*\rho$. Another observation is that the maximum RSS in both the specimen, appears at mid plane and not on the surface plane. Also the overall maximum RSS occurs at the upper half of mid plane of specimens B about the notch growth axis. The overall minimum RSS occurs at the surface of Specimen A (here no reference is made regarding the upper or lower part of the specimen since the RSS are symmetric about the notch growth axis). A comparison of the maximum RSS values at the surface and mid planes of both the specimens indicates that the lowest maximum RSS occurs at the surface of specimen A. In addition, it is observed that even the second lowest maximum which occurs at the surface of specimen A, is lower than the corresponding values at the mid planes of specimens A and B as well as the surface of the specimen B.

It is seen that, three primary slip planes, are activated on the surface of Specimen A on the (111) plane. From the mechanics point of view, it is unclear whether the slip planes alone have an effect on the desirability of one orientation over another. In fact, certain factors such as second or third maximum can determine the desirability of an orientation since they determine whether mechanism such as cross slip will occur or not.

Though these mechanism results in more deformation; they can avoid fracture by releasing energy through ductile deformation.

In order to predict the most favorable design orientations reasonably high degree of knowledge regarding dislocation and other atomic mechanism is desired. So, to a good approximation, a prediction solely based on a stress based approach, indicate that Specimen A has the best orientation for the tensile loading of a notch specimen.

Experimental Results

The Material Science department conducted experiments to predict slip fields in notched specimens. The predictions made by the numerical approach are compared with the experimental results. The experimental results for Specimen A were presented in a recent paper published by Forero et al. (2002). A tensile load of 1175 lb is applied to the specimen whose geometry was given in Chapter 3. Unlike the numerical model results for Specimen A, which indicated a symmetric distribution about the notch growth axis, the experimental results indicate an asymmetry, because of the 8˚ deviation of the load axis to the [001] axis in the experimental specimen. Therefore, the experimental results quoted here are presented for all values of θ varying between positive and negative θ. After calculating and scaling the RSS values for the actual applied load, a line is drawn on the figures at 47 ksi, which is the yield stress of the material ($\tau_{yield} \sim 47$ ksi). The slip systems above the drawn line were predicted to be activated at the applied load.

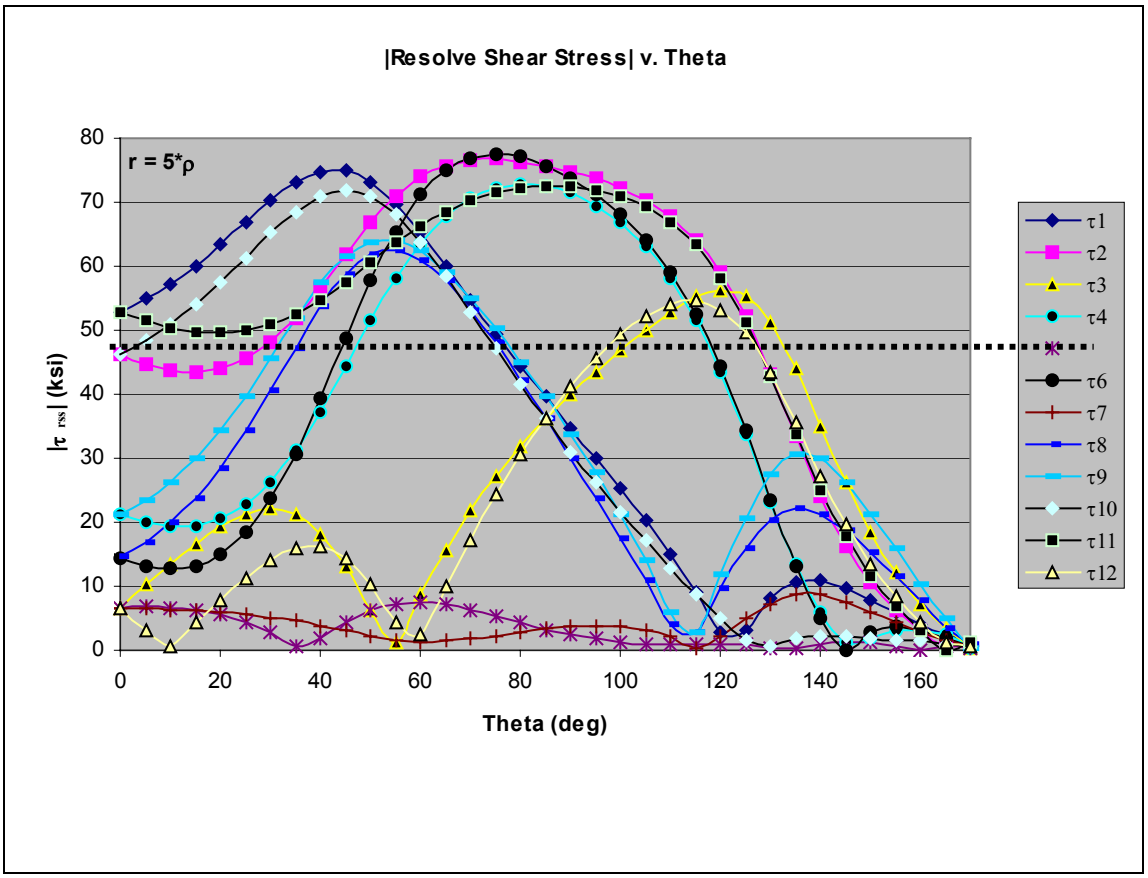

Figure 4-42 RSS for specimen A when experimental load is applied. The dashed line indicates the yield stress of the material. Any RSS curves above this line represent slip systems that are activated.

Also the predictions made for the dominant slip systems by the numerical model for different sector are in agreement with those indicated by the experimental results around the notch. (Table 4-7). The slight disagreement between the numerical results and experimental results is attributed to the 8˚ deviation of the load axis to the [001] axis in the experimental specimen. In addition to this, the irregularities in the cut outs of the notch in the experimental specimens, introduced an additional geometric variable.

Table 4-7 Comparison of numerical and experimental results of specimen A.

Dominant Slip System Sectors Specimen A (r = 5.0*ρ)					
	Numerical Solution			Experimental Results	
Sector	θ	τ_{max}	Slip System	θ	Slip Plane
I	0-54	τ_1	(111)[10-1]	0-75 -(0-65)	(111) or (11-1) (111) or (11-1)
II	54-68	τ_2	(111)[0-11]		
III	68-86	τ_6	(-11-1)[011]	75-90 -(65-100)	(-111) (1-11)
IV	86-122	τ_2	(111)[0-11]	90-110 -(100-115)	(111) or (11-1) (111) or (11-1)
V	122-135	τ_3	(111)[1-10]		

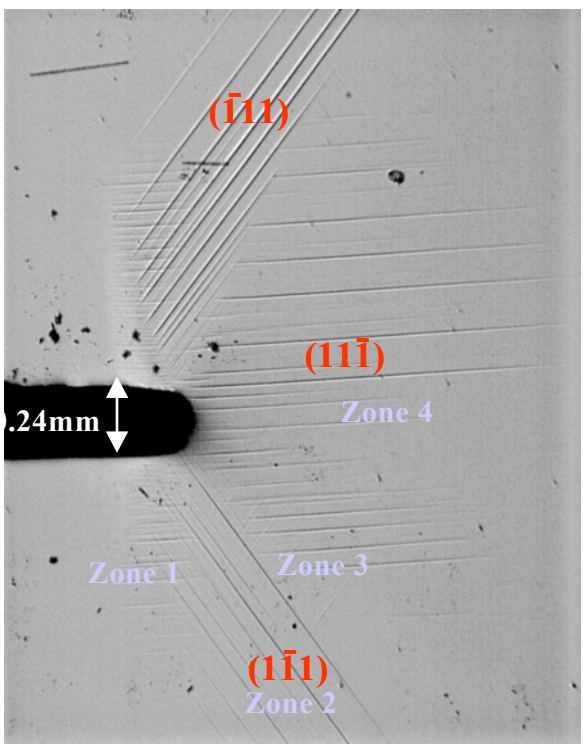

Figure 4-43 Slip planes in experimental tensile test specimen tested by material science department. (Forero and Ebrahimi, 2002).

The past research, which use 2-D isotropic plane stress or plane strain model, predicts sectors with straight boundaries. The present 3-D anisotropic FEA analysis with accurate representation of specimen geometry and load, predicts curved slip sectors boundaries with complex shapes (Figure 4-8). The analysis also predicts several active slip systems at a particular location indicating the greater degree of complexity of slip systems in 3-D stress fields.

Conclusions

Three-dimensional anisotropic stress fields are studied by analyzing the stress field in a single crystal double-edged notched rectangular specimen with varying crystal orientation. Following conclusions are made on the basis of the preceding study.

1) A maximum RSS is found to be on the mid planes of specimens A and B. Hence slip planes will initiate first on the mid plane and progress towards the surface, with increasing load. The State of stress on the mid planes of the specimen will approach conditions of generalized plane strain and hence the stress levels are expected to be higher there.

2) Slip sectors predicted near the notch are seen to be a strong function of crystal orientation, load and CRSS.

3) The Specimen with a (001) notch plane orientation and a [-110] notch growth direction (Specimen A) shows lower resolved shear stresses than one with (111) notch plane and [10-1] notch growth directions at the same applied load. (Specimen B).

4) The general 3-D anisotropic FEA model with accurate representation of specimen geometry and load is found to predict slip systems in good agreement with the experimental results.

5) The present 3-D anisotropic FEA analysis with accurate representation of specimen geometry and load predicts curved slip sectors boundaries with complex shapes.

6) The analysis predicts several active slip systems at a particular location indicating a greater degree of complexity of slip systems in 3-D stress fields, then compared to previously published results for 2-D isotropic plane stress or plane strain model.

Recommendations For Future Work

Prediction of slip systems for the specimens examined under compressive load would be of interest to examine tension compression asymmetry, which is exhibited by single crystal superalloys. This work will also help towards the better understanding of slip systems evolution under fatigue loading. Incorporation of time history, strain hardening, creep and crystal plasticity should also be done in future model to study the near –notch stress fields.

Experimental prediction of slip systems of specimen B is expected to be completed in near future in Material Science Department. Numerical results of specimen B will be compared once the results are available. Other crystal orientation should be examined for the global understanding of dependence of slip systems on crystal orientation and temperature.

APPENDIX

COORDINATE AXES TRANSFORMATION AND ACCURACY CHECKS

Here the first transformation is eliminated since ψ_1=0

$$\begin{pmatrix} x'' \\ y'' \\ z'' \end{pmatrix} = \begin{pmatrix} \cos(\psi_2) & 0 & -\sin(\psi_2) \\ 0 & 1 & 0 \\ \sin(\psi_2) & 0 & \cos(\psi_2) \end{pmatrix} \cdot \begin{pmatrix} x' \\ y' \\ z' \end{pmatrix} \qquad \begin{pmatrix} x''' \\ y''' \\ z''' \end{pmatrix} = \begin{pmatrix} 1 & 0 & 0 \\ 0 & \cos(\psi_3) & \sin(\psi_3) \\ 0 & -\sin(\psi_3) & \cos(\psi_3) \end{pmatrix} \cdot$$

$$\begin{pmatrix} x''' \\ y''' \\ z''' \end{pmatrix} = \begin{pmatrix} \alpha_1 & \beta_1 & \gamma_1 \\ \alpha_2 & \beta_2 & \gamma_2 \\ \alpha_3 & \beta_3 & \gamma_3 \end{pmatrix} \cdot \begin{pmatrix} x' \\ y' \\ z' \end{pmatrix}$$

$$\begin{pmatrix} \alpha_1 & \beta_1 & \gamma_1 \\ \alpha_2 & \beta_2 & \gamma_2 \\ \alpha_3 & \beta_3 & \gamma_3 \end{pmatrix} = \begin{pmatrix} 1 & 0 & 0 \\ 0 & \cos(\psi_3) & \sin(\psi_3) \\ 0 & -\sin(\psi_3) & \cos(\psi_3) \end{pmatrix} \cdot \begin{pmatrix} \cos(\psi_2) & 0 & -\sin(\psi_2) \\ 0 & 1 & 0 \\ \sin(\psi_2) & 0 & \cos(\psi_2) \end{pmatrix}$$

$$\begin{pmatrix} \alpha_1 & \beta_1 & \gamma_1 \\ \alpha_2 & \beta_2 & \gamma_2 \\ \alpha_3 & \beta_3 & \gamma_3 \end{pmatrix} = \begin{pmatrix} \cos(\psi_2) & 0 & -\sin(\psi_2) \\ \sin(\psi_3)\cdot\sin(\psi_2) & \cos(\psi_3) & \sin(\psi_3)\cdot\cos(\psi_2) \\ \cos(\psi_3)\cdot\sin(\psi_2) & -\sin(\psi_3) & \cos(\psi_3)\cdot\cos(\psi_2) \end{pmatrix}$$

$$\psi_2 := \operatorname{atan}\left(\frac{3}{4}\right) \qquad \psi_2 = 36.87\text{deg}$$

$$\psi_3 := -\operatorname{atan}\left(\frac{1}{\sqrt{25}}\right) \qquad \psi_3 = -11.31\text{deg}$$

$$\begin{pmatrix} \alpha_1 & \beta_1 & \gamma_1 \\ \alpha_2 & \beta_2 & \gamma_2 \\ \alpha_3 & \beta_3 & \gamma_3 \end{pmatrix} := \begin{pmatrix} \cos(\psi_2) & 0 & -\sin(\psi_2) \\ \sin(\psi_3)\cdot\sin(\psi_2) & \cos(\psi_3) & \sin(\psi_3)\cdot\cos(\psi_2) \\ \cos(\psi_3)\cdot\sin(\psi_2) & -\sin(\psi_3) & \cos(\psi_3)\cdot\cos(\psi_2) \end{pmatrix}$$

$$\begin{pmatrix} \alpha_1 & \beta_1 & \gamma_1 \\ \alpha_2 & \beta_2 & \gamma_2 \\ \alpha_3 & \beta_3 & \gamma_3 \end{pmatrix} = \begin{pmatrix} 0.8 & 0 & -0.6 \\ -0.118 & 0.981 & -0.157 \\ 0.588 & 0.196 & 0.784 \end{pmatrix}$$

Checks for Accuracy

All should equal zero:

$\alpha_1\cdot\alpha_2 + \beta_1\cdot\beta_2 + \gamma_1\cdot\gamma_2 = 0$ $\quad$ $\alpha_1\cdot\alpha_3 + \beta_1\cdot\beta_3 + \gamma_1\cdot\gamma_3 = 0$ $\quad$ $\alpha_3\cdot\alpha_2 + \beta_3\cdot\beta_2 + \gamma_3\cdot\gamma_2 = 0$

$\alpha_1\cdot\beta_1 + \alpha_2\cdot\beta_2 + \alpha_3\cdot\beta_3 = 0$ $\quad$ $\alpha_1\cdot\gamma_1 + \alpha_2\cdot\gamma_2 + \alpha_3\cdot\gamma_3 = 0$ $\quad$ $\beta_1\cdot\gamma_1 + \beta_2\cdot\gamma_2 + \beta_3\cdot\gamma_3 = 0$

All should equal one:

$\alpha_1^2 + \beta_1^2 + \gamma_1^2 = 1$ $\quad$ $\alpha_2^2 + \beta_2^2 + \gamma_2^2 = 1$ $\quad$ $\alpha_3^2 + \beta_3^2 + \gamma_3^2 = 1$

$\alpha_1^2 + \alpha_2^2 + \alpha_3^2 = 1$ $\quad$ $\beta_1^2 + \beta_2^2 + \beta_3^2 = 1$ $\quad$ $\gamma_1^2 + \gamma_2^2 + \gamma_3^2 = 1$

All checks verify a proper transformation.

REFERENCES

ANSYS Elements Reference, ANSYS Release 5.6; ANSYS, Inc. November 1999.

Cowles, B.A., "High Cycle Fatigue Failure in Aircraft Gas Turbines: An Industry Perspective," International Journal of Fracture, **80**, pp.147-163, 1996.

Crone, W. and Shield, T., "Experimental Study of the Deformation near a Notch Tip in Copper and Copper-Beryllium Single Crystals," Journal of the Mechanics and Physics of Solids, **49**, 2001, pp.2819-2838.

Cuitino, A. and Ortiz, M., "Three-Dimensional Crack Tip Fields in Four-Point Bending Copper Single-Crystal Specimens," Journal of the Mechanics and Physics of Solids, **44** (6), 1996, pp. 863-904.

Davis, J.R., ed., Heat Resistant Materials, ASM Specialty Handbook, Materials Park, Ohio: ASM International, 1997, pp.256-263.

Dieter, G., Advanced Mechanical Metallurgy, 3rd Ed., New York: McGraw-Hill, 1986, pp.106-130.

Deluca, D. and Annis, C., "Fatigue in Single Crystal Nickel Superalloys," Office of Naval Research, Department of the Navy FR23800, August 1995.

Fermin, J., Master of Science Thesis, Materials Science And Engineering Department, University of Florida, Gainesville, FL, 1999.

Lekhnitskii, S.G., Theory of Elasticity of an Anisotropic Elastic Body, San Francisco: Holden-Day, Inc., 1963, pp.1-40.

Meetham, G.W. and Voorde, M.H., " Materials for High Temperature Engineering Applications." New York: Springer-Verlag, 2000,pp.78-80.

Mohan, R.; Ortiz, M., and Shih, C., "An Analysis of Cracks in Ductile Single Crystals—II. Mode I loading," Journal of the Mechanics and Physics of Solids, **40** (2), 1992, pp.315-337.

Mollenhauer, D.; Ifju, P., and Han, B., "A Compact, Robust and Versatile Moiré Interferometer," Optics and Lasers in Engineering, **23**, 1995, pp. 29-40.

Moroso, J., Master of Science Thesis, Mechanical Engineering Department, University of Florida, 1999.

Rice, J.R., "Tensile Crack Tip Fields in Elastic-Ideally Plastic Crystals," Mechanics of Materials, **6**, 1987, pp.317-335.

Saeedvafa, M. and Rice, J.R., "Crack Tip Singular Fields in Ductile Crystals with Taylor Power-Law Hardening, II: Plane Strain," Journal of the Mechanics and Physics of Solids, **37** (6), 1989, pp.673-691.

Shield, T., "An Experimental Study of the Plastic Strain Fields near a Notch Tip in a Copper Single Crystal During Loading," Acta Materialia, **44** (4), 1996, pp.1547-1561.

Shield, T., "Microscopic Moiré Interferometry," Retrieved March 11, 2002 from the World Wide Web: http://www.aem.umn.edu/people/faculty/shield/mm.html.

Shield, T. and Kim, K., "Experimental Measurement of the Near Tip Strain Field in an Iron-Silicon Single Crystal," Journal of the Mechanics and Physics of Solids, **42** (5), 1994, pp.845-873.

Stouffer, D. and Dame, L., Inelastic Deformation of Metals: Models, Mechanical Properties, and Metallurgy, New York: John Wiley & Sons, Inc.; 1996, pp.387-417.

BIOGRAPHICAL SKETCH

The author of the thesis was born on the 10th of December 1977 in Nagpur and has an Indian origin. He lived in Nagpur for nearly 23 years where he completed his Bachelor of Engineering degree from Y. C College of Engineering. In the year 2000, he traveled to the United States of America for the pursuit of a master's degree in mechanical engineering at the University Of Florida. He is scheduled to complete the degree of Master of Science in mechanical engineering in December 2002.